EVALUATION OF Ti-6Al-4V PARTS PRODUCED WITH RAPID PROTOTYPING TECHNOLOGY: ELECTRON BEAM MELTING MACHINE

A Thesis

by

DANA ABDEEN

Submitted to the Office of Graduate and Professional Studies of
Texas A&M University
in partial fulfillment of the requirements for the degree of

MASTER OF SCIENCE

Chair of Committee,	Bruce Palmer
Committee Members,	Marcelo Castier
	Eyad Masad
Head of Department	Nazmul Karim

December 2014

Major Subject: Chemical Engineering

ABSTRACT

The present study measured the corrosion properties of Ti-6Al-4V parts produced with Electron Beam Melting machine (EBM). Potentiodynamic and potentiostatic tests were applied on EBM Ti-6Al-4V in 3.5% mass NaCl solution, to determine the pitting potential and critical pitting temperature (CPT). A relation between pitting potential and temperature was established for EBM Ti-6Al-4V alloy by conducting potentiodynamic test under different temperatures from room temperature until 83ºC. Critical pitting temperature was also measured in 3.5% mass NaCl solution of different pH of 2.0, 5.7 and 10.0, to examine the effect of aggressive conditions on the pitting corrosion of EBM alloy. Moreover, the same tests were performed on wrought Ti-6Al-4V for comparison purposes. The results showed that EBM alloy maintained its corrosion resistance as it had the same pitting potential of wrought alloy even at higher temperatures. EBM alloy did not pit when performing potentiostatic test at 800 mV vs. Saturated Calomel Electrode (SCE) even under different pH of the solution.

Due to the manufacturing technique and conditions of the EBM machine, the resulted object has irregularities on the exterior surface and voids that are formed within the part which affects samples' properties like surface roughness, CPT, density and porosity. In this study, a statistically designed experiment was employed to manufacture Ti-6Al-4V samples in EBM machine under different process parameters of beam current, beam speed and offset focus. Surface roughness was measured for as-built samples. Then, a potentiostatic test was conducted under 2.40 V vs. SCE to determine the critical pitting temperature in 3.5 % mass NaCl solution for the same samples of different processing parameters. Moreover, density was measured and porosity was calculated from density values. Finally, a model equation was established in order to relate EBM's process parameters to measured properties of surface roughness, CPT, density and porosity. It was noted that offset focus had the main influence on surface roughness more than beam current and beam speed. Changing processing parameters did not affect corrosion behavior of EBM Ti-6Al-4V as CPT did not vary widely, with a slight effect obtained from beam current and beam speed. Density and porosity were greatly affected with offset focus more than the other parameters. It can be concluded that uniform and precise roughness and porosity are not achievable through this machine, only a range of these properties can be attained.

DEDICATION

To my parents for their love and compassion.

To my husband Sami, my first inspirer, for his continuous encouragement, patience and love.

To my kids Nizar, Nada and Nadeen for their support and sacrifice.

To my sisters and brother, for their reinforcement and concern.

ACKNOWLEDGEMENTS

Foremost, I would like to thank God for giving me the capability and strength to finish this work, Elhamdoullelah.

I would like to express my sincere gratitude to my advisor Prof. Bruce Palmer; you have been a great advisor with the knowledge that I have acquired from you. Thank you for your continuous support of my research, for your patience and encouragement during the years that I have worked with you.

I would like to acknowledge my committee members: Dr. Marcelo Castier and Dr. Eyad Masad.

I would like to express my special appreciation and thanks to Dr. Walid Khalfaoui for his guidance and advice throughout this research, as he did not hesitate to enrich me with his experience since the early stages of my research. And I was blessed to be surrounded by cheerful and friendly team who supported me throughout my study; Nasser Al Jassem, Safwan Ghannam and Hanan Farahat.

Finally, thanks to all the members and staff in the chemical and mechanical engineering departments at Texas A&M University at Qatar who helped in making this research possible.

TABLE OF CONTENTS

Page

Page

LIST OF TABLES

Page

Page

LIST OF FIGURES

Page

Page

Page

Page

CHAPTER I

INTRODUCTION

1.1 Titanium and its Alloys

1.1.1 Titanium

Titanium is a lustrous transition element of a silver color. It is a non-ferrous metal with a density of 4.51 g/cm^3, and relatively high boiling and melting points of 3,287°C and 1,660°C, respectively. As it is a highly reactive metal when exposed to air, it cannot be found as pure metal in nature; it presents in mineral forms like rutile (TiO_2), ilmenite ($FeTiO_3$) and sphene ($CaTiSiO_5$). Titanium is the fourth most abundant metal in the earth after aluminum, iron, and magnesium, and makes up about 0.57% of the Earth's crust (Thomas Jefferson National Accelerator Facility, 2011). Extracting it from ores was delayed until the development of the Kroll process in 1950 (Welk, 2010). Due to its high melting point and high reactivity, extraction of titanium from ores is an expensive process, hence, its applications are limited to aerospace and marine applications where weight savings and decreased maintenance cost are critical. In recent times, titanium is used in many other industrial applications as in subsea, offshore, petrochemical equipment, and metal finishing. In addition, titanium plays a major role in biomedical applications and athletics equipment due to its distinct physical and chemical properties.

Titanium experiences allotropic transformation from HCP (Hexagonal Close-Packed) α phase to BCC (Body Center Cubic) β phase at a temperature called β transus temperature. β transus temperature is the lowest equilibrium temperature at which an alloy is 100% β phase (Donachie, 2000). At room temperature, titanium has α HCP crystal structure that transforms to β BCC crystal structure at 882 ±2°C (Safdar, 2010). This transformation temperature is important as it is the reference for any heat treatment and processing conducted on the alloy. It can be of a lower or higher value depending on the alloying elements and their proportions (Donachie, 2000). Hexagonal Close-Packed (HCP) and Body Center Cubic (BCC) crystal structure are shown in Figure 1.

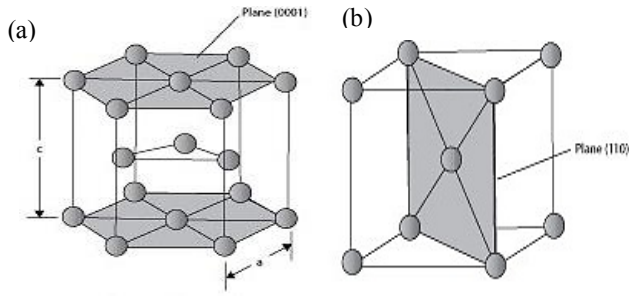

Figure 1: (a) α phase, HCP crystal structure. **(b)** β phase, BCC crystal structure (Callister & Rethwisch, 2007).

1.1.2 Titanium Alloys

Commercially pure (CP) titanium presents in the HCP crystal structure (α phase) at room temperature and changes to BCC crystal structure (β phase) when it reaches the β transus temperature of 822°C ±2°C. Since elements added to CP titanium will change the microstructure, the type and amount of element added will modify the β transus temperature, too.

Figure 2 illustrates the effect of elements added on β transus temperature. If the element added is an α stabilizer like oxygen, aluminum, nitrogen, and carbon, β transus temperature increases as these elements tend to stabilize in α phase. On the other hand, this temperature decreases when β stabilizer elements such as magnesium, iron, chromium, silicon and others are added. β stabilizers are classified in two groups: β isomorphous and β eutectoid (Campbell, 2008).

Some elements like zirconium and tin have a neutral effect on the β transus temperature. They are added to improve the mechanical properties of the alloy rather than affecting the phase transformation temperature (Campbell, 2008). According to the element added to CP titanium, titanium alloy is classified as (1) an α and near-α alloy, (2) β stabilizer alloy, and (3) α+β alloy.

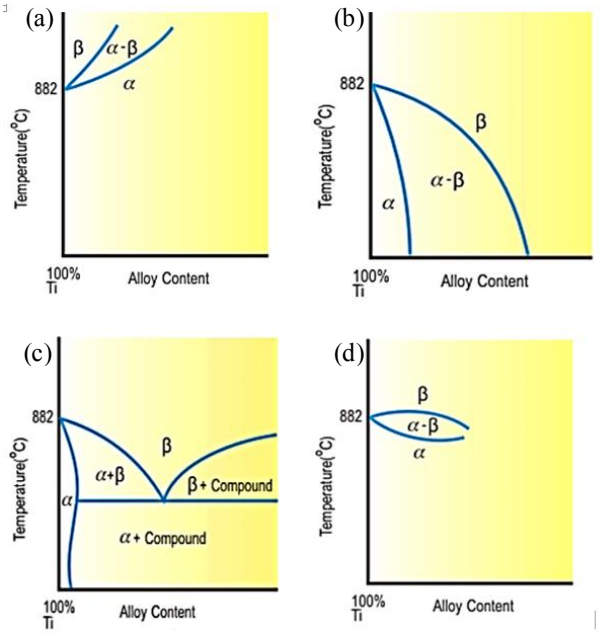

Figure 2: Titanium alloy phase diagrams with different types of stabilizers **(a)** α stabilizers. **(b)** β isomorphous stabilizers. **(c)** β eutectoid stabilizers. **(d)** Neutral stabilizers (Campbell, 2008).

α and near-α Alloys

α stabilizers include aluminum, oxygen, nitrogen, and carbon. These elements have HCP crystal structure at room temperature, and tend to stabilize towards α phase hence increasing the β transus temperature of the resulting alloy. α and near-α alloys contain one or more of these stabilizers with small amounts of β stabilizers like vanadium or iron. An α stabilizer provide excellent corrosion resistance and deformability while obtaining high strength (Campbell, 2008).

Commercially pure titanium is one of the α alloys where oxygen is added as an interstitial to increase its strength, at the same time it decreases ductility significantly (Leyens, 2003). These α alloys have satisfactory strength, toughness, creep resistance and weldability. Despite the fact that they are associated with reduced ductility, they do not have ductile-brittle transition which makes them suitable for cryogenic applications (Boyer, et al., 1994). Ti-5Al-2.5Sn is the only true α alloy that is commercially produced.

β Stabilizer Alloys

Transition metals like vanadium, niobium, and molybdenum, can stabilize titanium in the BCC structure at room temperature. Choosing the right cooling rate upon quenching plays a major role in maintaining β phase at room temperature. Small amounts of α stabilizer are added to this kind of alloy in order to increase its strength.

β stabilizer alloys have higher fracture toughness, better shaping and forming properties at room temperature than α and near-α alloys (Campbell, 2008). Yet, they have a poor high-temperature creep resistance and low ductile-brittle transition temperature which makes them unsuitable for low temperature applications (Boyer, et al., 1994). These alloys are used in the biomedical field due to their biocompatibility, and in the aerospace industry where high yield strength along with low modulus of elasticity are of major concern (Welk, 2010).

α +β Alloys

α + β alloy contains both α stabilizer and β stabilizer, indicating that it has HCP and BCC crystal structure at room temperature. It has improved strength and formability compared with α and near-α alloys. This unique blend of structure gives these alloys extraordinary mechanical properties, including a good combination of strength, ductility, fatigue and fracture properties (Welk, 2010). For this reason, α + β alloys are the most widely used titanium alloys in many commercial applications, and Ti-6Al-4V is the most commonly used one.

1.1.3 Ti-6Al-4V Alloy

Adding aluminum and vanadium to commercially pure titanium in small amounts increases the strength of the alloy significantly. With aluminum as the α stabilizer and vanadium as the β stabilizer, the β transus temperature is lowered –in comparison with α alloys- so that both phases are maintained at room

temperature. This allows Ti-6Al-4V to have special properties over α and near-α alloys and β alloys. Figure 3 shows the main characteristics of different titanium alloys and highlights that Ti-6Al-4V possesses an exceptional combination of both types of alloys.

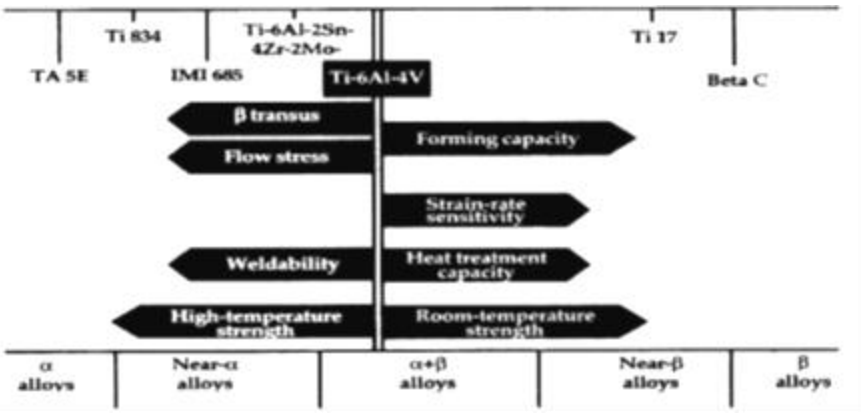

Figure 3: Main characteristics of titanium alloys (Donachie, 2000).

Preprocessing and heat treatments performed on this alloy affect its microstructure as different phases may appear, which causes changes in its properties as well. For instance, the cooling rate and solution temperature changes the yield strength, tensile strength and percent elongation of Ti-6Al-4V when it is heat treated (Donachie, 2000). Slow cooling of Ti-6Al-4V from the β region forms a nucleus of α at temperatures below 980°C. Upon further cooling, the α phase thickens slowly to develop plates, which thicken more to form parallel plates of α with β phase on the boundaries. This kind of microstructure is called Widmanstatten, and Figure 4 shows a schematic draw of its development in Ti-6Al-4V alloy.

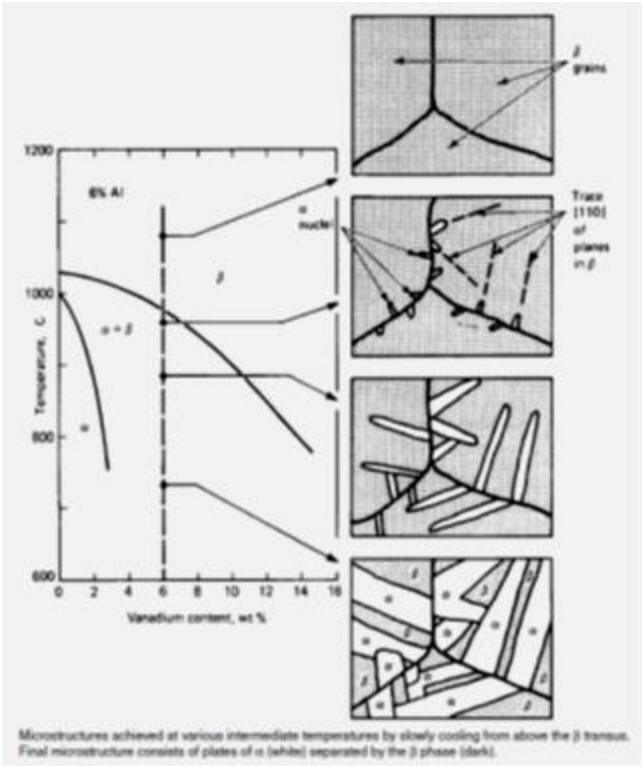

Figure 4: Schematic development of Widmanstatten structure in α+β alloy (Ti-6Al-4V) (Donachie, 2000).

With this microstructure and the special properties of light weight, extreme corrosion resistance, high strength and capability to withstand high temperature, Ti-6Al-4V is considered to be the workhorse in the aerospace industry. It accounts for 60% of the titanium used in aerospace and up to 90% of that used in airframes (Campbell, 2008). Ti-6Al-4V has replaced heavier, less cost-effective materials as the properties of this alloy resulted in reliable and more economic systems which in sequence increased performance and service life of that material.

1.1.4 Characteristics of Titanium Alloys

Titanium and its alloys are valuable engineering materials due to their excellent mechanical and physical properties. Compared to other metallic materials such as stainless steel and Co-Cr alloys, Ti and its alloys are of lighter weight, higher strength-to-weight ratio, and better corrosion resistance in wide range of

environments (Campbell, 2008). Recent availability of commercial titanium grades from Russia and China have made the applications of titanium-based alloys more accessible for industry consumers (Yu & Company, 2003).

Table 1 shows a comparison of selected materials' properties with commercially pure titanium (CP titanium) and titanium grade 5. CP titanium is as strong as stainless steel, but nearly 55% lighter. CP titanium, when alloyed with aluminum and vanadium as in grade 5, becomes even lighter and 20% stronger. Ti-6Al-4V is 60% heavier than aluminum, but 15 times stronger. In general, titanium alloys have high melting and boiling points and can work in environments of 370°C to 590°C (Campbell, 2008). Their high strength-to-weight ratio and ability to withstand high temperatures have caused them to supersede steel in many applications that require high strength and fracture toughness.

Table 1: Properties of Selected Materials (Callister & Rethwisch, 2007).

Physical Property	Stainless Steel 316	Stainless Steel 405	CP Titanium (grade 1)	Ti-6Al-4V (grade 5)	6061 Aluminum alloy	AZ91D Magnesium alloy
Density (g/cm^3)	8.00	7.80	4.51	4.43	2.70	1.81
Modulus of elasticity, at room temperature (GPa)	193	200	103	114	69	45
Passion ratio, at room temperature	0.30	0.30	0.34	0.34	0.33	0.35
Yield strength (MPa)	205	170	170	830	55	97-150
Tensile strength (MPa)	515	415	240	900	124	165-230
Percent elongation	40	20	24	14	30	3
Coefficient of thermal expansion (10^{-6} $(ºC)^{-1}$)	16.0	10.8	8.6	8.6	23.6	26.0
Thermal Conductivity, at room temperature (W/m.k)	15.9	27.0	16.0	6.7	180.0	72.0
Specific heat, at room temperature (J/kg.k)	502	460	528	610	896	1050

Furthermore, titanium alloys have a superior corrosion resistance to both aluminum and magnesium. This is due to the instantaneous formation of a very stable, highly adherent, continuous protective layer on their surface when exposed to air or moisture. Actually, the damaged film can heal itself instantly if a trace of oxygen is present (Schutz, 2005a). This extraordinary feature enables titanium to be used in many aggressive environments, including seawater.

However, corrosion resistance of titanium is not limited to seawater environment. Titanium is being increasingly utilized for medical applications due to its light weight, high strength and corrosion resistance in biological environments (Noort, 1987). It is widely used in the dentistry and medical implants industries in both its pure or alloyed forms. Ti-6Al-4V has high tensile properties that allows it to tolerate high stress bearing situations like in hip prosthesis and artificial knee replacements. While CP titanium is more common in dental applications where lower strength is not a concern but providing contamination free surroundings is essential. Titanium also has a low modulus of elasticity which helps in overcoming the mechanical incompatibility with bones better than any other material does (Noort, 1987).

1.1.5 Titanium Applications

Due to its extraordinary characteristics of low specific gravity, non-magnetic property, high specific strength, high corrosive resistance property, and its biocompatibility, titanium and its alloys are widely used in many applications such as the following:

- **Petrochemical industry**: Ti and its alloys are often used in the petrochemical industry in heat exchangers, distillation units, and reactors due to their high level of corrosion resistance to seawater and sulfur compounds, and high temperature and pressure resistance properties. In addition, light-weight pipes of titanium are an excellent material for deep sea production risers.
- **Chemical Processing**: Titanium alloys are used in power generation plants where saline, brackish or polluted waters are used in the cooling process because they resist corrosion which enables longer equipment life and reduces maintenance costs. They are also used in condensers and in desalination plants.
- **Aerospace applications**: Ti alloys conserve weight while noise is reduced and aircraft efficiency is increased. Also, their light weight and capability to withstand extreme temperatures have made them suitable for building aircraft turbine disks, blades, jet engines, and airframes.
- **Medical applications**: Since titanium is inert to human body fluids, it is considered to be biologically compatible with human bone and tissue. Titanium implants can adhere to bone and tissue without

interfering with growth. Titanium hips, spinal discs, and knee joints are widely used replacements, along with rods, plates, and mesh that are used to support broken bones. Furthermore, it is also used in dentistry for root implants, crowns, and bridges (Gaytan, et al., 2009).

- **Automotive industry**: Engine parts like connecting rods, valves, wrist pins, rocker arms and springs are made of titanium as it has proven to be tough, lightweight, and resistant to heat and corrosion. It is preferred as it generates parts for better performance, low lifecycle cost, and longer life (Azom, 2002).

1.2 Rapid Prototyping Technology

Rapid prototyping (RP) or direct manufacturing (also called layered manufacturing (LM), or rapid manufacturing (RM)) is a technology used for manufacturing three-dimensional objects from a computer aided design (CAD) model by means of layer-based building. The name of this technology signifies its function. With this CAD presentation, the machine utilizing this technique directly fabricates complex geometries while saving time, production space, and manpower requirements (Liou, et al., 2012). It has proven to have other advantages in industry, as the resulting parts have better material properties with higher performance and accurate dimensions, more than parts made by any other conventional processing (Campbell, et al., 2012).

1.2.1 RP Classifications

Using the concept of the RP technique, many systems have been developed in the market. These systems can be classified according to the input to the machine, material used in fabrication, applications of produced parts and manufacturing method. Figure 5 shows the Rapid Prototyping wheel with its four major classifications.

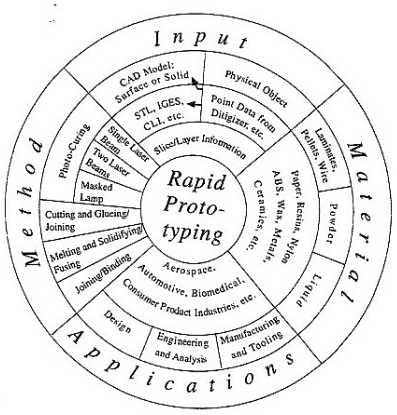

Figure 5: Rapid Prototyping wheel showing four major classifications of RP (Chua, et al., 2003).

Input

Input to RP systems is the model of electronic information needed to describe the object to be manufactured. It can be a computer model or physical model. A CAD model is created in the computer directly, while with physical object equipment like CMM (coordinate measuring machine) it is used to reconstruct captured points of the physical object into a CAD system.

Method

The method of fabrication used can be based on photo curing (hardening), cutting and gluing/joining, melting and solidifying/fusing and joining/blinding. Photo curing can be done either with a single laser beam, two laser beams or masked lamp. A detailed discussion of each method is mentioned in Rapid Prototyping: Principles and applications by Chua and Leong (Chua, et al., 2003).

Applications

RP has a wide range of applications which can be divided into the following categories: design, engineering and analysis, and manufacturing and tooling. Parts produced out of RP are used in many industries like

automotive manufacturing, aerospace industry, medical implants, jewelry and athletic equipment. Details for some of these applications are further discussed in section 1.2.4.

Material

The material used can be in an initial state of either solid, liquid or powder. Solid state comes in forms of laminates, pellets or wire. In liquid-based RP systems, an organic resin contained in a vat solidifies -or cures- under the exposure of laser radiation as in the StereoLithography Apparatus (SLA) and laser beam curing systems. Powder-based RP systems utilize a powder that is melted with electrons of high energy directed by a CAD design to form fully dense functional objects. The electron beam melting machine uses this metallic powder in production, while selective laser sintering (SLS) systems can use metallic powder or ceramic and thermoplastic composites as well (Chua, et al., 2003).

Fused deposition systems are examples for solid-based systems where ceramic and metal objects are produced using ceramic-polymer or metal-polymer feeds. In solid-based systems, a polymer or wax is used as a binding material which also helps eliminate internal defects. Polycarbonate ABS (acetonitrile butadiene styrene) is one of the polymer binders commonly used (Agarwala & Jamalabad, 1996).

1.2.2 RP Process Chain

The process chain of RP to fabricate an object passes through different stages. The first stage is the 3D geometric modeling where the object is represented as an enclosed volume of specified dimensions for the inside and outside boundaries with CAD (Computer-Aided Design) programing. The original part has supports around it which are extra structures built to retain the height of over hanged parts that might fall due to gravity. These supports are also represented with CAD program as part of the main object.

This CAD presentation is then transferred into STL file format (STereoLithography) that approximates the surface as tiny triangular facets described by set of X, Y and Z coordinates to count for curvature in objects. This means curved objects will have a large STL file. As the STL file is an

approximation to the real part, errors may appear like overlapping facets and missing facets that can cause gaps in the form of cracks and holes. For this reason, the file is checked for errors and repaired with specialized software like MAGICS.

Once the STL file is error free, it is sliced into cross sections which are systematically recreated during the fabrication process. A cross section of the layers has a thickness range between 0.12 mm (minimum) and 0.5 mm (maximum). Usually the original structure of the object is sliced with the minimum thickness to obtain accurate dimensions while the supports are constructed at the maximum thickness.

Next is the fully automated building stage. Building parameters of RP system are specified to make the build. Build time can take up to several hours depending on the size and number of parts to be built. The final stage is post processing. Supports which are excess parts on the original object are detached manually. Furthermore, depending on the RP system used, excess pieces of wood, resin or powder trapped in holes and on the sides of the part are removed as well. This task requires some caution as damaging of the part can occur (Chua, et al., 2003). Figure 6 shows RP Process chain.

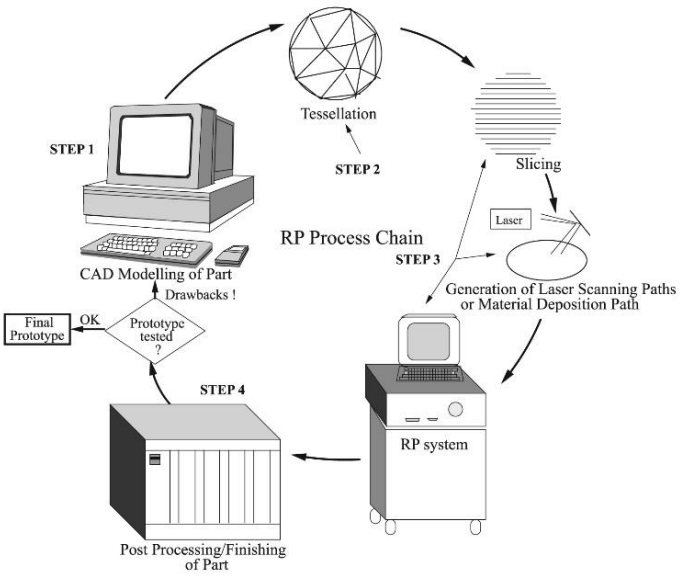

Figure 6: Rapid Prototyping process chain (Pandey, et al., 2003).

1.2.3 Advantages of RP

Rapid prototyping (RP) is suitable where the need for custom-made design is required while maintaining both the safety and compatibility aspects. Joint replacements and skull implants are good examples of applications for these parts fabricated by RP. With RP technology, it is possible to produce custom made shapes that suit a patient's dimensions designed directly from a computer model. Ti-6Al-4V is used in an electron beam melting machine (EBM), which is one of the RP systems. This alloy has proven to have exceptional compatibility with body bones and tissues. It has a light-weight, a porous surface and tolerates biological environment well which helps in fast healing and growth of tissues around the implants (Noort, 1987). In addition, most RP systems, such as electron beam melting machine, are conducted in a high-vacuum environment allowing for a contamination-free work zone, which supports optimal conditions to produce parts with better properties and higher functionality.

RP is a self-assembly process with a laser or electron beam as the energy source. RP builds parts layer-by-layer by means of sintering or melting the material which solidifies quickly. As a consequence, cost of labor, inspection, and assembly are minimized. Furthermore, time is reduced and prior production steps are eliminated. Conventional manufacturing processes like forging and machining require several details to be prepared in addition to the design of the object, which makes the tooling and die design process difficult and long. Scraps from tooling and die design must be disposed of as waste which increases overall time and cost of fabrication. Chua et al. noted the influence of employing RP in a process: in addition to allowing an increase in product's complexity, RP saves 50% to 90% in time and cost depending on the size of product (Chua, et al., 2003).

RP is a unique process. Besides avoiding molding, machining and forming, it eliminates the constraints that these conventional manufacturing methods impose and provides flexibility in the design of objects. A traditional manufacturing process like casting requires that tooling and dies built for a specific part and are not suitable for the production of another part. Any change or addition in features requires new custom tools and dies. However, RP can change the dimension and shape of the part quickly to meet with

the changing market needs which saves production and inspection time and eliminates cost of handling and the earlier stages of preparation.

1.2.4 Industrial Applications of RP

With the great benefits of RP, many industries have begun to utilize it in the production process. It is not only economically viable in comparison to the traditional techniques, but it also saves time and achieves the required job with high functionality. Below are some of the industries that have introduced RP into their production process:

- Automotive manufacturing:

RP is preferred in this industry because it can produce one piece of a complex set of parts for better functionality which can be fit directly on the automobile. RP parts are also easily adjusted to required dimensions. With rapid production, the RP parts can reach the consumer/commercial market quickly. The Renault team in Formula 1 (F1) racing has adopted RP to manufacture some parts. Figure 7(a) shows a cooling duct made with this technology. In addition, NASCAR uses RP in preparing race car parts, including airflow parts and brake air inlet ducts (Hopkinson, et al., 2005).

- Aerospace industry:

RedEye -a RP manufacturing company- demonstrated that RP parts have low FST (flame, smoke, toxicity) evolution, high heat resistance and high strength-to-weight ratio. Redeye utilizes fused deposition modeling (FDM) equipment to fabricate aerospace components with decreased time and cost compared to conventional machining processes (RedEye, 2014). RP generates light-weight structures of complex geometries. It fabricates parts that integrate high performance and mechanical functionality. For these reasons, aerospace companies have included this technology in space stations and aircraft designs. Figure 7(b) shows space station retainers that eliminate vibrational movements produced with selective laser sintering (SLS) technique (Hopkinson, et al., 2005).

- Medicine and Dentistry:

Accurate parts of surgical implants which fit specific patients are achievable through this manufacturing. In view of the fact that safety and compatibility are critical considerations in this industry, RP provides parts with the exact dimensions made of materials that are compatible with the body environment. 3D printing produces objects of high performance and enhanced mechanical properties. Stratasys is a company that uses polyJet technology to manufacture accurate hearing aids with smooth and comfortable surfaces (Startasys, 2014). Arcam is another company that uses EBM machines to produce patient-specific orthopedic implants with metallic powder (Figure 7(c)) (Arcam, 2013). EBM machines are also used to manufacture porous, root-form, tooth implants, as shown in Figure 7(d). The porous structure has biological compatibility with the surrounding bones and increases bone growth (Gilbert, et al., 2011).

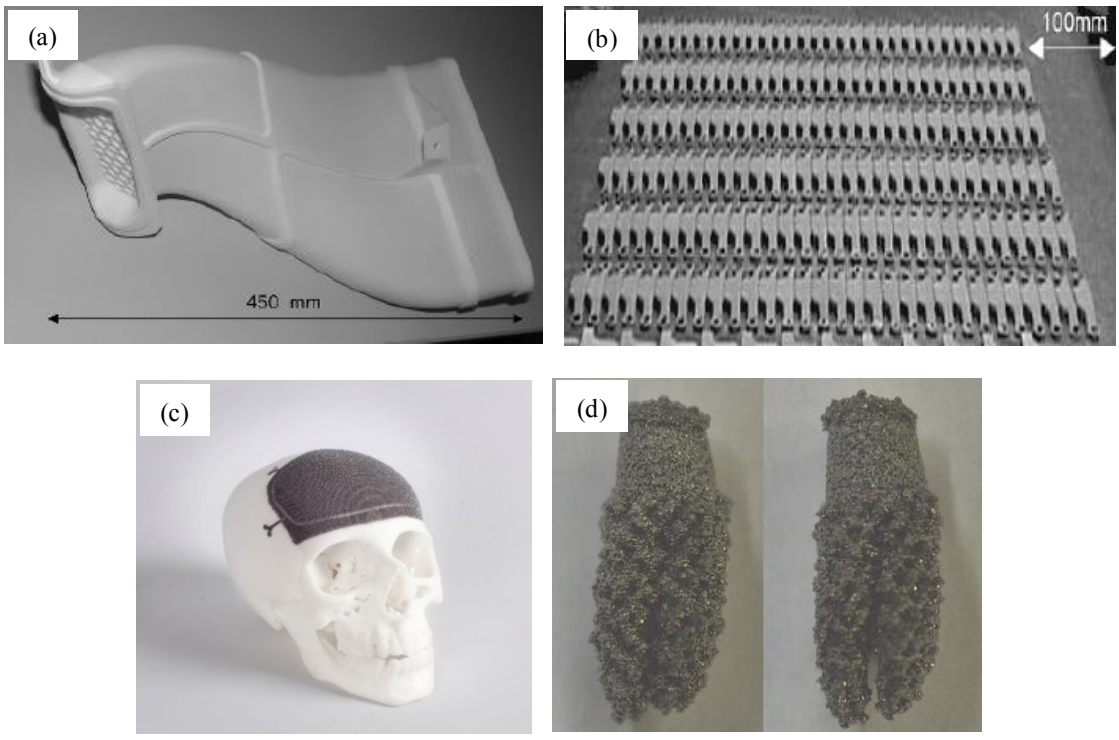

Figure 7: RP applications in different industries **(a)** Automotive: Cooling duct adopted by the Renault team F1 (Hopkinson, et al., 2005). **(b)** Aerospace: Retainers for the international space station (Hopkinson, et al., 2005). **(c)** Medicine: Arcam's orthopedic implant made by EBM machine (Arcam, 2013). **(d)** Dentistry: Bio-adoptable dental root-form implant built by EBM system (Gilbert, et al., 2011).

1.3 The Electron Beam Melting System

1.3.1 EBM Machine

An Electron Beam Melting (EBM) machine utilizes Rapid Prototyping (RP) technology to self-assemble objects by melting the metallic powder. It consists of a control chamber and a build chamber. The build chamber contains the electron beam column and vacuum chamber (Figure 8 (a)). EBM machine can work with conductive metals like commercial pure titanium, Ti-6Al-4V, cobalt-chrome alloy, nickel alloys and other selective metals (Arcam, 2013). RP technology (also known as 3D printing, solid Freeform Fabrication (SFF), and Layered manufacturing (LM)) is based on transferring a computer aided design (CAD) presentation into a fully dense, near the net shape of 3D parts by means of layer-based building.

(a)

(b)

ARCAM A2 TECHNICAL DATA

Build tank volume	250x250x400 mm and 350x350x250 mm (W x D x H)
Maximum build size	200x200x350 mm and Ø 300x200 mm (W x D x H)
Model-to-Part accuracy, long range [1]	+/- 0.20 mm (3σ)
Model-to-Part accuracy, short range [1]	+/- 0.13 mm (3σ)
Surface finish (vertical & horizontal) [2]	Ra25/Ra35
Beam power	50–3500 W (continuously variable)
Beam spot size (FWHM)	0.2 mm – 1.0 mm (continuously variable)
EB scan speed	up to 8000 m/s
Build rate [2]	55/80 cm^3/h (Ti6Al4V)
No. of Beam spots	1–100
Vacuum base pressure	$<1 \times 10^{-4}$ mBar
Power supply	3 x 400 V, 32 A, 7 kW
Size and weight	1850 x 900 x 2200 mm (W x D x H), 1420 kg
Process computer CAD interface	PC
CAD interface	Standard: STL
Network	Ethernet 10/100/1000
Certification	CE

[1] Long range: 100 mm, Short range: 10 mm, measured on Arcam Standard Test Part (ASTP).
[2] Measured on Arcam Standard Test Part (ASTP).
Settings optimized for fine surface quality/Settings optimized for high build speed.

Figure 8: EBM machine **(a)** Arcam A2 machine **(b)** Arcam A2 technical data (Arcam, 2013).

EBM machine (Figure 9) uses electrons as the energy source to melt a metallic powder layer-by-layer to build the required object. An electron gun operates at 60 kV and generates electrons through its

filament. Electrons are then accelerated as they pass by an astigmatism lens and are then focused with a focus lens. In order to obtain the required design, a deflection lens scans the electrons systematically according to the CAD design to melt selected areas of the powder in the building plate. Electrons transfer their kinetic energy to the electrons in the material being melted (Mahale, 2009). After melting each layer, the plate decreases down, the powder hoppers supply a new layer of powder, and the rake moves horizontally between the hoppers to even out the surface of the powder. The process is repeated until the 3D object is fully built.

The manufacturing process occurs at a temperature of around 700°C and a vacuum atmosphere of $1x10^{-5}$ mbar to prevent collision of accelerated electrons with air molecules (Bass, 2007). This controlled environment improves the quality of the produced part as the absence of the air in the chamber allows for a contamination-free environment, and small melt pools which reduces the heat-effected zone. Working under elevated temperatures provides stress-relieved parts and rapid quenching rates reduce segregation so internal stresses are also minimized (Safdar, 2010). As a result of manufacturing in these conditions, microstructure will be affected. In addition, variances in the exterior surface appear and voids form within the sample which will change surface roughness, density and porosity of the produced parts. However, it is possible to control these variations by changing the building parameters of EBM machine.

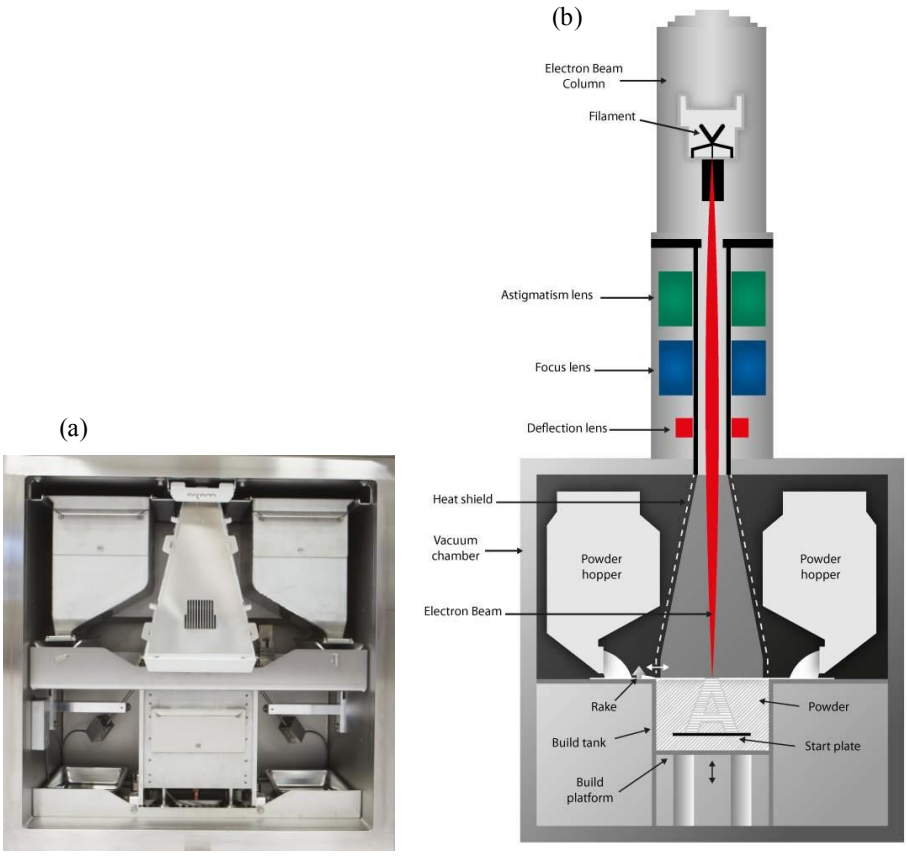

Figure 9: (a) EBM vacuum chamber **(b)** EBM building chamber components (Arcam, 2013).

1.3.2 EBM Build Parameters

Ti-6Al-4V powder is melted with the accelerated electrons at high temperature of 1,900°C. The material's phase transformation and cooling of melted powder passes through three steps:

1) Rapid cooling from the melt temperature, 1,900°C, to build temperature, around 700°C,
2) Holding at temperature around 700°C during the build time, and
3) Slow cooling from 700°C to room temperature when the build is done.

These stages accommodate annealing that helps in stress relief, ductility enhancement, and refining the microstructure to make the part more homogenous.

In addition, the EBM manufacturing process includes other build parameters like scanning speed, beam current (beam energy), offset focus, scanning direction, offset line, and layer thickness. These parameters influence the product's properties such as surface roughness, porosity and density. This is likely due to the fact that different build parameters changes the build environment, and hence, the microstructure is affected as well (Mahale, 2009).

In the present research, three parameters were studied: scan rate, beam current and offset focus. Beam current, or beam energy, is the current of the electrons released in the electron beam. Beam speed is the electrons scan speed, and offset focus is the amount (in mA) by which the beam is defocused from the calibrated position (as was denoted from the manufacturer, North Carolina State University). These parameters contribute to the energy transferred by the electrons per unit length of the material, which is called linear energy. Linear energy (J/m) is the ratio of beam power to the beam speed, beam power is the product of accelerated voltage and beam current. The accelerated voltage for Arcam A2 EBM machine is 60 kV. Previous studies showed that linear energy increases with increasing beam current and with decreasing scan speed and offset focus (Safdar, 2010).

Possible variations in EBM process parameters offer different properties of materials produced. Properties of the finished parts can be controlled by changing the building parameters, as some applications require rough surface-like body implants, whereas others need almost smooth surface to reduce holes that can accumulate impurities, as in pipes and reactors. On the other hand, porosity is an advantage in medical replacements as it has low modulus of elasticity and gives flexibility, while porous material cannot be used for equipment in a chemical unit or for car parts in automobile industry.

Achieving specific properties not only can be done with variations in build parameters; other factors like powder type and its particle size distribution can cause such changes. Powder used in EBM has an average size of 30μm, with size ranging from 10-60μm. By adjusting the powder particle size distribution

when the beam energy and beam scan is set properly, it is possible to vary the dimension of building layers which contributes to the nature of the surface and porosity of the part produced (Gaytan, et al., 2009).

Therefore, to obtain parts that fulfill the purpose they are made for with a good quality and uniform microstructure, a well-designed set of EBM's processing parameters should be chosen.

1.4 Corrosion Overview

1.4.1 Polarization Curve

Corrosion is the destruction or breakdown of material by electrochemical reaction of a material with its surroundings. Electrochemical reactions happening are of one or more oxidation (anodic) and reduction (cathodic) reactions. When the material oxidizes it loses electrons as shown in the anodic reaction (1), and for titanium metal in specific, the anodic reaction is shown in reaction (2):

$$M \rightarrow M^{+n} + ne^{-} \qquad (1)$$

$$Ti \rightarrow Ti^{+3} + 3e^{-} \qquad (2)$$

The electrons can react with the H^{+} in the solution as shown in the following cathodic reaction:

$$2H^{+} + 2e^{-} \rightarrow H_2 \qquad (3)$$

Oxidation causes corrosion of the material. Depending on the conditions and nature of the surroundings, corrosion comes in many forms including: uniform corrosion, galvanic, crevice, pitting, erosion corrosion etc. This present study is related to pitting corrosion where localized attack occurs on the surface of the material causing holes in discrete areas. This is discussed in more details in section 1.6 of this chapter.

As the material oxidizes, a change in the potential of the metal's surface occurs called anodic polarization η_a, while the surface at which electrons are supplied will have a cathodic polarization η_c. Corrosion is measured by the rate of anodic and cathodic reactions which is represented by the corresponding

current densities. Due to the occurrence of anodic and cathodic reactions shown in (1) and (3), the polarizations on the sample's surface are related to the anodic and cathodic current densities according to the Tafel equations (4) and (5), respectively:

$$\eta_a = \beta_a \log\frac{i_a}{i_o} \qquad (4)$$

$$\eta_c = \beta_c \log\frac{i_c}{i_o} \qquad (5)$$

Where i_a is the anodic current density, i_c is the cathodic current density and i_o is the exchange current density which is equal to the reaction rate at equilibrium. β_a and β_c are called Tafel constants for each reaction, which are the slope of the linear region in the polarization curve of potential vs. log current density. The potential at which η_a and η_c are equal is the corrosion potential E_{corr} as shown in Figure 10. At that point, i_a and i_c will be the same and equal to the corrosion current density i_{corr}. Laboratory determination of anodic Tafel constant β_a will gives quantitative estimate of the cathodic potential needed to be applied for cathodic protection of a material (Jones, 1996).

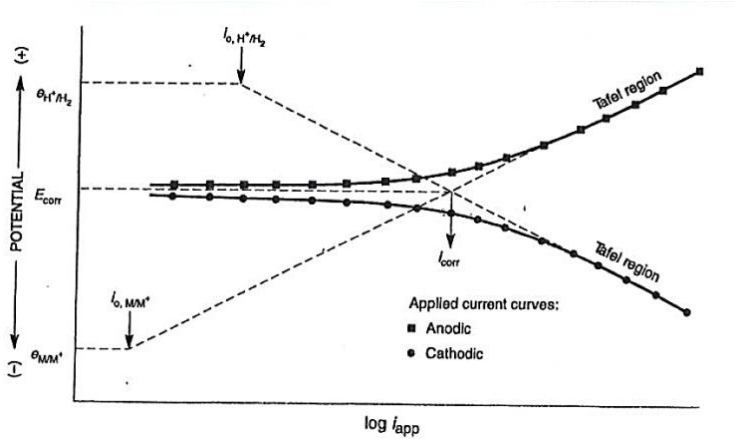

Figure 10: Experimental polarization curve obtained from potentiodynamic test (Jones, 1996).

Corrosion rate is measured by weight loss of coupon samples. This is tested by exposing the coupons to certain environments which are then evaluated to verify quality control specifications and the most economical ways to reduce corrosion (Jones, 1996). Another way to evaluate corrosion is through conducting potentiodynamic and potentiostatic tests. Establishing a polarization curve from a potentiodynamic test (potential scan) can help in obtaining data about the corrosion potential, corrosion rate, pitting potential, passivity region, etc. Moreover, critical pitting temperature (CPT) is another indicator for corrosion resistance of a material. CPT can be determined from conducting a potentiostatic test (constant potential). CPT is the temperature at which pitting starts under specific conditions. It is an indication of the lowest temperature at which the metal's surface is attacked by pitting corrosion under specific test conditions. Both potentiodynamic and potentiostatic tests were employed in the present research.

1.4.2 Reference Electrodes

Conducting potentiodynamic and potentiostatic tests require measuring potential of the corrosion cell. Potential inside a corrosion cell can be measured by a high-impedance voltmeter. Potential is determined as the difference between sample potential and the reference potential. Therefore, all potential measurements are referred to a standard electrode.

The half-cell potential can be calculated using the following Nernst equation (6):

$$E = E_0 - \frac{R\,T}{n\,F} \ln \frac{a_{products}}{a_{reactants}} \qquad (6)$$

Where E is the half-cell potential, E_0 is the standard half-cell reduction potential, R is the universal gas constant, T is the absolute temperature, n is the number of electrons transferred in the half-cell reaction, F is faraday constant, and a is the activity of the species in the solution. Activity can be denoted as pressure in atmospheres for gases and can be approximated by concentrations in moles per liters for many dilute

solutions. Values of constants are calculated at 25ºC and substituted in Nernst equation (6) which becomes as shown in equation (7):

$$E = E_0 - \frac{0.0591}{n} \log \frac{a_{products}}{a_{reactants}} \qquad (7)$$

Electrochemical thermodynamic measurements use the hydrogen electrode as a standard electrode. By definition, the standard hydrogen electrode (SHE) has a potential equal to zero. Reaction (8) represents the half-cell reaction of the hydrogen electrode:

$$2H^+_{(aq,a=1)} + 2e^- \rightarrow H_{2(g,1\,atm)} \qquad (8)$$

Nernst equation for hydrogen electrode can be represented in equation (9):

$$E = E_0 - \frac{0.0591}{2} \log \frac{a_{H_{2(g)}}}{(a_{H^+})^2} = 0 \qquad (9)$$

At standard state it is assumed that the pressure of hydrogen gas is one atmosphere and the concentration of hydrogen ions is one mol/liter, which makes the hydrogen electrode potential equal to zero.

Other secondary reference electrodes that are commonly used are listed in Table 2 with the corresponding half-cell reactions and half-cell potentials. Saturated calomel electrode (SCE) is the most common electrode used in aqueous solutions. It consists of mercury pool in contact with a paste of mercurous chloride (Hg_2Cl_2). The paste is insoluble salt that is also known as calomel which is in contact with saturated solution of potassium chloride (KCl). Solid KCl is added to the KCl solution to maintain the latter saturated in order to keep a constant value for the activity of chloride ions. Figure 11 shows a schematic diagram for calomel reference electrode.

Table 2: Potential values for common secondary reference electrodes (Jones, 1996).

Name	Half-Cell Reaction	Potential V vs. SHE
Mercury-Mercurous Sulfate	$HgSO_4 + 2e^- = Hg + {SO_4}^{2-}$	$+0.615$
Copper-Copper Sulfate	$CuSO_4 + 2e^- = Cu + {SO_4}^{2-}$	$+0.318$
Saturated Calomel	$Hg_2Cl_2 + 2e^- = 2Hg + 2Cl^-$	$+0.241$
Silver-Silver Chloride	$AgCl + e^- = Ag + Cl^-$	$+0.222$

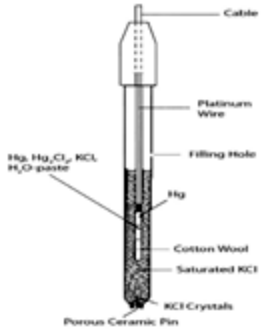

Figure 11: Schematic drawing for calomel reference electrode (Jones, 1996).

Saturated calomel reference electrode has the half-cell reaction represented in equation (10), and Nernst equation for calomel electrode can be represented in equation (11):

$$Hg_2Cl_2 + 2e^- \rightarrow 2Hg + 2Cl^- \qquad (10)$$

$$E = E_0 - \frac{0.0591}{2}\log\frac{a_{Hg_2Cl_2}}{(a_{Hg})^2(a_{Cl^-})^2} = +0.241 \qquad (11)$$

where the activity of elements and compounds species are equal to one and the activity of ions in saturated solutions is equal to 10^{-6} mol/liter. The saturated calomel reference electrode used in the present research with a potential of +0.241 V.

1.5 Corrosion of Titanium Alloys

1.5.1 Corrosion Resistance of Titanium Alloys

Wide usage of titanium and its alloys in many applications like aerospace, marine and chemical industry is due to their unique attractive combination of engineering properties. Corrosion resistance of titanium in various media is one of these properties, and it is due to the formation of a very stable and continuous film layer on the surface of the metal.

Titanium and its alloys are resistant to water and steam up to 315°C. Contaminants like iron, manganese oxides, sulfates, sulfides, carbonates and chlorides do not affect passivation of the alloy. In seawater where several hundred traces of chloride are present, crevice corrosion can take place at temperatures above 75°C. On the other hand, negligible corrosion rates (for uniform corrosion) in seawater is observed for titanium alloys up to 260°C. The marine environment with splashes and soils does not affect titanium resistance as well. Specifically speaking, Ti-6Al-4V maintains extremely low corrosion rates after three years of exposure to ambient seawater (Schutz, 2005b).

Corrosion of Ti-6Al-4V is observed to increase with increasing NaCl concentration. Some proteins like egg albumin and bovine serum, work as corrosion inhibitors due to the formation of a thick and compact layer on the alloy's surface (Abou Shahba, 2011). Commercially pure titanium has better corrosion resistance than Ti-6Al-4V in boiling nitric acid solution (Robin, et al., 1999). Excellent corrosion resistance of pure titanium was observed when it was tested in 5.2 M NaCl solution at different temperatures. The anodic part of the polarization curves shown in Figure 12 had a passive region that extended through a potential range of 2,000-5,000 mV (Branzoi, et al., 2005). The anodic curve reached to a high potential of

5,000 mV without having any pitting corrosion which is much higher than 700 mV, the value of the pitting potential for most stainless steels (ASTMG150-99, 2010).

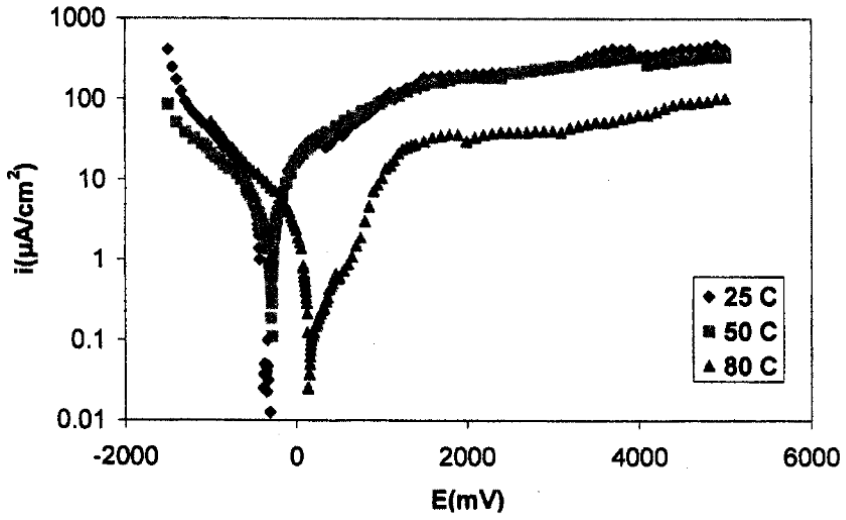

Figure 12: Polarization curves of pure titanium in 5.2 M NaCl at different temperatures (Branzoi, et al., 2005).

Corrosion of Ti-6Al-4V was investigated by Gurrappa in chemical, marine and industrial media at different temperatures. Figure 13 shows cyclic polarization curves of Ti-6Al-4V at 25 and 50℃ in these different media. Ti-6Al-4V was resistive to both crevice and pitting corrosion in the chemical and marine environments at these temperatures; the reverse scan of the chemical environments rose above the forward scan and the reverse scan of the marine environments came almost following the forward scan. On the other hand, the reverse scan was below the forward scan for industrial environment indicating that Ti-6Al-4V is susceptible to crevice and pitting corrosion at both temperatures. Even the alloy might degrade at both temperatures in marine and chemical environments but the mode of degradation will be due to uniform corrosion not pitting or crevice corrosion. The corrosion rate in the chemical environment was the highest, while the rate had the lowest value for marine environment (Gurrappa, 2003).

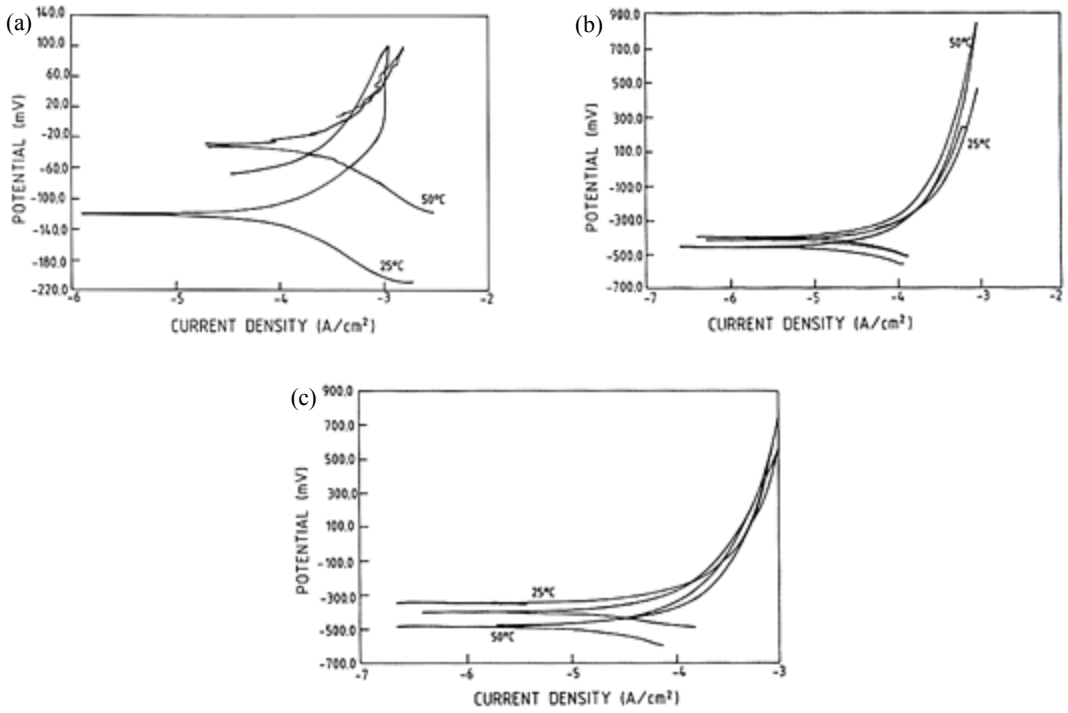

Figure 13: Cyclic polarization curves of Ti-6Al-4V alloy at different temperatures in different environment **(a)** Chemical environment. **(b)** Marine environment. **(c)** Industrial environment. (Gurrappa, 2003).

Abdulmageed et al. studied corrosion of Ti-6Al-4V in different media of chloride, hydroxide, carbonates and acids. Table 3 shows some corrosion properties of Ti-6Al-4V in different media. It was determined that Ti-6Al-4V has corrosion resistance as shown in the following sequence (Abdulmageed & Ibrahim, 2010):

Sodium Chloride (NaCl)> Sodium Hydroxide(NaOH) > Acetic Acid (CH_3COOH) > Phosphoric acid (H_3PO_4) > Sodium Carbonate (Na_2CO_3).

Table 3: Corrosion properties of Ti-6Al-4V in different media (Abdulmageed & Ibrahim, 2010).

Medium	Corrosion Potential $-E_{corr}$(mV) (SCE)	Corrosion Current Density i_{corr} ($\mu A.cm^{-2}$) $*10^{-3}$	-bc ($mV.dec^{-1}$)	+ba ($mV.dec^{-1}$)	$R_p x10^{-7}$ ($\Omega.cm^{-2}$)
NaCl	148.26	1357.6	113.0	206.6	0.2330
Sodium tartarate	1317.3	160.68	199.3	666.5	4.1460
NaOH	1029.2	114.83	221.7	741.3	6.4530
Sodium Oxalate	1324.2	75.48	261.7	678.9	10.866
Acetic acid	736.8	63.95	171.5	333.5	7.6900
Phosphoric acid	639.9	63.91	216.3	452.5	9.9420
Na_2CO_3	1319.9	61.43	225.9	862.0	12.652

Furthermore, Martin et al. showed in experimental work that different phase composition, texture and microstructure influence the corrosion resistance of Ti-6Al-4V. These investigators prepared the alloy to different microstructures of ά martensite, α lamellar and (α+β) equiaxed structure. Each condition resulted in different corrosion rates with the equiaxed structure exhibiting the best corrosion resistance. ά martensite structure was of better corrosion resistance than α lamellar structure since the lamellae structure enhances the formation of microchemical galvanic cells at the interface which leads to corrosion. In addition, XRD of these samples showed some β phase in α lamellar, while no β was detected in ά martensite structure. Lower β phase (or no β phase) indicates better passivation as more resistant oxides form on surface of the specimen, giving better corrosion resistance. Equiaxed (α+β) structure corrosion resistance comes from the absence of a lamellar structure. Even if material with equiaxed structure has some β phase (less than α lamellar) it still has better resistance than ά martensite. This is due to the random distribution of β phase in the form of isolated nodular particles on the boundaries of α particles (Martin, et al., 2010).

1.5.2 Passivation of Titanium Alloys

Strong immunity of titanium and its alloys is a result of the development of a very steady, coherent, and highly adhesive oxide layer. Corrosion rates of titanium decrease with time of exposure to the surroundings, which indicates the finite growth of this layer. This layer is very protective as if it was damaged it can heal

itself immediately even if there were only traces of oxygen (few parts per billion) present in the surroundings (Schutz, 2005a).

The nature, composition and thickness of the oxide layer depends on the surroundings. Normally, titanium oxides form in most environments. Additionally, the surface layer can be a mixture of other oxides like Ti_2O_3 and TiO. To understand the nature of oxides formed in different environments, a pourbaix (Potential-pH) diagram for a titanium-water system at 25°C is constructed (Figure 14). This diagram is based on free-energy of formation of metallic oxides at different pH levels. These thermodynamic calculations help in predicting oxide stability based on the pH and potential of the surroundings. The area between the dashed lines represents the stability region for water. In this area, the titanium is passive with TiO_2 formation over the full range of pH, whereas Ti_2O_3 is formed in mild reducing conditions. Hence, titanium alloys can resist corrosion in mildly reducing to highly oxidizing environments with protective TiO_2 or Ti_2O_3 oxide layers, while corrosion takes place in strongly acidic reducing environments (Schutz, 2005b).

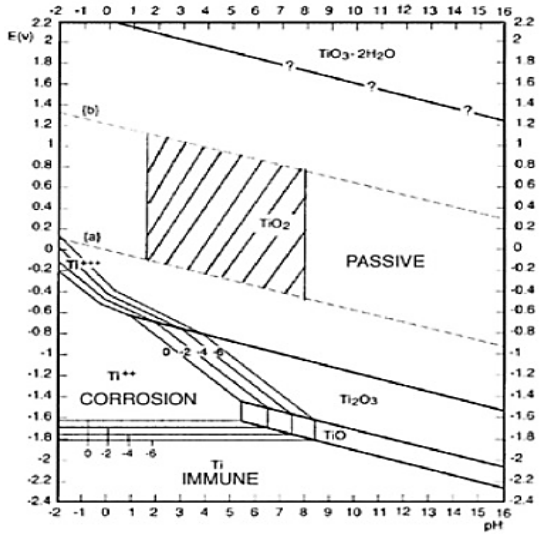

Figure 14: Pourbaix diagram for titanium-water system at 25°C (Schutz, 2005b)

Alloying the titanium might increase the corrosion rate of the alloy, but it will maintain its high corrosion resistance even in acidic environments. Figure 15 shows polarization curves for different titanium

alloys in deaerated NaCl and HCl solutions. It can be noted that titanium alloys are spontaneously passive even in acidic environments due to the formation of very stable oxide layer on the alloy's surface (Yu & Company, 2003).

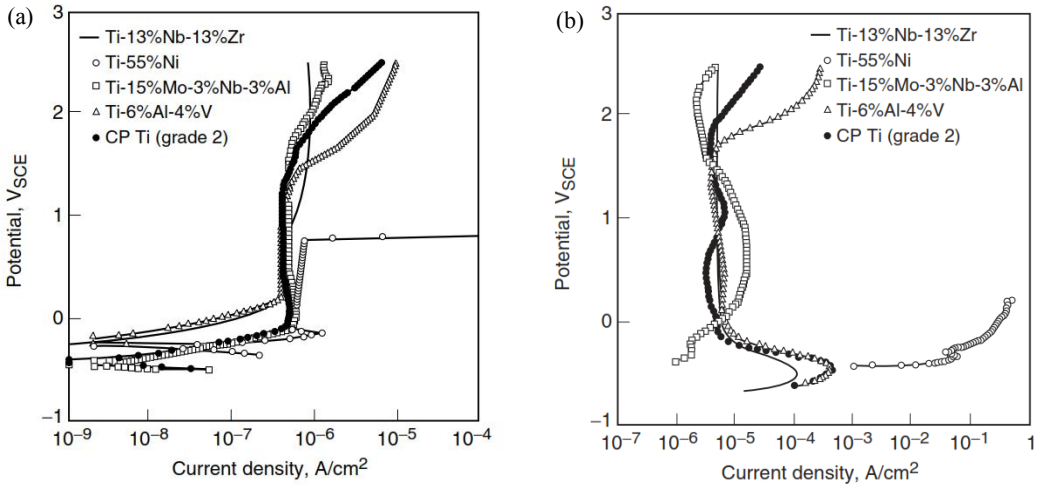

Figure 15: Polarization curves of titanium alloys indicating strong passivity in different solutions **(a)** Deaerated 0.1 NaCl solution. **(b)** Deaerated 0.1 HCl solution (Yu & Company, 2003).

1.6 Pitting Corrosion

1.6.1 Pitting Mechanism

Pitting corrosion is a form of localized attack that occurs on the open exposed areas of the passive film which results in penetration of the metal surface at discrete areas. It happens when the metal's potential exceeds the pitting potential of that metal in the given environment (Schutz, 2005b). Pitting forms holes of different diameters and depths that can be covered with oxides, which makes it difficult to detect. Mechanical damage of the surface like scratches, stress in the form of dislocations, and coating discontinuity initiates pits and causes a breakdown of the passive film. Once pits are initiated, metal is exposed to the electrolyte allowing pits to propagate yielding accelerated dissolution of the metal. Pitting corrosion is considered more dangerous than uniform corrosion as its rate of growth is 10-100 times faster (Jones, 1996).

Pitting corrosion is an electrochemical oxidation-reduction (redox) process that happens within the holes on the surface of the passive film. Even though titanium is highly resistant to corrosion in NaCl solutions (Schutz, 2005b), when its potential exceeds the pitting potential in chloride solutions, pitting occurs.

Pitting corrosion occurs in two stages: pit initiation and pit propagation. Figure 16 shows a schematic presentation of pitting corrosion happening on the surface of titanium metal.

Pit initiation

In aerated NaCl solutions, titanium reacts with dissolved sodium chloride and forms soluble $TiCl_3$. Titanium dissociates into Ti^{+3} ions and loses electrons as in the anodic reaction (2). Hydrogen ions in the solution react with the evolved electrons and form a hydrogen gas as in the cathodic reaction (3). Pits begin in acidic environments when the potential increases above a certain value called pitting potential (E_{pit}). In aerated environments, dissolved oxygen acts as an oxidizing agent that is reduced by reacting with water as in reaction (12). This reaction causes an increase in site potential (Jones, 1996):

$$O_2 + 2H_2O + 4e^- \rightarrow 4OH^- \qquad (12)$$

With the continuous reduction of oxygen, potential can increase to a value higher than E_{pit}. At the same time, the metal oxidation causes an increase in chloride ion concentration inside the pit that balances the increase in Ti^{+3} ions to maintain charge neutrality within the pit. This in sequence leads to the following hydrolysis reaction (13):

$$4Ti^{+3} + 6H_2O + O_2 \rightarrow 4TiO_2 + 12H^+ \qquad (13)$$

Therefore, the solution inside the pit becomes acidic. As previously noted, when the potential increases to a value higher than E_{pit}, and in low pH environment, an active corroding anode inside the pit is created as shown in Figure 16. The pit is then initiated with the liberation of Ti^{+3} by increasing the rate of

the anodic reaction, then more metal dissociation occurs (Jones, 1996). The presence of chloride ions boosts this process significantly (Figure 17). Chloride ions have high diffusivity due to their relatively small size which enables them to interfere with the passivation process causing penetration of the outer surface of passive film (Frankel, 2003). This will initiate a pit and allow the pit to grow more in such an acidic chloride environment.

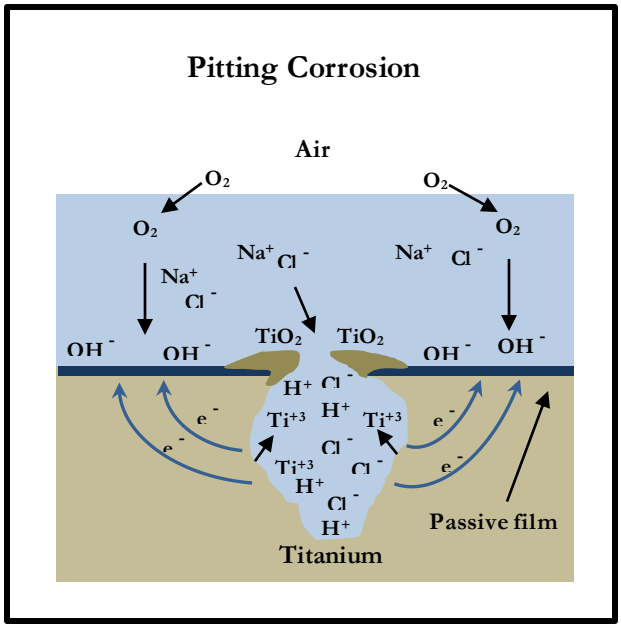

Figure 16: Schematic draw for pitting corrosion of titanium.

Pit propagation

A pit propagates as the hydrolysis reaction continues and more corrosion products are formed. As shown in Figure 16, TiO_2 forms a porous cap on the mouth of the pit that maintains an acidic environment inside the pit. Titanium ions Ti^{+3} can migrate through this cap to the exterior of the pit for further hydrolysis, whereas Cl^- ions migrate to the interior of the pit. This way, anodic regions are maintained inside the pit allowing it to grow, while the cathodic region is preserved outside the pit on the surface of the passive film where oxygen is more concentrated.

1.6.2 Pitting Potential

Pitting potential (E_{pit}) –or sometimes called breakthrough potential, is the potential at which pits appear on metal's surface in a given environment. This quantity is a measure of metal's resistance to pitting corrosion. When the potential on the surface of metal exceeds the pitting potential for that metal in a specific surroundings, pitting occurs. Pitting potential can be detected using potentiodynamic test. Figure 17 shows that the anodic current is increasing at low potentials which indicates an active state of the material where corrosion occurs. When the current is constant with increasing potential then the material is in the passive state and low rates of corrosion is detected due to the formation of oxide layer on the surface. When part of the protective layer breaks down, corrosion occurs, and the current increases rapidly and keeps increasing at all potentials. The potential at which this current increase occurs called pitting potential (E_{pit}). As shown in the same figure, presence of chloride ions enhances corrosion so that E_{pit} for environments without chloride ions is higher than that for environments with the chloride ions. Explicitly speaking, presence of chloride ions in acidic environments can cause a potential increase on the metal's surface. If this increase exceeds the pitting potential limit, oxidation of the metal occurs (Jones, 1996).

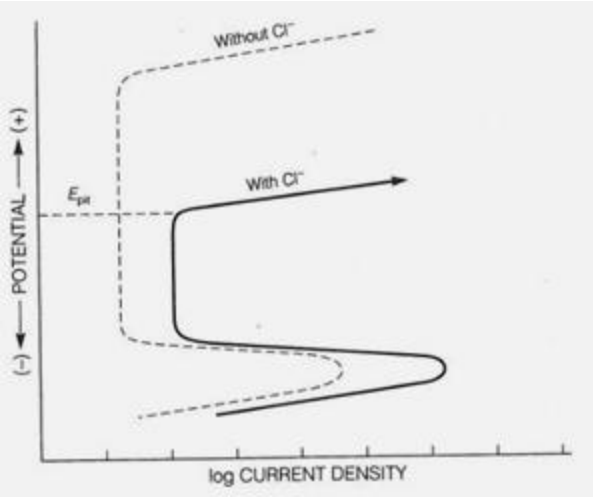

Figure 17: Pitting potential from potentiodynamic test with and without the presence of chloride ions (Jones, 1996).

1.6.3 Critical Pitting Temperature (CPT)

Pitting corrosion is characterized by the presence of discrete holes on the surface of material. Adjacent areas on the same surface remain unaffected. Pits can have different shapes; they can be shallow, deep, elliptical, vertical, horizontal, etc. The evaluation of pitting corrosion is done by analyzing the morphology of these pits. Pits can be classified according to their pit density (spacing), surface size, and depth of pits and then compared with well-defined standards. However, this procedure becomes tedious and time consuming when there are several samples to examine. Hence, a maximum pit depth measurement was adopted as the preferred way to assess and compare pits. Measuring maximum pit width can be done using various methods such as, microscopic, metallographic, machining and micrometer depth gauge (Jones, 1996). Yet, these methods identify the appearance of the pits after the occurrence of the attack, and none can predict when it will start or the conditions which increase its possibility to initiate.

Critical pitting temperature (CPT) is another way to evaluate pitting. CPT is the temperature at which the protective oxide layer starts to break up in certain surroundings. It is an indication of the lowest temperature at which the sample surface will be attacked under specific test conditions. It is a more practical indicator than the above mentioned methods, because it allows for testing under different environments and can give predictions of pitting occurrence, thus helping in taking the right precautions before the occurrence of pitting.

CPT can be measured using different procedures; the two most familiar ones are the potentiostatic test at constant potential, and the potentiodynamic test at different temperatures. Electron impedance spectroscopy is another method that proved to give close results to potentiostatic test (Ebrahimi, et al., 2012). Potentiostatic test procedure is the most used one currently as it is more practical than performing several potentiodynamic tests at different temperatures. In addition to saving time and samples needed for the test, potentiostatic test has a precision of ± 2ºC or less and is close to that of potentiodynamic test (Arnvig & Bisgard, 1996). For these reasons, a potentiostatic test was chosen in the present study to detect the CPT of Ti-6Al-4V samples produced from EBM machine, and ASTM standard G150-99 (2010) was implemented

to do this test (ASTMG150-99, 2010). CPT test used here to give indications of corrosion resistance of EBM Ti-6Al-4V and to compare this resistance with wrought of the same alloy.

Potential for potentiostatic test

Potentiostatic test for measuring CPT is to be performed under constant potential. The proposed potential in G150-99 (2010) standard is 700 mV or 800 mV versus SCE (Saturated Calomel Electrode). As the above mentioned standard is for stainless steels and the samples produced from the EBM are titanium grade 5 (Ti-6Al-4V), an adjustment of the pitting potential had to be done due to the fact that titanium has higher corrosion resistance than stainless steels. While pitting potential for most metals is less than +1 V versus SCE, titanium and its alloys form a protective oxide layer which increases the value of this potential depending on the media (Schutz, 2005a). In chloride solutions, titanium alloys have a pitting potential value ranging between +2 to +10 V versus SCE depending on solution chemistry (acidity and ions contained), solution temperature, alloy composition, potential scan rate and surface conditions (Schutz, 2005b).

Finding the right pitting potential for potentiostatic test is necessary since CPT value can vary if it is in CPT potential dependent range (Arnvig & Bisgard, 1996). Figure 18 shows the relation between potential and temperature. In general, the pitting potential decreases with increasing temperature. Below CPT potential independent temperature no pitting occurs, only passive or transpassive corrosion. For temperatures higher than this, CPT will vary according to the potential and it is in a CPT potential dependent range. Above pitting potential range and below the transpassive region pitting occurs simultaneously, while below the pitting potential range no pitting will be observed.

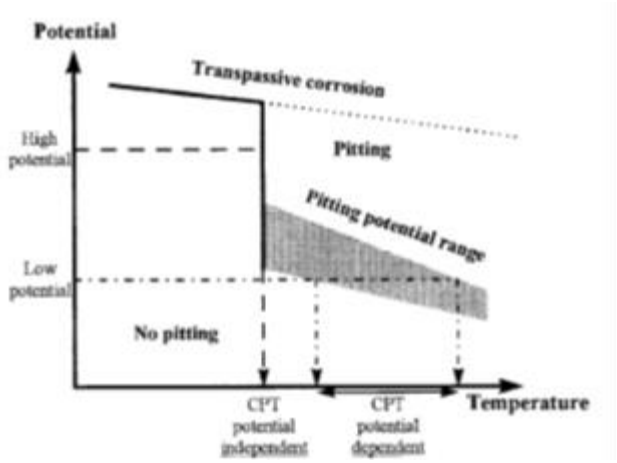

Figure 18: Relation between pitting potential and CPT (ASTM G150-99, 2010).

Practically, pitting potential for potentiostatic test can be determined with conducting potentiodynamic (potential scan) test at different temperatures (Arnvig & Bisgard, 1996). It requires the test to be conducted at low scan rates of ≤ 0.5 mV and consideration of surface conditions of the tested samples (Schutz, 2005b). From each potentiodynamic test, E_{pit} is corresponding to the potential at which the anodic current density increases abruptly and remains high at all potentials as Figure 17 shows (Jones, 1996). Pitting potential versus temperature is plotted, and a curve similar to Figure 18 is obtained. Constant potential for the potentiostatic test has to be above the pitting potential range and below the transpassive potential (ASTM G150-99, 2010).

CHAPTER II

RESEARCH PROBLEM AND OBJECTIVES

Rapid prototyping (RP) is a recent technology that has been playing an increasingly important role in many industrial applications. With a convenient CAD model, RP technology saves time while manufacturing intricate objects. RP avoids molding, machining and tooling, and eliminates constraints imposed by these conventional manufacturing methods.

RP has achieved significant developments in different sectors of industry; from hip and joints implants in the medical sector, to rocket engine impeller in aerospace and intricate gear box casing of a race car in the automobile industry. In the automobile industry, RP technology saved one of the most competitive race teams in NASCAR race. The car's duct outlet was not supplying air to the tire, which resulted in overheating then blowing out of the tire. The conventional method would have taken several weeks to solve the problem, but with RP, a new outlet duct was designed, validated, and manufactured in 56 hours and kept this team on track (Engineer, 2011). In the field of aerospace, Wyle's Integrated Science and Engineering Group in Houston cooperated with NASA in preparing the Robonaut 2 (R2) as a helping hand robot for launch to the International Space Station (ISS). Conventional machining estimations for the parts of this model required eight months to prepare with a cost of $180,000. Instead, RedEye was able to prepare all the required parts with RP technology only in two weeks with a cost of $36,000 (RedEye Australia, 2014). Another recent innovation for RP in aviation is the light-weight and high-speed ICON aircraft. Eight specially-designed air ducting parts of this aircraft were created using RP without the need for any tooling process. Some parts of this aircrafts were seven feet long with 0.06 inch thickness to maximize handling with a minimum weight. In addition, extra features were added like intricate turning vanes inside the ducts to bring outside air to cool the engine, which would not been achievable without complex tooling (RedEye, 2013). RP allows for patient-specific implants without any design constraints for parts to be manufactured

within several hours. The high-quality objects produced with RP are of light-weight and can be made of complex geometry, and yet maintain their compatibility and safety features.

An Electron Beam Melting (EBM) machine utilizes RP technology to fabricate parts with the metallic powder of Ti-6Al-4V. An EBM machine enables manufacturing complex 3D objects from a CAD presentation through fusing thin layers of a material, one layer at a time. The manufacturing process involves extreme conditions such as high temperature, vacuum atmosphere and rapid thermal quenching of the molten metal to nearly room temperature in just a few seconds. Due to unique characteristics Ti-6Al-4V alloy of being lightweight, having strong corrosion resistance, great biocompatibility and high strength-to-density ratio, object fabricated in an EBM machine is utilized in many industrial applications.

The broad objective of the present study is to evaluate a Ti-6Al-4V alloy produced in an EBM machine. This evaluation is achieved through electrochemical testing for corrosion examination and through measuring surface roughness, critical pitting temperature, density and porosity of EBM parts and relating these properties to the EBM's processing parameters.

Due to the technique in manufacturing, voids created within the produced parts and exterior surface of the product have rough edges since the metallic powder melts in a layer-based procedure. This contributes to the roughness and porosity of the produced part. Surface irregularities allow the formation of stagnant regions that might initiate pits within surface folds. While voids cause weak points throughout the protective oxide layer, thus this is expected to affect corrosion properties of produced parts. Moreover, as the machine can run under different processing conditions, it would be possible to have an optimal set of conditions that produces parts of specific properties so as to accomplish the purpose of application it is used for. For example, parts for medical applications are preferred to be of a relatively rough surface so that tissue grows and adheres to the surface. However, a rough surface can cause corrosion and fracture of pipes, which is not desirable for industrial applications. On the other hand, setting certain process parameters might result in a porous structure, which is not an appropriate property when building parts for a car or airplane. Therefore,

choosing the right process parameters is an essential step in the EBM manufacturing process. The following are the main objectives with the key questions addressed by the present research:

- Examining corrosion resistance of the produced part: Does a Ti-6Al-4V part produced with an Arcam A2 EBM machine maintain its corrosion resistance after manufacturing? What is the maximum limit of temperature and potential the EBM part can withstand before it pits? How does this resistance compare to a conventionally-produced alloy like wrought Ti-6Al-4V?
- Relating properties of the produced part to EBM processing parameters: Does changing processing parameters affect surface roughness, density and porosity of produced part? If so, how does these parameters change the properties of EBM parts? Is there a way to control properties of these parts for a specific application? Is there a model equation that can define the relation between processing parameters and EBM properties?

Achieving the first objective was done by conducting two kinds of electrochemical tests: potentiodynamic and potentiostatic tests. Potentiodynamic and potentiostatic tests were conducted in 3.5 % mass NaCl solution to detect the pitting potential (E_{pit}) and critical pitting temperature (CPT), respectively. Pitting potential and critical pitting temperature give indication for the conditions under which pitting corrosion of Ti-6Al-4V will start to take place. The potentiodynamic test was conducted at room temperature to give an overview of the corrosion behavior of EBM alloy through its polarization curve. Also, pitting potential at different temperatures was determined with potentiodynamic testing. The potentiostatic test was conducted at the same potential recommended by the ASTM standard G150-99 (2010). This standard is for stainless steels and it uses a constant potential of 800 mV vs. SCE (Saturated Calomel Electrode). Moreover, potentiostatic tests were performed under 800 mV vs. SCE on EBM's Ti-6Al-4V in NaCl solutions of different pH to determine their effect on CPT value. For comparison purposes, both tests were done for wrought Ti-6Al-4V as well.

The second objective was accomplished through fabricating samples from Arcam A2 machine under different processing parameters of beam current, beam speed, and offset focus. A statistically designed experiment was used for this purpose. EBM samples were tested, and surface roughness, CPT, density and porosity of produced parts were obtained. Surface roughness was measured using a 3D profilometer. The potentiostatic test was performed under high potential of 2,400 mV vs. SCE to be able to detect the CPT. A glass pycnometer with a vacuum setup was used to measure the density of samples manufactured, and densities obtained were used to calculate porosity of samples. Finally, Minitab software was used to establish a model equations that relate significant processing parameter/s to the measured properties.

CHAPTER III

LITERATURE REVIEW

3.1 Rapid Prototyping Historical Development

Rapid prototyping (RP) technology fabricates near-net-shape objects from a computer aided design (CAD) model by means of layer-based building. Prototyping is a word that means copying or developing of the first example or model, and rapid prototyping is the physical implementation of prototyping. As it requires a computer design representation, RP development has been closely related to the widespread use of computers in industry and the decline of computer's cost.

Prototyping processes have gone through three phases of development: manual prototyping, soft or virtual prototyping, and rapid prototyping. The last two phases have been developed only in the last 30 years and the third phase is still being developed (Chua, et al., 2003). Manual prototyping began when simple tools were being fabricated manually. These prototypes consisted of simple products to help with everyday living and were not sophisticated. The fabrication process consumed time and used labor extensively. With the introduction of computer programs like CAD in the early 1980's, soft, or virtual prototyping, allowed for computer models of tools to be tested and analyzed as if they were actual physical objects. In virtual prototyping, a computer model can be assigned physical and mechanical properties of certain material like steel, then the model can be virtually created for kinematic/dynamic analysis. Virtual prototypes are more complex than manual fabrication, however they take a longer time to produce as they are still made from a craft-based method and need to be tested prior to application. Also, while virtual prototypes are not physical objects, there is still no guarantee that a fault-free prototype will be produced. Rapid prototyping, the third phase of prototype development, has caused a major revolution because computer programs can be utilized to manufacture a 3D physical object. The same complexity can be achieved, but with tremendous time and labor savings, and the prototypes can still be used for physical testing. In 1988, first commercial RP system

was developed. Since then, more than twenty different RP techniques have been established (Chua, et al., 2003).

3.2 Previous Research on Parts Produced from EBM Machine

3.2.1 Materials Applied in EBM Machine

Improving the properties of a manufactured part is a major concern in RP technology, and the type of material involved plays a major role in this regard. The electron beam melting (EBM) machine is a powder-based RP system that uses metallic powder. For purposes of enhancing the functionality of fabricated parts, more than one material was tested in this machine. Arcam is a leading company that utilizes this system to fabricate complex and efficient parts for specialized industries like aerospace and medicine. Arcam recommends using the following powder-based alloys: Ti-6Al-4V, Ti-6Al-4V ELI (extra low interstitial), Cobalt-Chrome and Titanium grade 2 (Arcam, 2013).

Only a few studies have introduced other alloys in the EBM machine. **Mahale** from North Carolina State University investigated the feasibility of using some aluminum alloys and copper alloys in this machine. Gamma titanium aluminide (γ-TiAl), aluminum-7075 and aluminum-2024 were tested in an EBM machine. γ-TiAl has exceptional properties at elevated temperatures, but its low ductility at ambient temperatures makes it difficult to process by conventional methods. After testing different process parameters of the EBM machine, it was found that γ-TiAl can be used with controlled process parameters of the machine and some pretreatment processes of the powder used in manufacturing. However, using aluminum-7075 alloy in the EBM machine produced parts with some problems in porosity and in maintaining the alloy's composition of the finished part. This is due to the difference in melting points of the alloy metals; zinc and magnesium vaporize in a range of 200-300°C, while aluminum vaporizes at around 660°C. The difference in melting points caused heavy evaporation of zinc and manganese at higher temperatures, which made it difficult to keep the composition limit of the aluminum-7075 alloy (Mahale, 2009).

The other alloy that was first tested by **Mahale** is copper alloy GRCop-84 with a composition of 87.22% mass copper, 6.78% chrome and 6.00% niobium. As GRCop-84 has the capability of retaining strength even with high thermal gradients, it was intended to be used in high temperature applications in aerospace like the space shuttle combustion chamber. However, agglomeration and precipitation of particles made it almost impossible to process parts made of this alloy with the conventional methods, whereas the EBM machine with its small melting pool and rapid cooling method might be a preferred process for such an alloy.

Copper alloy GRCop-84 parts produced from the EBM has similar mechanical properties as extruded parts at elevated temperatures. However, lower mechanical properties were obtained at cryogenic and room temperatures. This was associated with the thermophysical properties of the alloy such as thermal conductivity, melting point and latent heat of fusion. These properties should be considered and are related to process parameters that might be adjusted accordingly to improve part properties. Mahale performed simulations of process parameters using Arcam's software to determine the required process parameters. GRCop-84 can be used in EBM machine to fabricate complex components for high-temperature applications, while further study needs to be done to specify optimal process parameters for low-temperature applications (Mahale, 2009).

Ackelid from Arcam performed another feasibility study using aluminum alloy 6061 in the EBM machine. Besides the large loss of magnesium in the produced part, a long vertical crack propagated along the grain boundaries of the part. Therefore, aluminum parts can be obtained with an EBM machine, but proper process parameters should be investigated to accomplish parts of acceptable strength, porosity and alloy composition (Ackelid, 2006).

Ti-6Al-4V is the most commonly used alloy in the EBM machine. **Bass** performed some mechanical and microstructural tests on samples fabricated in Acram's EBM S12 machine to validate the manipulation of Ti-6Al-4V alloy in this type of manufacturing (Bass, 2007). Table 4 shows a comparison of the averages of selected mechanical properties for Ti-6Al-4V produced by the EBM and other traditional

methods. The EBM alloy was tested under different build orientations of XY, XZ and YZ. The yield strength and ultimate tensile strength values obtained for Arcam's EBM samples exceeded the minimum requirements for the same alloy fabricated by cast or laser deposition method. The percent elongation of the EBM sample was the same as the percent elongation specifications of the same alloy made by the forged method. In addition, hardness values of EBM samples were the same as a typical Ti-6Al-4V alloy fabricated by the previously mentioned methods (Table 5) (Bass, 2007).

Table 4: Comparison of the averages of selected mechanical properties for Ti-6Al-4V samples produced by EBM machine and other traditional methods (Bass, 2007).

	Process	UTS (ksi)	Yield Strength (ksi)	%Elongation	Fracture Strength (ksi)
XY Average	Arcam EBM	156.75	146.59	10.76	153.88
XZ Average	Arcam EBM	156.83	149.64	8.93	152.98
YZ Average	Arcam EBM	152.54	138.63	15.02	144.34
AMS-T 9047[1]	Forged, Square, <.5 in^2	165.00	155.00	10.00	
AMS-T 81915[2]	Cast	125.00	115.00	8.00	
AMS 4999[3]: (x direction)	Energy Beam Process	130.00	116.00	4.00	
(y&z direction)	Energy Beam Process	122.00	108.00	4.00	
AMS 4985C[4]: (separately-cast)	Cast	130.00	120.00	6.00	
(integrally-cast, designated areas)	Cast	130.00	120.00	6.00	
(integrally-cast, nondesignated areas)	Cast	125.00	108.00	4.50	

1. AMS-T 9047: Titanium and Titanium Alloys, Bars (Rolled or Forged) and Reforging Stock, Aircraft Quality
2. AMS-T 81915: Titanium and Titanium-Alloy Castings, Investment
3. AMS 4999: Titanium Alloy Laser Deposited Products 6Al-4V Annealed
4. AMS 4985C: Titanium Alloy, Investment Castings 6Al-4V 130 UTS, 120 YS, 6% EL Hot Isostatically Pressed Anneal Optional or When Specified

Furthermore, **Bass** measured fracture toughness of EBM samples for horizontally oriented samples (XY) as well a vertically oriented samples (XZ). Average fracture toughness values were 39.51 ksi-$in^{1/2}$

(1,709.26 MPa-$m^{1/2}$) and 41.02 ksi-$in^{1/2}$ (1,774.59 MPa-$m^{1/2}$) for the horizontal and vertical specimens, respectively. The fracture toughness for traditionally fabricated Ti-6Al-4V was in the range of 30-90 ksi-$in^{1/2}$ (32.965 - 98.896 MPa-$m^{1/2}$). Even the fracture toughness of the EBM samples were close to the lower limit of that range –according to the powder preparation process, but the required specifications were still met. In conclusion, Ti-6Al-4V samples produced with the EBM technique met the minimum material requirements for a traditionally manufactured alloy specifications. Thus, Ti-6Al-4V is acceptable to be used in the EBM fabrication processes (Bass, 2007).

Table 5: Comparison of the averages of hardness values for Ti-6Al-4V produced by the EBM machine with typical Ti-6Al-4V alloy (Bass, 2007).

Specimen	Plane	Average Hardness (Rockwell C)	Standard Deviation
XY	Face	39.0	1.31
XY	Edge	37.0	0.60
XY	Cross-Section	36.6	1.74
YZ	Face	35.6	0.99
YZ	Edge	36.3	1.20
YZ	Cross-Section	37.1	0.77
XZ	Face	35.5	0.00
XZ	Edge	36.7	1.15
XZ	Cross-Section	38.2	1.04
Typical Ti-6Al-4V Alloy		36.0[1]	

1: Source-Titanium Information Group

3.2.2 Mechanical Properties, Microstructure and Surface Analysis of Ti-6Al-4V Produced with Electron Beam Melting System

Mechanical properties are closely related to the Microstructure of the material. For this reason, most of the studies conducted on the mechanical properties of EBM parts have presented microstructure data as well. An EBM machine produces parts by sintering layer-by-layer a metallic powder with electrons of high energy. The process is conducted under high vacuum and in high temperature. This method of

manufacturing causes uneven void distribution within the part and unusual surface appearance. Thus, most of the explanations for mechanical properties of these parts were referred to the material's porosity and nature of its exterior surface.

Gaytan et al. studied the variations in microstructure along with the mechanical properties of Ti-6Al-4V cylindrical samples fabricated in an EBM machine. The observed ultimate tensile strength (UTS) was in the range of 1.15-1.20 GPa, the 0.2% offset yield stress (YS) ranged from 1.10 GPa to 1.15 GPa, and the percent elongation was in the range of 16% to 25%. The EBM's UTS and elongation values were comparable to those for wrought Ti-6Al-4V. Cylindrical samples of 6.8 cm length were fabricated and 1.0 cm sections from the top and from the bottom were examined for microstructure analysis. Samples were also compared with casted and wrought samples. Figure 19 shows optical images for the EBM samples. The figure shows that the samples have a homogeneous, continuous, fully dense structure and primarily acicular α-plate in a widmanstätten microstructure. The average α-plate thickness and length of the EBM samples in the top was larger than that in the bottom. Furthermore, in the bottom, the α-plates were finer and lamellar-like, more than acicular. Porous areas on the EBM build surface rarely appeared, which means almost all the particles were completely melted during processing. Figure 20 shows two wrought samples where each had different microstructure according to their preprocessing steps. Figure 20 (a) shows W1 wrought sample that had an acicular α-plate microstructure, while Figure 20 (b) was for the W2 wrought samples which had an equiaxed α/β mixture (Gaytan, et al., 2009).

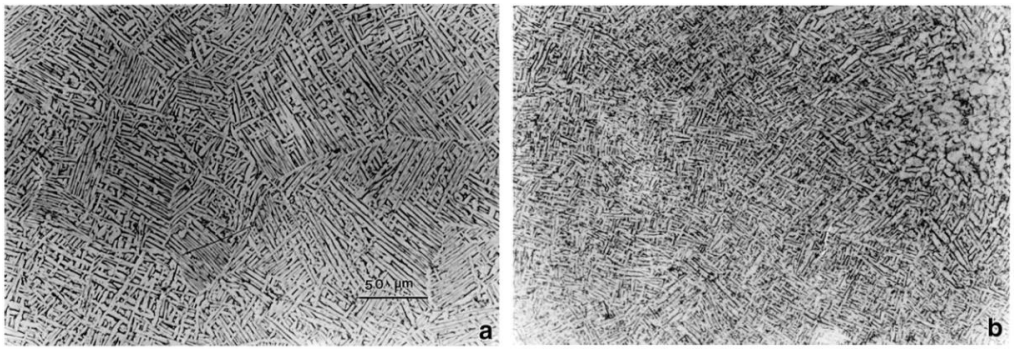

Figure 19: Optical metallographic images for EBM Ti-6Al-4V samples **(a)** 1 cm from top (b) 1 cm from bottom. Both images were taken at the same magnification (Gaytan, et al., 2009).

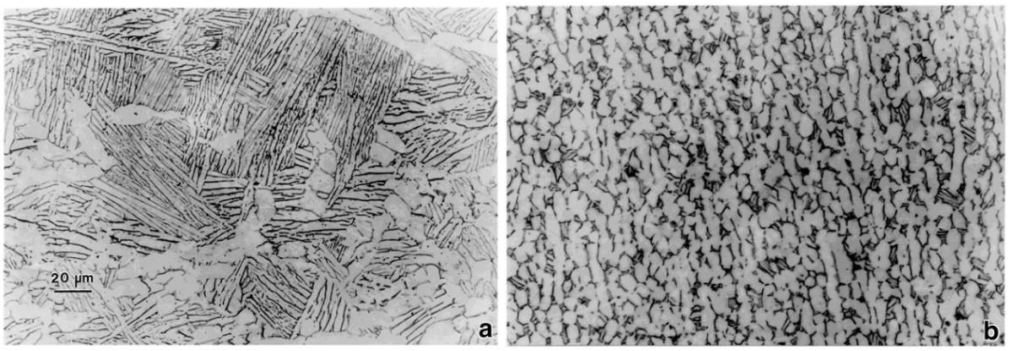

Figure 20: Optical metallographic images for wrought Ti-6Al-4V samples **(a)** W1 wrought alloy **(b)** W2 wrought alloy. Both images were taken at the same magnification (Gaytan, et al., 2009).

In addition, **Gaytan et al.** showed that variations in the mechanical property of EBM parts occurs within the part, which is difficult to achieve with conventionally-made alloy like wrought or cast Ti-6Al-4V. Hardness in particular is associated with microstructure variations from the top to the bottom of the part. With EBM technology, values of hardness below HRC 37 and above HRC 50 can be achieved within a few tens of layers (almost 2-3 mm). Moreover, a 30% reduction in powder size, from 30 µm to 20 µm, will increase elongation to the range of 23% to 90%, which is higher than that for forged Ti-6Al-4V. This variation in properties makes it possible to have parts of graded mechanical properties according to its application. For example, parts can be made of selective strength, fatigue resistance and elasticity to be biologically compatible with the bone properties (Gaytan, et al., 2009).

Murr et al measured mechanical properties, hardness and grindability of Ti-6Al-4V ELI (extra low interstitial, ASTM grade 23) produced with EBM, laser beam melting (LBM), traditional casting and wrought techniques (Murr, et al., 2011). As shown in Figure 21 (a), the EBM tensile strength, yield strength and elongation were the lowest of all four samples and they were closest to those for the cast alloy. This was due to the increase in oxygen content in the EBM alloy which increases the tendency for slip localization which decreases elongation. (Koike, et al., 2011). While LBM processing showed a slight increase in strength over EBM processing, and hardness of EBM was slightly higher than that of LBM as shown in Figure 21 (b). Hardness of both EBM and LBM were roughly 25% higher than cast and wrought alloys.

The percentage of interstitial oxygen present in the alloy affected hardness, since higher oxygen content causes higher microindentation hardness. As for the grindability, at a low wheel speed of 500 m/min, EBM had the highest value of all and cast alloy was the least, while at higher speed of 1,250 m/min no differences were observed in grindability (Figure 21 (c)) (Murr, et al., 2011).

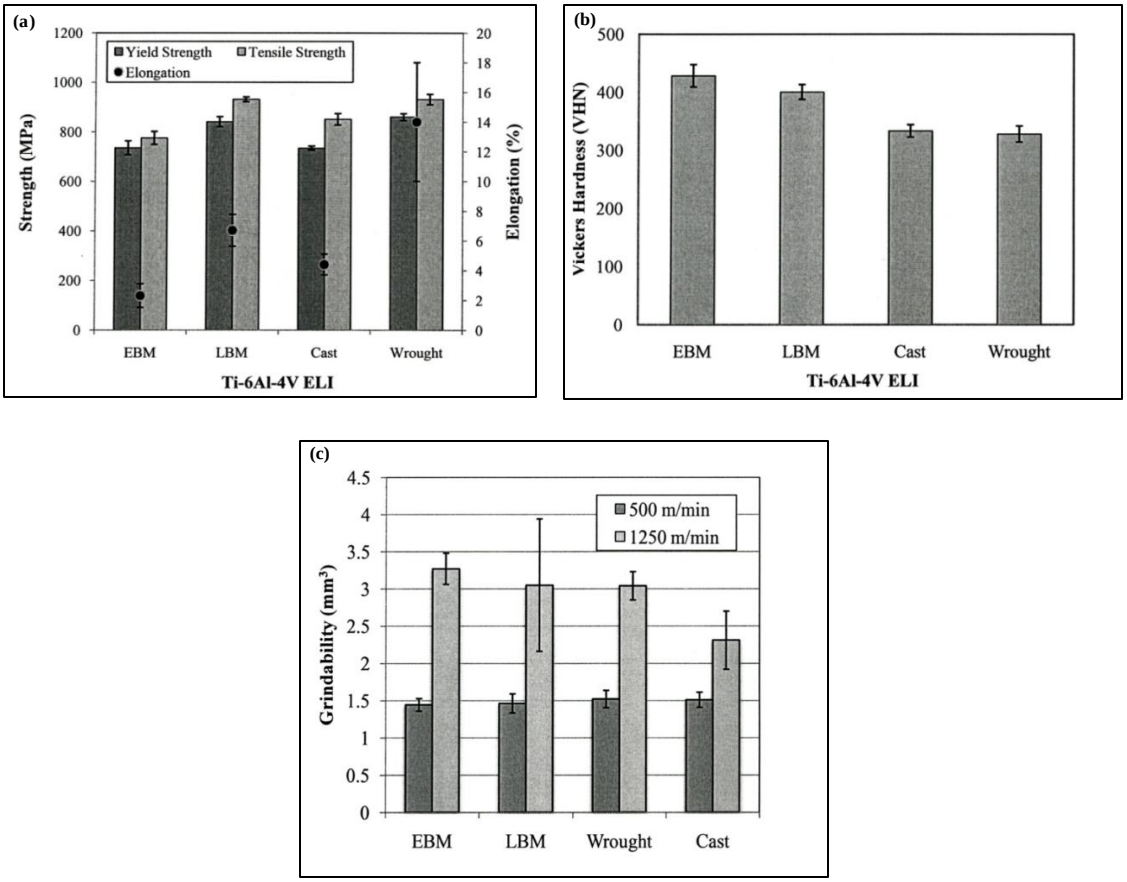

Figure 21: Tests conducted by Murr et al. on Ti-6Al-4V fabricated by different methods **(a)** Mechanical properties. **(b)** Vickers Hardness **(c)** Grindability (Murr, et al., 2011).

Koike et al. has also performed mechanical testing on as-built Ti-6Al-4V ELI dumbbell samples from EBM and casting machines and compared them with data for wrought specimens. Koike et al. mentioned the previous studies involving parts produced from the EBM machine specifically in dental applications. Table 6 is a comparison table by Koike et al. that details previously published mechanical

properties for EBM and selective laser melting (SLM) –or laser beam melting (LBM) - processes with the sample condition used in testing for each one. In agreement with Murr et al., the yield strength of EBM was comparable to that of the cast alloy but lower than the wrought alloy. Hardness of the EBM specimen was higher than that of the cast and wrought specimens. It was concluded that higher strength values were obtained for EBM treated samples –such as polished or machined ones- more than the as-built samples. Moreover, better hardness for EBM parts obtained due to the finer α/β lamellar structure and better grindability was because of lower ductility. Lower ductility and strength for EBM specimens were related to the oxygen content; in EBM recycled powder, oxygen content was near 0.34%, whereas it was 0.22% and 0.11% in cast and wrought samples, respectively. It was also discussed that due to the EBM fabrication process, repeated sintering of metal layer of 100-150 μm causes unique rough surface of rippled layers in comparison to the smooth surface obtained for a plastic dumbbell pattern or a cast specimen (Figure 22) (Koike, et al., 2011).

Table 6: Comparison of Ti-6Al-4V ELI or Ti-6Al-4V fabricated by EBM and SLM processes (Koike, et al., 2011).

	YS (MPa)	TS (MPa)	El (%)	*E* (GPa)	Remarks
EBM					
Lindhe and Harrysson (2003) Ti–6Al–4V	880	930	>10	128	Used HIP-specimen (likely machined)
Schroeder (2006) Ti–6Al–4V	910–960	950–1030	12–16	120	Used machined/polished specimens
Thundal (2008) Ti–6Al–4V	950	1020	14	114	
Christensen (2007) Ti–6Al–4V ELI	820	913	17	–	
Christensen et al. (2007b, 2008) Ti–6Al–4V ELI	800	876	16	–	Used HIP and machined specimens
	856	924	15	–	Used machined specimens
Chahine et al. (2008) Ti–6Al–4V ELI	–	1028	14	–	Used machined and polished tensile specimens
		928	3		Used as-fabricated specimens
Murr et al. (2009b) Ti–6Al–4V	1130	1180	>20	–	Used machined but unpolished specimens
Al-Bermani et al. (2010) Ti–6Al–4V	884–939	994–1031	12–14	–	
	841–875	939–978	13–14	–	
Koike and Okabe (2010) Ti–6Al–4V ELI	735	775	2.3	93	Used as-fabricated specimens
SLM					
Das et al. (1998) Ti–6Al–4V SLS/HIP	–	1117	5	–	Used machined/polished specimens
Lü et al. (2001) Ti–6Al–4V SLS/HIP Same as Santos	885	962	23	110	Used machined/polished specimens
Levy et al. (2003) Ti–6Al–4V SLS/HIP	–	1200–1400	1–2	–	Used machined/polished specimens
Murr et al. (2009b)	1350	1450	0.5	128	Used machined specimens

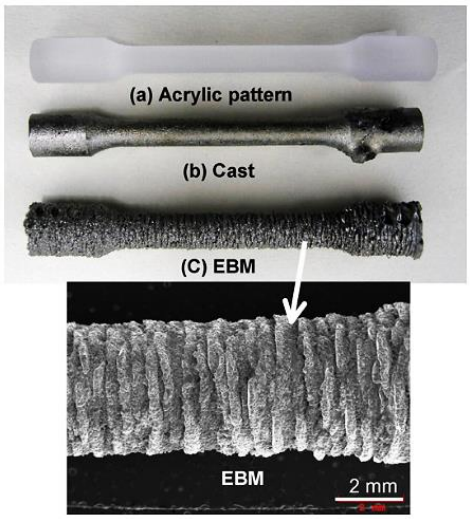

Figure 22: Surface appearance of (a) Plastic dumbbell pattern (b) Cast Ti-6Al-4V ELI (c) EBM-manufactured Ti-6Al-4V specimen with enlarged view (Koike, et al., 2011).

Mechanical properties of as-built EBM cylindrical samples in different orientations were examined by **Rafi et al.** (Rafi., et al., 2012). Tensile tests and fatigue tests were conducted on as-built Ti-6Al-4V parts built in vertical and horizontal orientations to observe the effect of surface finish on the mechanical properties. Table 7 shows that horizontally built samples had higher yield strength and tensile strength than vertically built samples. This was due to the change in microstructure that occurred; horizontal built samples showed more refined lamellar α structure in comparison to the vertical ones which resulted in higher strength values. In addition, horizontally built samples had higher fatigue strength than the vertically built samples. This was attributed to layer stacking during the fabrication process of both orientations. For vertically built samples, layers were stacked in thin disc-shaped layers, while for the horizontally built samples, layers were stacked in thin rectangular sheets. Stacking of these thin layers forms valleys and mountains on the surface, which causes a rough surface. SEM observations showed that these ridges on the vertically built samples appear on the exterior surface of the sample while for the horizontally built samples, they were on the upper surface as shown in Figure 23. These slips between each layer support crack initiation and propagation in vertically built samples more than in the horizontally built ones (Rafi., et al., 2012).

Table 7: Tensile test results for the EBM Ti-6Al-4V samples built in horizontal and vertical orientation (Rafi., et al., 2012).

		Stress at Yield [Offset 0.2 %] (MPa)	Ultimate tensile stress (MPa)	Strain at break (%)	E-Modulus (GPa)
As-built vertical		782 (SD:5.1)	842 (SD: 13.84)	9.9 (SD: 1.02)	101 (SD:2.5)
As-built horizontal		844 (SD:21.6)	917 (SD:30.53)	8.8 (SD:1.42)	104 (SD: 2.3)
% increase		8	9		
Machined vertical		869 (SD:7.2)	928 (SD:9.8)	9.9 (SD:1.7)	115 (SD:0.7)
Machined horizontal		899 (SD: 4.7)	978 (SD: 3.2)	9.5 (SD:1.2)	113.5 (SD: 2.5)
% increase		4	5		
ASM Handbook(1993) (Cast and annealed)		885	930		
% increase in machined compared to as-built	Vertical Orientation	11	10		
	Horizontal Orientation	6.5	6.6		

SD: Standard Deviation

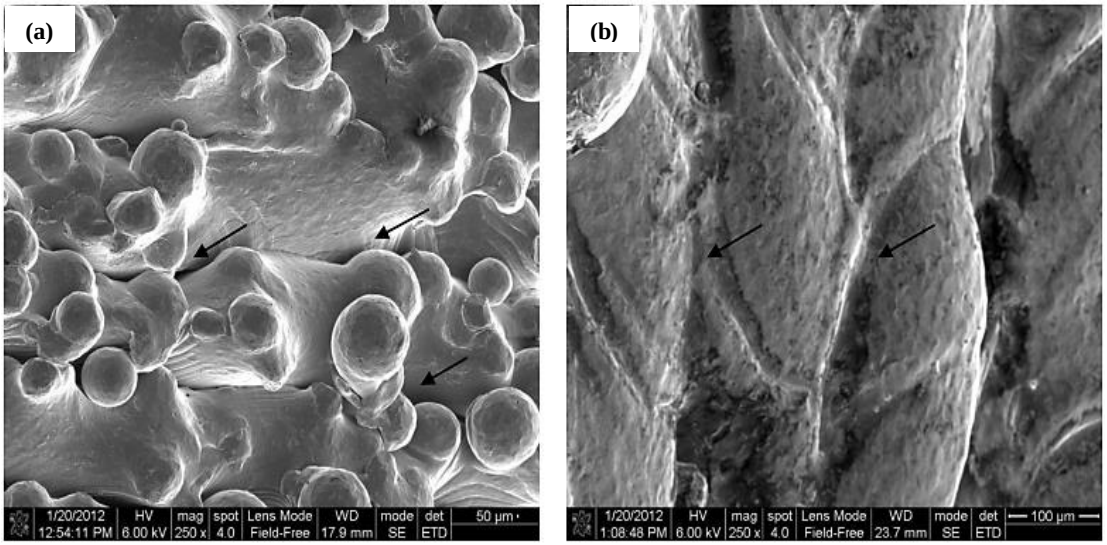

Figure 23: SEM images for the exterior surface of the EBM Ti-6Al-4V samples built in **(a)** Vertical orientation. **(b)** Horizontal orientation (Rafi., et al., 2012).

3.2.3 Porosity and Surface Roughness of Ti-6Al-4V Alloy

The manufacturing process in the EBM machine is conducted under high temperature and in a vacuum atmosphere. High speed electrons scan the metallic powder in a layer-based technique to build up the 3D object. These conditions of fabrication causes formation of voids at different locations on the part and causes irregularities on the exterior surface. Thus, porosity and surface appearance are major problems facing EBM manufacturing since these faults decrease the quality and performance of produced parts.

Newell studied the porosity of a part produced from S12 and A2 EBM Arcam machines. Pores were detected at different depths within the part with a variety of shapes and sizes ranging from as low as 10 μm to 250 μm in its depth dimension. With SEM observations, these pores were formed due to one or more of the following: incomplete melting, insufficient particle packing prior to electron beam processing, powder feedstock agglomeration and gas pores. Figure 24 (a) shows partially sintered powder particles that kept their initial spherical shape and did not melt into the rest of the bulk metal. Newell suggested that incomplete melting of the particles might be due to variations in the electron beam energy along with the beam velocity, this occurs when the beam energy is low with a relatively high beam speed. Another reason for the presence of pores is deficiency of powder in the layer before melting as shown in Figure 24 (b). This might be due to inefficient packing or insufficient supply. Moreover, non-uniform packing and/or unevenly distributed particles can lead to agglomeration of powder particles before the melting process as shown in Figure 24 (c). In addition, voids formed within the part can trap gas during the manufacturing process and lead to gas pores that appear when rapid solidification occurs as shown in Figure 24 (d). Thus, any part produced with either EBM machines cannot be guaranteed to be totally free of defects or pores. Newell mentioned that an optimized set of operating parameters can help in reducing this phenomenon but will not solve it completely (Newell, 2009).

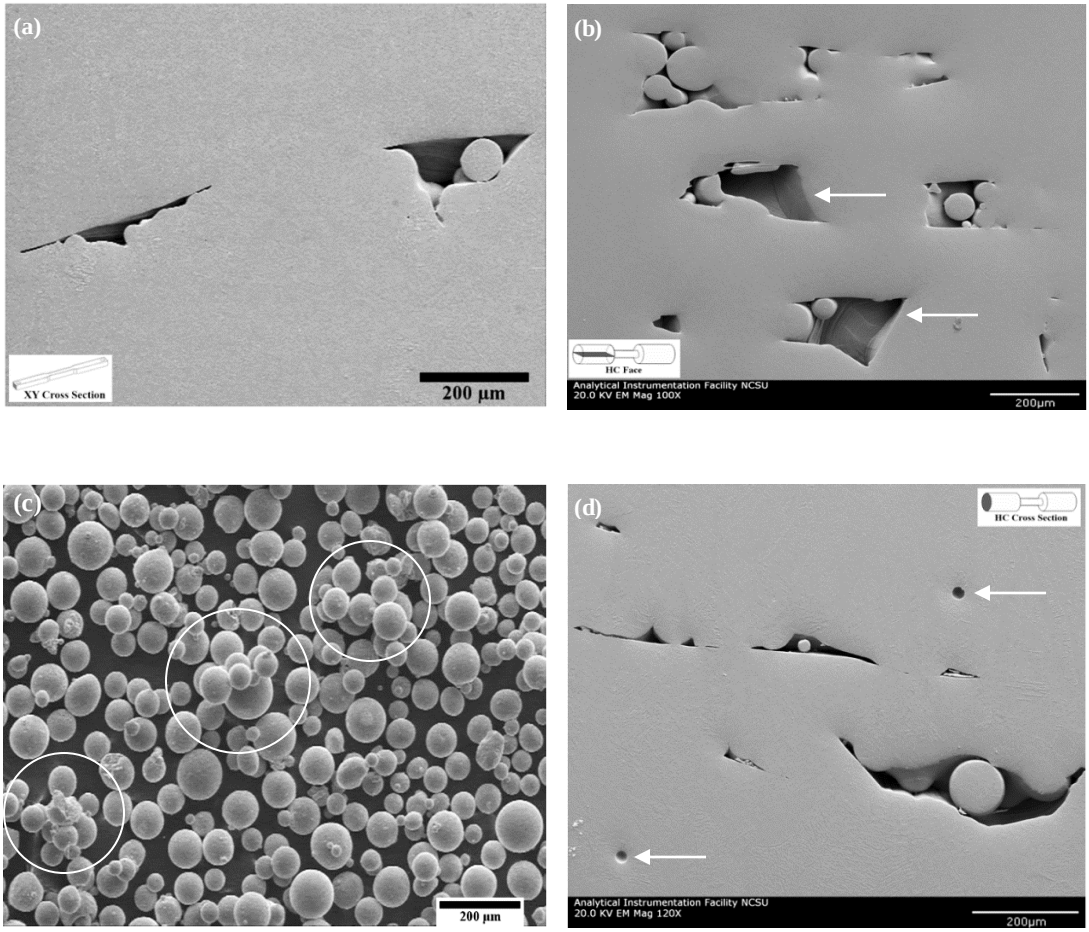

Figure 24: SEM images for **(a)** Cross section of tensile bar of XY growth direction of manufacturing illustrating incomplete melting of powder particle **(b)** Face of horizontal cylinder (HC) sample illustrating inefficient packing or supply of powder particles **(c)** Ti-6Al-4V powder with agglomerated particles **(d)** Cross section of horizontal cylinder (HC) sample with gas pores (Newell, 2009).

Moreover, as Ti-6Al-4V is inert to body environment and has a light weight property, this alloy was used to fabricate body implants of porous structure in the EBM machine. **Starly et al.** fabricated porous objects in EBM machine with Ti-6Al-4V alloy. Porous objects were produced with different pore and strut sizes, then objects tested for their mechanical properties. Porous structure proved to be a favorable configuration as it caused a reduction in the implant's modulus of elasticity and approached the elasticity of the replaced bone. Porous structure implant is also of a lighter weight and less effective stiffness than regular titanium implants, which reduces stresses transferred to the adjacent bone. SEM observations of this

structure produced from an EBM showed complete melting of the metal without any interlayer bonding differences indicating high functionality of these parts. Hence, this technique accomplished the need to have a highly porous implant of similar mechanical properties using the least amount of metal and without losing its biomedical strength. Figure 25 shows some Ti-6Al-4V porous models fabricated in an EBM machine (Starly, et al., 2009).

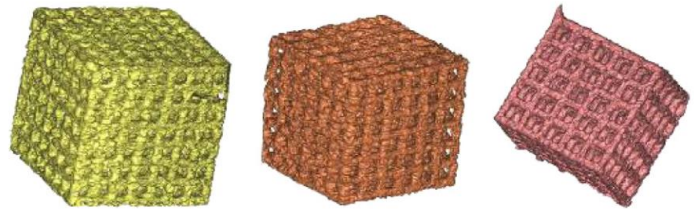

Figure 25: 3D digital model for three different sets of porous structure fabricated by the EBM machine (Starly, et al., 2009).

As previously mentioned, porosity and surface roughness can be controlled by employing the right set of process parameters. **Safdar** investigated the effect of the process parameter settings and geometry of the produced part (slab thickness) on the surface roughness and microstructure of Ti-6Al-4V produced with an EBM system. Four sets of rectangular slabs of different thicknesses were built; each set built with different process parameters of beam current, scan speed and offset focus (offset focus is the probe size on powder). Surface roughness was quantified by the arithmetic mean of absolute values of deviation points from the mean line. Samples had different roughness in the range of 1-20 µm. Surface roughness increased with increasing slab thickness and beam current, whereas it decreased with increasing scan speed and offset focus. These results were related to energy density of the melt pool. With an increase in energy density, many layers of powder on the building plate tend to sinter which causes overflow of the melt pool. This overflow will appear as valleys and mountains causing an increase in surface roughness (Safdar, 2010).

In the same study, **Safdar** investigated the effect of process parameters and slab thickness on the microstructure of EBM Ti-6Al-4V. The microstructure analysis obtained was in agreement with Gaytan et al. Safdar showed that Ti-6Al-4V built with EBM machine has a columnar grains of prior β phase growing along the build direction. The diameter of these grains was in the range between 20-200 μm. Inside these prior β grains there were widmanstätten α platelets of different sizes and orientations with rod-like β phase on the boundaries of α grains. The thickness of these α platelets ranges from 2 to 3 μm, while their width is from 5 to 10 μm. The parameters investigated were beam current, scan speed, offset focus, slab thickness and scan length. The effect of the first three parameters were related to energy density; energy density increases with increasing beam current and with decreasing scan speed and offset focus. It was concluded that with increasing energy density, the number and diameter (bunch size) of columnar grains of β phase increases and these grains will follow the build direction. While with lower energy density, these grains become tilted in direction of scanning. In addition, the α layer has a smoother grain boundary with increasing energy density and this layer becomes wavy with lower energy density. On the other hand, increasing the scan length and the thickness of the slab resulted in an increase in the diameter of columnar grain β. Also, the α platelets become coarser. Figure 26 shows optical micrographs for slabs built at high and low energy with the black arrows indicating the build direction. Black dots in Figure 26 (a) show α grains in the columnar grain of prior β phase, and the voids shown in Figure 26 (b) are due to the presence of argon gas in gas automatized alloy powder (Safdar, 2010).

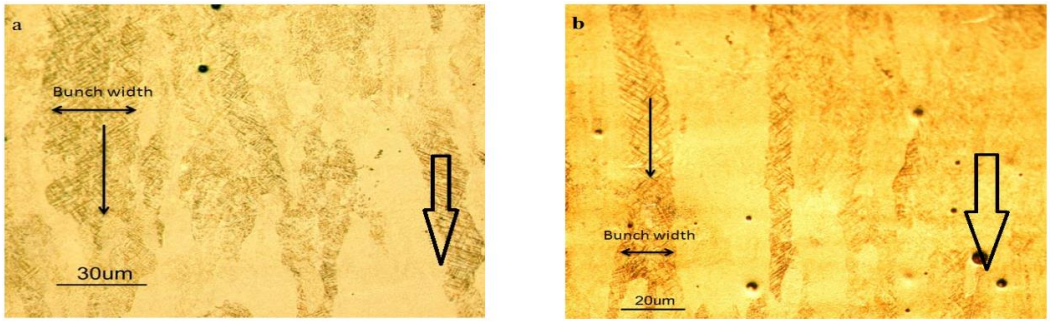

Figure 26: Optical micrographs for EBM samples built with scan speed of 250 m/s, offset focus 10 mA, slab thickness of 2.1 mm and beam current of **(a)** 6 mA (high energy density) **(b)** 4 mA (low energy density). Big arrows in both pictures show the build direction (Safdar, 2010).

3.2.4 Corrosion Resistance and Critical Pitting Temperature of Ti-6Al-4V Alloy

In general, not much effort has been put into studying the corrosion behavior of Ti-6Al-4V produced in an EBM system until now. This is possibly because EBM is a new advancement, and it is necessary to know the structure and properties of materials manufactured from this system first. In addition, most of its applications are in the medical and aerospace sectors where compatibility and strength are the key factors, and especially for a material that already has a strong corrosion resistance like titanium. However, with the expansion in the applications of this technology and the reduction in its cost, it has become more accessible to the world in distinct areas which made studying its corrosion in different conditions is an important issue.

Corrosion behavior of Ti-6Al-4V produced in an EBM machine was studied by **Murr et al.** and compared with cast, wrought and LBM (Laser Beam Melting) specimens. The environment at which the test was conducted included a deaerated solution of synthetic saliva at 37ºC. The LBM and wrought samples showed better corrosion resistance than the EBM and cast samples. Rapid cooling during the LBM process formed a controlled fine structure of ά martensitic, which gave the sample better corrosion resistance than large α platelets in the EBM's acicular α microstructure (Murr, et al., 2011). In wrought specimens, equiaxed structure gave better resistance than the EBM and cast (Martin, et al., 2010). Table 8 shows a comparison of corrosion characteristics such as the open circuit potential (OCP), polarization resistance (R_p), corrosion current density (i_{corr}) and passivation current density ($i_{passive}$). A potentiodynamic test was conducted in a deaerated solution of synthetic saliva at 37ºC and anodic polarization curves are shown in Figure 27 (Murr, et al., 2011).

Table 8: Corrosion characteristics of Ti-6Al-4V alloy in deaerated solution of synthetic saliva at 37ºC fabricated with different techniques (Murr, et al., 2011).

	OCP (mV)		Rp (MW)		icorr (nA/cm^2)		ipassive (nA/cm^2)	
LBM	−239	(18) [a]	1.81	(0.5) [a]	23	(8) [a]	870	(179) [a]
EBM	−246	(81) [a]	0.44	(0.3) [b]	199	(90) [b]	1645	(583) [a]
Cast	−243	(18) [a]	0.75	(0.7) [b,c]	199	(158) [b]	1137	(752) [a]
Wrought	−159	(18) [a]	1.36	(0.5) [a,c]	49	(25) [a]	837	(249) [a]

Values are means (one standard deviation) for properties of tested alloys. Identical letters indicate no statistical differences ($p > 0.05$).

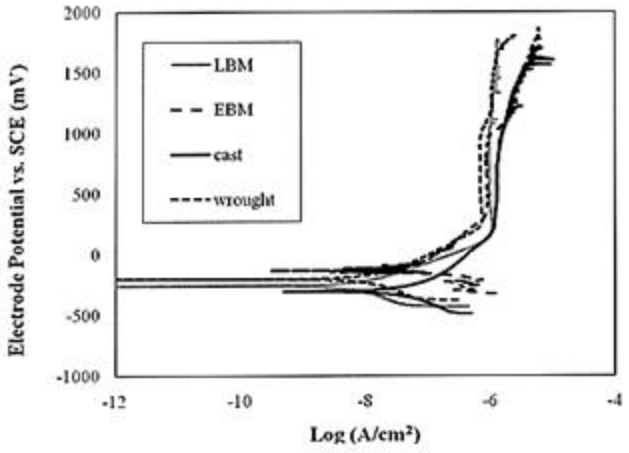

Figure 27: Anodic polarization behavior of Ti-6Al-4V in deaerated solution of synthetic saliva at 37ºC manufactured with different techniques (Murr, et al., 2011).

Corrosion resistance of titanium and its alloys of different microstructures and in different media was discussed in detail in Section 1.5. It was noted that the equiaxed structure has the best corrosion resistance and that ά martensite structure exhibits more corrosion resistance than α lamellar structure. No β phase or lower β phase allows for better passivity of this metal which enhances resistance (Martin, et al., 2010). Also, sodium chloride solution was the most aggressive environment for titanium alloys in comparison to other environments like sodium hydroxide (NaOH), acetic acid (CH_3COOH), phosphoric acid (H_3PO_4) and sodium carbonate (Na_2CO_3) (Abdulmageed & Ibrahim, 2010). The high corrosion

resistance of titanium and its alloys is due to the formation of a highly adhesive oxide layer on their surfaces. This passivation region clearly appeared in the polarization curves when a potentiodynamic scan was performed on titanium alloys in NaCl and HCl solutions, as was shown in Figure 15.

Critical pitting temperature (CPT) is a measure of the material's resistance to pitting corrosion. It is the lowest temperature at which the sample surface will be attacked under specific test conditions. CPT for high steel alloy is independent of pH in the range of 1-7, and independent of chloride concentration in the range of 1-5 M (Qvarfort, 1989). CPT can be determined with a potentiostatic test at constant potential or with multiple potentiodynamic tests at different temperatures. For 2205 duplex stainless steel (DSS2205) with composition of 21.6 % Cr, 5.3% Ni, 3.1% Mo, a potentiostatic test was conducted at 600 mV vs. SCE in 0.1 NaCl solution and the CPT was 60ºC. While for 20Cr-28Ni super austenitic stainless steel, it was 55ºC under the same testing conditions (Ebrahimi, et al., 2012).

Neville and Xu investigated the instability of several titanium alloys in acidic environments. Titanium alloys tested were: CP-Ti (commercially pure titanium, α-phase alloy of ASTM grade 2), Ti-5111 (near-α alloy of ASTM grade 32), Ti-6Al-4V ELI (α/β alloy of ASTM grade 23) and Ti-6Al-4V ELI/Ru (variation of grade 23 alloy with 0.1% Ruthenium). ELI indicates extra low interstitial alloy that has low oxygen content to resist stress corrosion cracking. The investigators performed a potentiostatic test on these alloys at 500 mV vs. (Ag/AgCl) and obtained CPT values listed in Table 9. CP-Ti had the least CPT in HCl solution of pH 4, while Ti-5111 had the least CPT value when NaCl was added to the HCl solution. Both Ti-6Al-4V had better corrosion resistance than CP-Ti and Ti-5111 in HCl solution of pH 4, while this resistance decreased when the solution had a lower pH value of 2. Potentiostatic tests for Ti-6Al-4V ELI in different environments are shown in Figure 28. It was noticed that under the conditions of this test, which is a constant potential of 500 mV vs. Ag/AgCl reference electrode, Ti-6Al-4V had a high CPT of 98ºC in a solution of pH 4. The presence of chloride ions in a solution of the same pH resulted in a very close value of CPT for both Ti-6Al-4V alloys. However, this CPT decreased when increasing the acidity of the solution to pH 2 (Neville, Anne; Xu, Jie, 2011).

Table 9: Critical pitting temperature of several titanium alloys measured with potentiostatic tests at 500 mV vs. a Ag/AgCl reference electrode (Neville, Anne; Xu, Jie, 2011).

Solution	Ti-6Al-4V ELI	Ti-6Al-4V ELI/Ru	Ti 5111	CP-Ti
HCl (pH = 4)	98.2	94.1	94.7	83.1
HCl (pH = 4) +500 ppm NaCl	99.8	94.1	86.1	87.0
HCl (pH = 2)	88.2	88.6	95.1	93.4

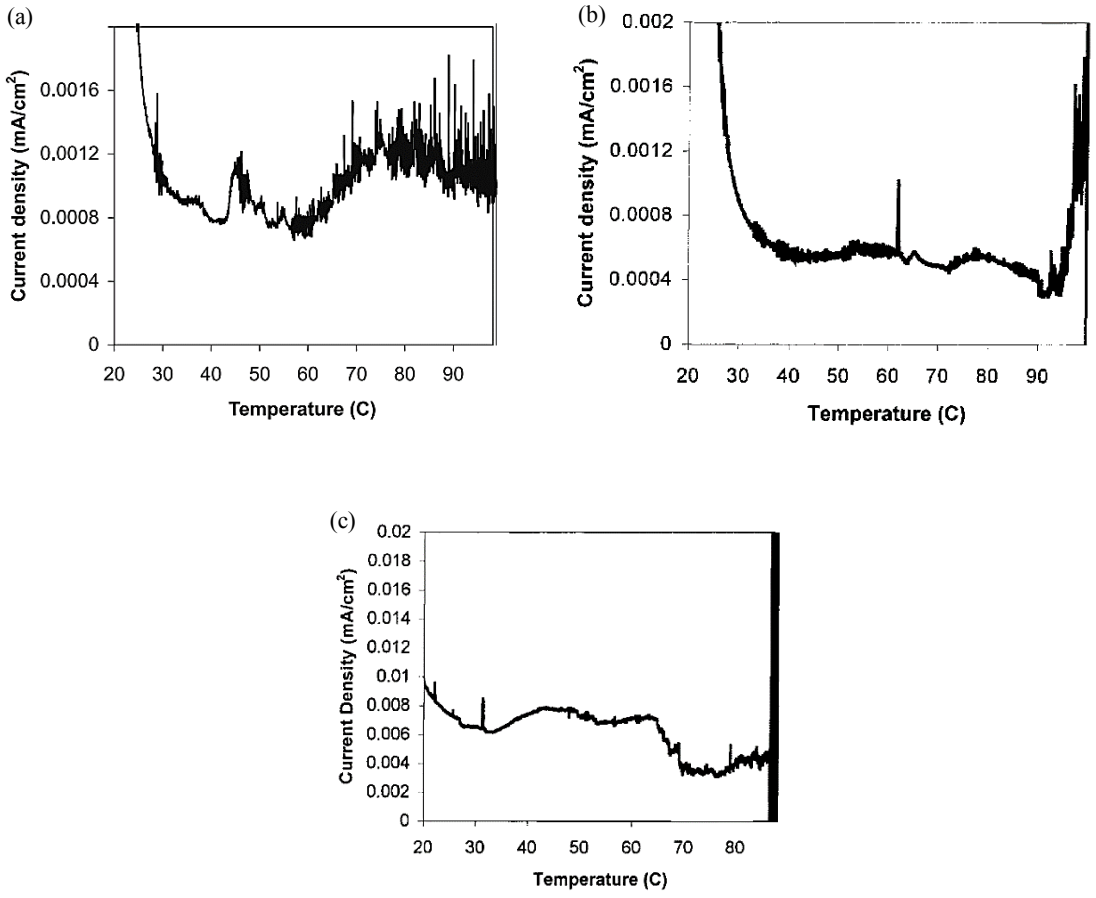

Figure 28 : Potentiostatic tests conducted at a potential of 500 mV vs. Ag/AgCl reference elecrode for Ti-6Al-4V ELI in different solutions **(a)** HCl at pH=4. **(b)** HCl at pH=4 with 500 ppm NaCl **(c)** HCl at pH=2. (Neville, Anne; Xu, Jie, 2011).

Since the corrosion resistance of the material is greatly affected by the texture of the surface, the CPT will be affected by the surface roughness as well. The effect of surface roughness on CPT was examined by **Moayed et al.** These investigators measured the CPT of rod samples of 904L stainless steel with potentiodynamic and potentiostatic tests in 1 M NaCl solution. Stainless steel samples were tested under different surface finishes to detect the effect of surface roughness on CPT. Potentiostatic tests were conducted in 1 M NaCl solution with anodic potential of 750 mV vs. Ag/AgCl reference electrode. The samples of surface finish of 60, 320, 1200 and 3 μm grit had an average CPT values of: 46.7, 49.0, 51.1, and 55.7ºC, correspondingly. Potentiostatic tests are shown in Figure 29. It was observed that the higher the roughness of the surface, the lower the CPT. This result was due to the fact that a rough surface provides holes of stagnant sites that induce a concentrated chemistry that initiates pits. It was noticed that small pits of diameter less than 30 μm were initiated at temperatures below CPT but they were not stable enough to cause a pitting. These pits were metastable pitting as they were assumed to repassivate during the test. Large pits of diameter more than 100 μm initiated at temperatures above CPT and did not repassivate, resulting in a stable pitting (Moayed, et al., 2003).

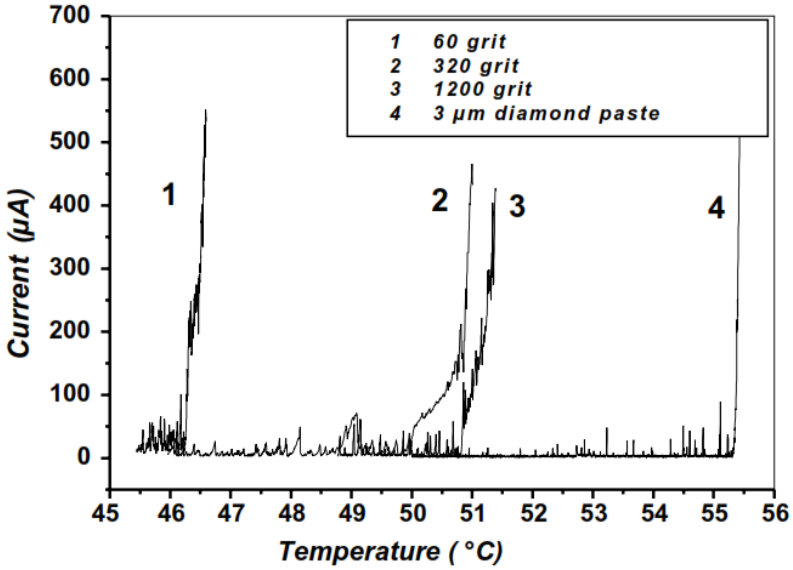

Figure 29: Potentiostatic tests conducted at 750 mV vs. Ag/AgCl reference electrode, for 904L stainless steel of different surface finish (Moayed, et al., 2003).

CHAPTER IV

RESEARCH METHODOLOGY

The present research evaluates Ti-6Al-4V manufactured with an EBM machine in two parts. First, corrosion resistance of Ti-6Al-4V samples fabricated in an EBM machine was evaluated through performing potentiodynamic and potentiostatic tests. Pitting potential (E_{pit}) and critical pitting temperature (CPT) were identified from these tests as they define the maximum temperature and potential the alloy can tolerate at certain temperatures and in specific surroundings without pitting. E_{pit} was found at different temperatures and CPT was inspected at different pH values of NaCl solution. Moreover, EBM corrosion resistance was compared to conventionally-made wrought Ti-6Al-4V. In the second part of the research, samples of Ti-6Al-4V from EBM were manufactured with different processing parameters of the machine. Surface roughness, CPT, density and porosity of these samples were measured, and results obtained for these properties were related to EBM processing parameters.

4.1 Part One: Electrochemical Testing of Ti-6Al-4V Parts Manufactured in Electron Beam Melting Machine and Comparison with Wrought Ti-6Al-4V Alloy

4.1.1 Potentiodynamic Testing

The following examinations were done with potentiodynamic tests:

- Comparison of the polarization curve of Ti-6Al-4V alloy manufactured by EBM machine and by conventional wrought method at room temperature in NaCl solution.
- Pitting potential determination for Ti-6Al-4V parts manufactured by EBM machine and by conventional wrought method in NaCl solution at different temperatures.

The objective in this part of the study is to establish an overview of the corrosion behavior of EBM and wrought titanium alloy in 3.5% mass NaCl solution. A potentiodynamic test produces polarization

curves where corrosion potential, pitting potential and passivation region can be identified. Both EBM and wrought Ti-6Al-4V alloy were tested under different temperatures, and a relation of pitting potential vs. temperature for both alloys were established.

Another purpose for this part of the work is to identify the potential under which potentiostatic tests of part two need to be conducted. ASTM Standard G150-99 (2010) was implemented to measure CPT of Ti-6Al-4V using the potentiostatic test that runs at constant potential (ASTMG150-99, 2010). This standard is for stainless steels, and the potential recommended in the standard is 700 mV or 800 mV vs. SCE. In comparison to stainless steels, titanium and its alloys have a higher pitting potential. To further validate this issue, a potentiostatic test at 800 mV vs. SCE was performed. The experiment ran until the temperature reached 100°C, and the solution started to boil. The curve obtained is shown in Figure 30. Inspection of the tested surface showed no pits and no visible change in color, and the current did not exceed 30 $\mu A/cm^2$. Since the current was retained in a low value without any major increase and no change in surface appeared, it is concluded that no pitting corrosion occurred. Hence, for titanium alloys, 800 mV vs. SCE is a low potential and another value should be determined. The correct potential value applied in a potentiostatic test to measure the CPT of titanium alloy can be obtained from the potential vs. temperature curve (Arnvig & Bisgard, 1996). The details of the potential value chosen will be discussed in section 4.2.2 of this chapter.

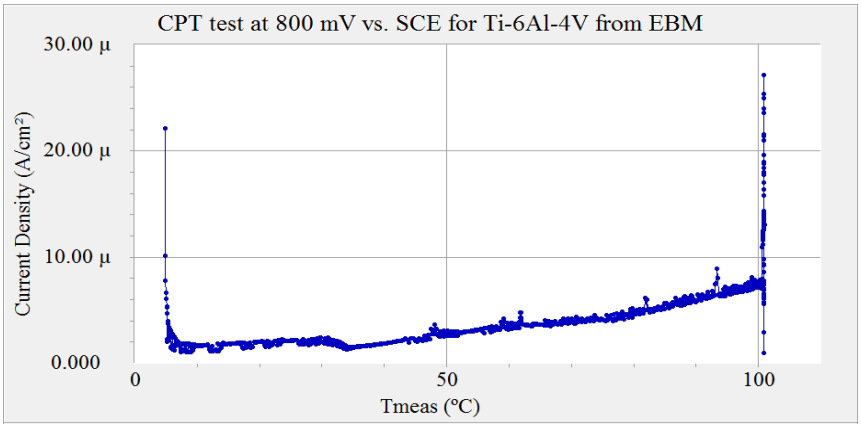

Figure 30: Potentiostatic test of Ti-6Al-4V produced from EBM machine in 3.5% mass NaCl solution. Test conducted at potential of 800 mV vs. SCE.

Potentiodynamic scan: Apparatus and procedure

In any corrosion cell, anodic reaction takes place on the surface of working electrode where metal oxidation occurs according to reaction (1) mentioned in chapter I. While the cathodic reaction represented by reaction (3) takes place on the counter electrode where reduction of hydrogen occurs and hydrogen bubbles are observed on the surface of the counter electrode. The counter electrode chosen must be inert to the electrolyte solution even in the most acidic environment to maintain the oxidation reaction on the surface of working electrode. Finally, the reference electrode measures the potential of the working electrode through a movable luggin probe. Luggin probe is placed as close as possible to the sample to reduce ohmic resistance interferences.

Following the ASTM standard G5 (Reapproved 2004) (ASTMG5-94, 2004), a potentiodynamic scan was employed using a jacketed multiport electrochemical cell from Gamry Instruments along with a chiller to control the temperature. As shown in Figure 31 (a), the corrosion cell is jacketed to allow for a water circulating bath around the cell. The cell is connected to a potentiostat in order to apply potential at a constant rate. The top of the cell has several ports to permit the introduction of electrodes and a thermometer. In Figure 31 (b), a working electrode and counter electrode were immersed in the test solution, while the reference electrode was kept in a reference bridge tube outside the cell, and the reference bridge was filled with same test solution (NaCl solution). The working electrode consists of a copper wire that has the sample mounted to it. The counter electrode is a high density graphite rod that is inert to electrolyte solution. The reference electrode is filled with saturated calomel and located in a bridge tube outside the test solution to keep the electrode away from the test solution thermal gradients.

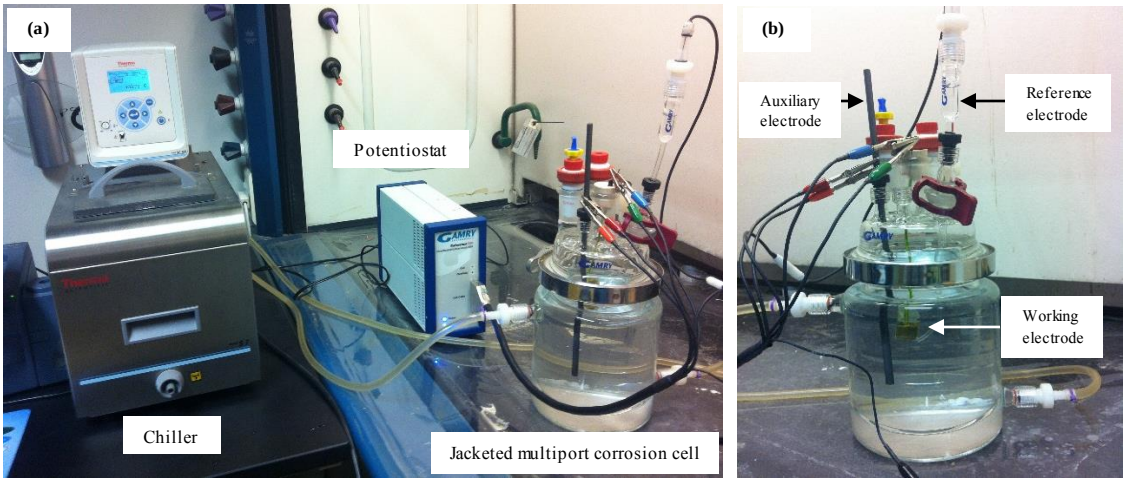

Figure 31: (a) Jacketed multiport electrochemical cell kit and the chiller for conducting potentiodynamic scan to determine pitting potential at different temperatures. **(b)** Jacketed multiport corrosion cell.

The Ti-6Al-4V samples from the EBM machine have the composition and mechanical properties shown in Table 10. They were cut into approximately 5 mm cubes and made into a working electrode by gluing the sample to a copper wire with a conductive adhesive. Both ends of the wire were stripped to allow direct contact between the wire and sample surface. Afterwards, the sample and the lower part of the wire were insulated with an epoxy resin from all sides, except one side of the sample surface, which was polished to 600-grit emery paper. The samples were then washed with ethanol and immersed in a test solution one hour prior to testing. Figure 32 (a) shows the working electrode with a sample mounted in the epoxy resin, and Figure 32 (b) shows the schematic drawing.

Table 10: Composition and mechanical properties of Ti-6Al-4V samples produced from EBM machine (Arcam, 2013).

Composition (weight %)							
Aluminum	Vanadium	Carbon, C	Iron, Fe	Oxygen, O	Nitrogen, N	Hydrogen, H	Titanium, Ti
6.00%	4.00%	0.03%	0.10%	0.15%	0.01%	0.003%	89.71%
Mechanical properties							
Yield Strength	Ultimate tensile strength		Elongagtion	Fatigue Strength		Rockwell Hardness	Modulus of elasticity
950 MPa	1020 MPa		14%	> 10,000000 cycles		33 HRC	120 GPa

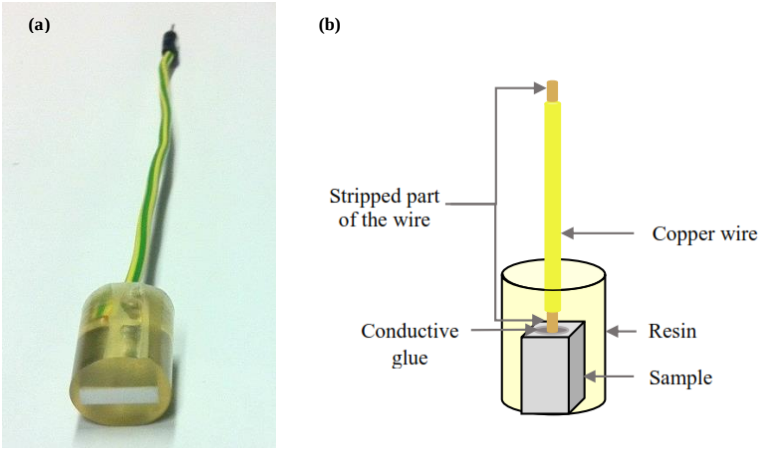

Figure 32: (a) Working electrode of mounted sample for potentiodynamic test. **(b)** Schematic draw of working electrode.

The Wrought Ti-6Al-4V samples were manufactured by the company Metals Samples. Wrought Ti-6Al-4V samples were fabricated by annealing process and these samples have the composition shown in Table 11. The samples are 50 mm square-shaped with a thickness of 5 mm. Preparing the wrought samples for a potentiodynamic test was done in the same way described for preparing the EBM samples, and the working electrode of the wrought alloy obtained is the same as shown in the schematic drawing of Figure 32 (b).

Table 11: Composition of Ti-6Al-4V produced from the company Metals Samples.

Composition (weight %)							
Aluminum	Vanadium	Carbon	Iron	Oxygen	Nitrogen	Hydrogen	Titanium
6.28%	4.05%	0.013%	0.20%	0.11%	0.008%	0.0048%	89.33%

A potentiodynamic scan was conducted at a constant scan rate of 0.5 mV/s. The current and potential were recorded during the experiment and polarization curves of potential versus logarithm of current density were obtained. The experiment was conducted until a major increase in current was detected which indicates onset of pitting. This experiment was done under different temperatures for both the EBM

and the wrought titanium alloy. The values of pitting potential were read from these curves, and data of the potential versus temperature was obtained.

4.1.2 Potentiostatic Testing

The following examinations were done with potentiostatic tests:

- Critical pitting temperature of Ti-6Al-4V manufactured by EBM machine and by conventional wrought method at 800 mV vs. SCE in NaCl solution.
- Critical pitting temperature of Ti-6Al-4V manufactured by EBM machine in NaCl solutions of different pH values.

Critical pitting temperature is an indication of a material's resistance to pitting corrosion in a given environment. It is the lowest temperature at which pits will occur in test conditions. As EBM objects have voids and surface variations, their ability to withstand localized attack might be affected. Samples from an EBM machine were manufactured and tested as-received in order to observe their corrosion properties. They were tested without additional surface treatment, since typically they are used without additional processing in most industrial applications. The test solution was 3.5% mass NaCl, and the potential applied was 800 mV vs. SCE, according to ASTM standard G150-99 (2010). For comparison purposes, a test was performed on Ti-6Al-4V manufactured in EBM machine and on a wrought alloy which was polished with 600-grit emery paper. Afterwards, the same test was done on EBM samples at several pH values in order to observe the effect of more aggressive conditions on CPT of this alloy.

Potentiostatic test: Apparatus and procedure

The apparatus shown in Figure 33 was used in assessing CPT. The apparatus consists of Gamry's Flexcell critical pitting test cell, intravenous set of deionized water, potentiostat, temperature controller, and mechanical mixer. The Flexcell critical pitting test cell consists of three electrodes, as shown in Figure 34. The counter electrode is a graphite rod inert to test solution. The reference electrode is mounted outside the

cell in an external reference well filled with test solution to avoid temperature fluctuations that happens inside the cell. Unlike the multiport jacketed cell, the working electrode is introduced in this cell from the bottom to allow for a deionized water path around the edges of exposed surface, which will help in preventing the occurrence of crevice corrosion. Deionized water was supplied to the cell through the intravenous set with a controlled flow rate of around 6 ml/hour. This system provides a flooded seal of deionized water around the sample edges without diluting the test solution.

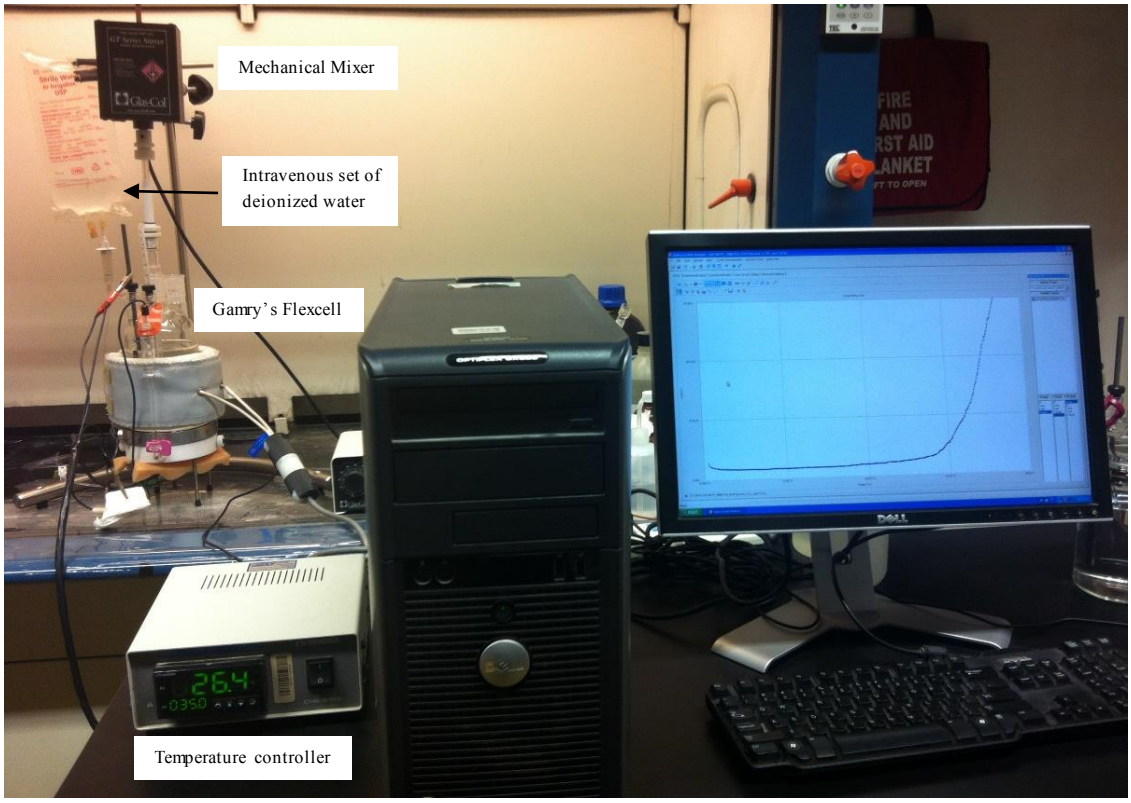

Figure 33: Apparatus used in measuring critical pitting temperature.

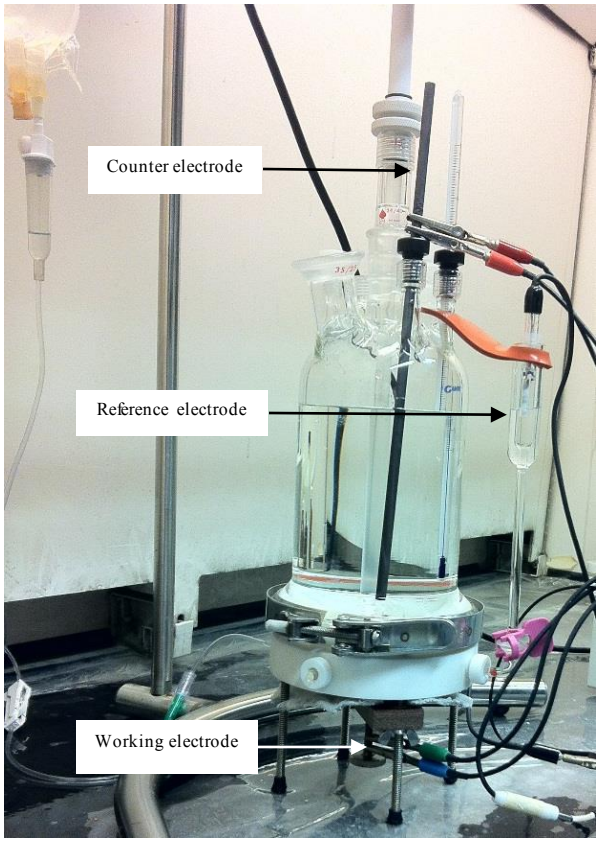

Figure 34: Flexcell critical pitting test cell from the firm Gamry Instruments.

Another important component of the apparatus is the potentiostat which applies potential and measures the current density of the sample during the experiment. In addition, the potentiostat provides digital outputs of set temperatures to the temperature controller to achieve a heating rate of 1°C/min. The temperature controller converts these set points to the current delivered to a heating jacket surrounding the cell. The controller operates in a cyclic mode to attain the required temperature increase ramp. The temperature controller measures the temperature inside the cell with an RTD temperature probe that is placed in the bottom of the cell close to the sample. Finally, to minimize temperature gradients within the cell, a mechanical mixer with a speed of 100 rpm is used inside the cell.

The ASTM standard G150-99 (2010) was employed while using a potentiostatic test to determine the CPT in 3.5% mass NaCl solution. Figures 35 (a) and (b) show Ti-6Al-4V samples used in testing. EBM

samples are of a disc shape with a diameter of 45 mm and 3.5 mm thickness. The wrought sample is 50 mm square-shaped, and has a thickness of 5 mm. The EBM and wrought alloy have the composition and mechanical properties shown in Tables 10 and 11, respectively. Samples were placed in the bottom of the cell where a seal of deionized water surrounded the edges of exposed area in order to obtain a crevice-free test. The exposed surface area of the sample was 5 cm^2. The sample was also covered with an insulating tile behind it in order to reduce heat loss to the surroundings.

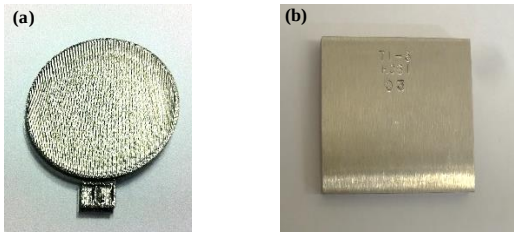

Figure 35: Ti-6Al-4V used in potentiostatic test **(a)** EBM manufactured. **(b)** Wrought manufactured**.**

The test solution was introduced to the cell at a temperature around 0°C. A constant potential of 800 mV vs. SCE was applied while the solution temperature was increased at a constant rate of 1°C/min. The deionized water was allowed to enter the cell with a flow rate of 6 ml/hour. The mixer speed was 100 rpm. The values of the current and the temperatures were recorded, and the temperature at which the current density (current/unit area) exceeded 100 $\mu A/cm^2$ for 60 seconds was recorded as the CPT (ASTMG150-99, 2010).

The CPT for EBM samples were also examined under a pH of 2 and 10. The original solution of 3.5% mass NaCl had a pH around 5.7. To make this solution more acidic, dilute HCl was added until the pH value of 2 was achieved. To make the solution more basic, dilute NaOH solution was added to achieve pH value of 10. The CPT test was then conducted on the EBM samples as mentioned previously.

4.2 Part Two: Statistical Design of Experiment for Process Parameters of Electron Beam Melting Machine

An electron beam melting machine can run under different process parameters to allow for variation in the properties of the part that is produced, such as surface roughness and porosity. Consequently, a specific set up of these parameters should be applied to obtain parts with the required specifications depending on their application. The EBM samples were manufactured under different process parameters. A statistical design of experiment was applied in order to determine the following examinations:

- Effect of EBM beam current, beam speed and offset focus on surface roughness
- Effect of EBM beam current, beam speed and offset focus on critical pitting temperature.
- Effect of EBM beam current, beam speed and offset focus on density and porosity.

4.2.1 Design of Experiment (DOE)

For a better understanding of the EBM build parameters' effect on characteristics of a part produced, a statistical design of experiment (DOE) was conducted. A DOE is one of the statistical tools used to reduce the variability of a process, as random variations can cause defective products. This technique identifies variations and eliminates them until a defect-free product is attained.

A DOE is a statistical procedure that establishes conditions for a series of experiments in order to identify the critical factors which affect the response –which is for this study the CPT, roughness, porosity and density. The DOE establishes a sets of EBM build parameters and varies them in order to identify specific effects on the properties of parts produced (Schmidt, Robert G. Launsby; Kiemele, Mark J., 1997). Arranging sets of factors can be performed in many design types, and since there is a relatively small number of factors to be examined in this research, a full factorial design is the preferable choice. This type of design sets all possible combinations of factors that might be of a significant effect to the response, with the aim to evaluate the effect of all parameters individually along with the interaction effects as well. Two levels of

each parameter are explored: high and low. With three factors, each of two levels, a full factorial design would have 2^3 possible arrangements of experimental conditions. This means that eight samples with different combinations of building parameters will be built. Table 12 was constructed using Minitab software. For the purposes of standardization, values were coded according to their levels such that the high values and low values of each factor are indicated as +1 and -1, respectively.

Table 12: Full factorial statistical design of experiments conducted on samples produced with EBM machine to study the effect of EBM building parameters on properties of the samples.

Sample number	No. of replicates	Coded values			Decoded values		
		Beam current	Beam speed	Offset focus	Beam current (mA)	Beam speed (mm/s)	Offset focus (mA)
1	3	-1	-1	-1	5	3000	0
2	3	1	-1	-1	10	3000	0
3	3	-1	1	-1	5	6000	0
4	3	1	1	-1	10	6000	0
5	3	-1	-1	1	5	3000	25
6	3	1	-1	1	10	3000	25
7	3	-1	1	1	5	6000	25
8	3	1	1	1	10	6000	25

After testing the above 24 samples for roughness, CPT, density and porosity, data were analyzed to build a mathematical model to relate EBM build parameters (factors) to the properties (response). In order to make a decision about which factor should be included in the model equation, an analysis of variance approach (ANOVA) was employed. ANOVA is one of the analysis strategies and it is based on estimates of variance. It estimates the effect of the -1 level response and the effect of the +1 level response for each factor and for the interaction factors as well. By choosing a 95% level of confidence, each factor or an interaction factor is significant to be included in the model equation or insignificant to be omitted from the equation. When the significance of a factor (or interaction factor) has a probability of significance greater than 95%,

then an EBM processing parameter will be included in the model. The details of the ANOVA statistical hypothesis tests are discussed in "Understanding Industrial Designed Experiments" for Schmidt (Schmidt, Robert G. Launsby; Kiemele, Mark J., 1997) .

With this analysis, mathematical models that relate significant EBM build parameters to the responses of surface roughness, CPT, density and porosity were obtained.

4.2.2 Experimental Implementations

A statistically designed experiment was used to produce samples from the EBM machine under different process parameters of beam current, beam speed and offset focus according to Table 12. Samples were of a disk shape with a 45 mm diameter and 3.5 mm thickness as shown in Figure 35 (a). Three replicates were tested to ensure consistency. First, the surface roughness was determined for the as-built samples, then a potentiostatic test was conducted to find the CPT. After that, the density of the samples was measured, and porosity was calculated from density values.

Measuring the surface roughness

Surface roughness is a measure of the texture of a surface. It is quantified by the vertical deviations of the measured surface from its ideal form, which is typically obtained from a reference surface. Roughness is characterized in the present study by the root mean squared (RMS) values of each point's deviation from the mean. A 3D optical profilometer was used to measure the surface roughness of the samples (Figure 36). It creates profiles of an 800 micron squared image and provides an overall average roughness of the profile. For this research, a stitched profiles of an 8x8 array was created in order to measure the surface roughness of a total surface area of 30.36 mm square. Roughness was measured at the center of the sample. The samples were measured as received.

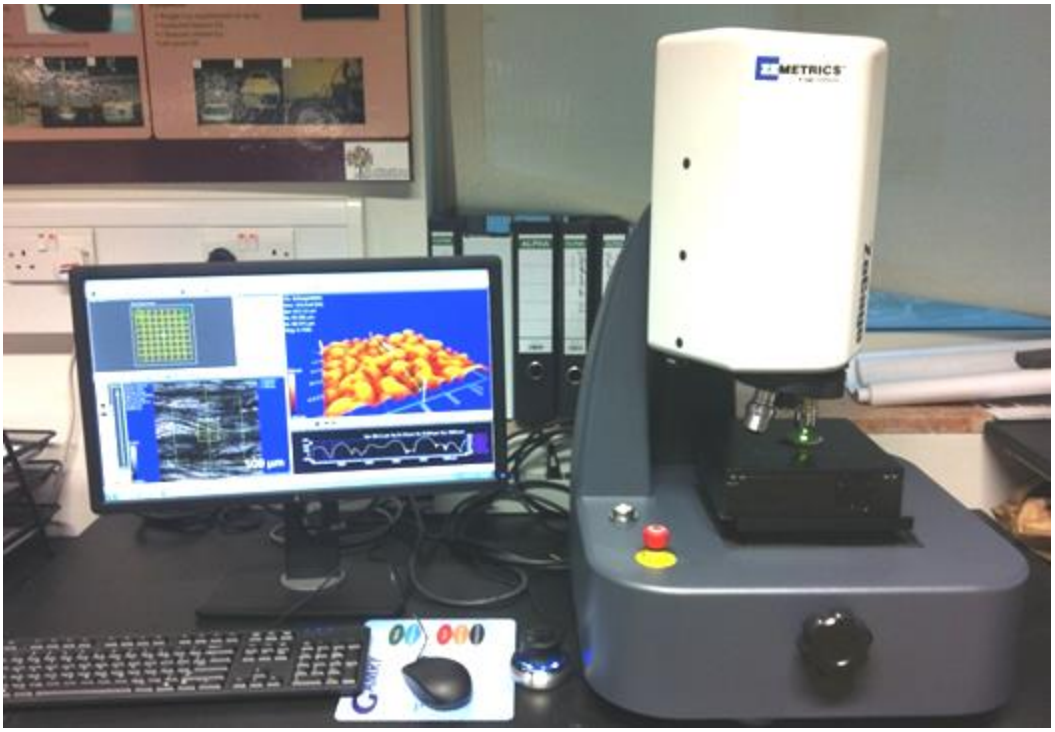

Figure 36: 3D optical profilometer.

The 3D optical profilometer is an interference microscope that utilizes a visible light to create combined images of the specimen and, a reference object. Figure 37 shows the microscope optical interference profiler where the light beam is split into two paths: one passes through the focal plane of the specimen and the other passes through a reference mirror. Reflected light waves from the two paths are then recombined. The reference mirror has near perfect flatness. Therefore, light waves from the specimen is compared to light reflected by the reference surface. Due to height variations in the specimen, differences in the wave lengths of both reflected lights will be obtained. These wavelengths cause constructive and destructive interferences in the combined beam, which are called fringes. These interference fringes are then focused in the interference beam into a digital camera. Images are seen as light and dark areas. The light areas are due to the formation of constructive interferences and the dark areas are due to the destructive interferences. The interference images are then converted to measured heights and surface roughness is calculated (Zygo, 2011).

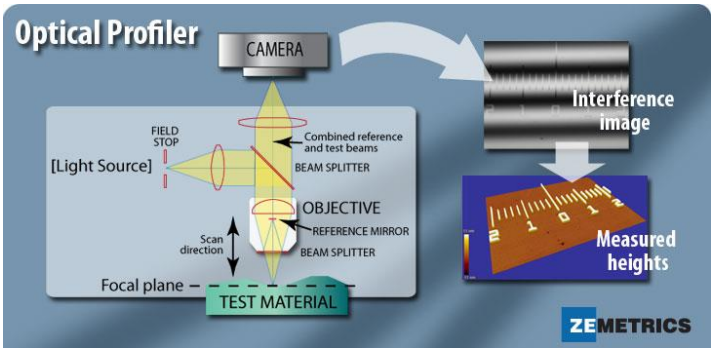

Figure 37: How 3D optical profilometer works (Zygo, 2011).

Measuring the CPT

A potentiostatic test was used for determining the critical pitting temperature of samples manufactured at different process parameters. The same apparatus mentioned in section 4.1.2 was used (Figure 34). Similar experimental procedure was followed in this part for performing potentiostatic test. However, the value of constant potential applied during potentiostatic test varied. As discussed in section 1.6.3, potentiodynamic tests at different temperatures were used to construct potential-temperature curve as in Figure 18, from which the right potential value was determined. The potential value should be above the pitting potential region but below the transpassive potential (Arnvig & Bisgard, 1996). The potential value used for this part was 2,400 mV vs. SCE.

Measuring the density

The densities of the samples were measured using a glass pycnometer along with an analytical balance shown in Figure 38. A pycnometer gives the density of a solid sample based on the water displacement principle. To ensure complete removal of air bubbles from inside the sample pores, a vacuum set was applied to remove trapped air as shown in the schematic drawing in Figure 39. Due to the pycnometer size limitation, disc-shaped samples were cut into three parts, and the densities of the three parts were measured. The

average density of each sample ($\bar{\rho}_{sample}$) was calculated as the ratio of the total mass to the total volume. Average density of one sample can be calculated according to equation 14:

$$\bar{\rho}_{sample} = \frac{m_1 + m_2 + m_3}{\left(\frac{m_1}{\rho_1} + \frac{m_2}{\rho_2} + \frac{m_3}{\rho_3}\right)} \qquad (14)$$

Where m_1, m_2 and m_3 are the mass of part 1, part 2 and part 3 of one sample, respectively. The same can be said for the densities ρ_1, ρ_2 and ρ_3 of the three parts of one sample.

Figure 38: Analytical balance and glass pycnometer used in measuring density of samples.

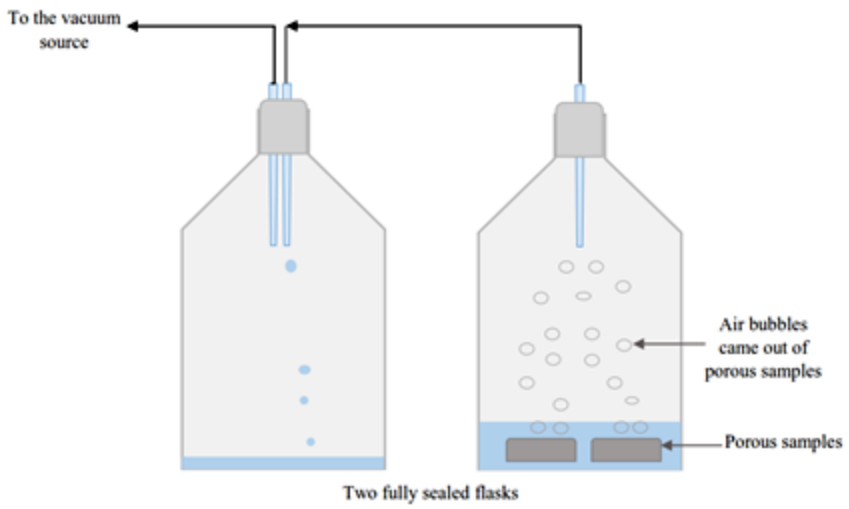

Figure 39: Schematic drawing of the vacuum set used to remove trapped air from the pores of EBM samples.

Calculating the porosity

Porosity represents the fraction of the bulk sample that is not occupied by solid matter. It is the ratio of pore volume to the total bulk volume. Porosity can be expressed as a percentage and calculated as in the following equation:

$$\emptyset = \left[1 - \left(\frac{\rho}{\rho_s}\right)\right] \times 100\% \qquad (15)$$

where Ø is the porosity present, ρ is the density of the sample measured and ρ_s is the density of bulk solid material. For the Ti-6Al-4V alloy, ρ_s is 4.43g/cm^3 (Donachie, 2000).

CHAPTER V

RESULTS AND DISCUSSIONS

This chapter begins the analysis of the first experimental research, which involved a comparison between polarization curves of Ti-6Al-4V samples manufactured in an EBM machine and conventionally wrought samples of the same alloy. An overview of the alloy's behavior was obtained from these curves, and pitting potential was determined. Pitting potential was found at different temperatures, and a potential-temperature relation was established for Ti-6Al-4V parts manufactured by the two techniques. Afterwards, critical pitting temperature (CPT) was determined with potentiostatic tests at a potential of 800 mV vs. SCE in 3.5% mass NaCl solution for EBM Ti-6Al-4V alloy and for wrought of the same alloy. CPT was also determined for EBM Ti-6Al-4V samples under different pH values of 3.5% mass NaCl solution.

In the second part of this chapter, the effect of EBM manufacturing parameters was correlated to surface roughness, CPT, density and porosity of the Ti-6Al-4V samples. The EBM samples were manufactured under different EBM process parameters of beam current, beam speed and offset focus. Surface roughness values were found for as-built samples using a 3D profilometer before setting for the CPT test. CPT values were obtained from potentiostatic tests conducted in 3.5% mass NaCl solution. CPT tests were performed in this part under high voltage of 2.40 V vs. SCE to be able to detect the CPT and relate it to the processing parameters. Measured values of the density of the samples were used to calculate their porosity. Finally, the significant processing parameters were related to samples' properties of surface roughness, CPT, density and porosity through a model equation.

5.1 Results of Part One: Electrochemical Testing of Ti-6Al-4V Parts Manufactured in Electron Beam Melting Machine and Comparison with Wrought Ti-6Al-4V Alloy

5.1.1 Potentiodynamic Testing

The following outcomes were obtained with potentiodynamic tests:

- ***Comparison of the polarization curve of Ti-6Al-4V alloy manufactured by EBM machine and by conventional wrought method at room temperature in NaCl solution.***

Figures 40 and 41 show polarization curves for Ti-6Al-4V tested at 23ºC in 3.5% mass NaCl solution for the EBM and wrought alloy, respectively. The start of the curve at low potential represents the cathodic region that shows the current decrease with increasing potential due to the cathodic reaction where hydrogen gas is formed. The point at which the anodic current equals to the cathodic current is called corrosion potential and it is -0.45 and -0.49 V vs. SCE for the EBM alloy and the wrought alloy, respectively. The anodic part of the curve then appears where the current increases with increasing potential, indicating the potential value of the metal is increasing over the corrosion potential value. This region represents the active state of the curve. Contrary to the stainless steel curves shown in Figure 42, titanium alloys have a longer passivation region that extends from 0.3 to 1.3 V vs. SCE with a 2.45 $\mu A/cm^2$ of passivation current density (I_{pass}). This passivation is due to the formation of titanium oxide layer that protects the surface from any further dissolution. Specifying the passivation region of a metal allows for controlling the corrosion rate. The corrosion rate of an active-passive metal can be reduced by shifting the corrosion potential of the metal to a value in the passive region, thus increasing the corrosion resistance of the metal.

After this passive state, the metal passes through a transpassive state where the current increases rapidly in a small range of potential which signifies the start of the breakdown of the protective layer. This transpassive breakdown happens at a potential around 1.5 V vs. SCE for both titanium alloys, which is outside the thermodynamic stability of water. After this potential, oxygen gas is formed due to the decomposition of water and a bump appears in the polarization curve since the evolved oxygen bubbles on

the sample surface cover part of the exposed surface to the solution. The corrosion rate is low in the passive region but increases in the transpassive region with the potential increase. When a broad increase of current density is observed in a small potential range, corrosion occurs continuously. The potential value at which this rapid corrosion takes place is called the pitting potential value (E_{pit}), which is 6.25 and 6.06 V vs. SCE for EBM and wrought alloy, respectively.

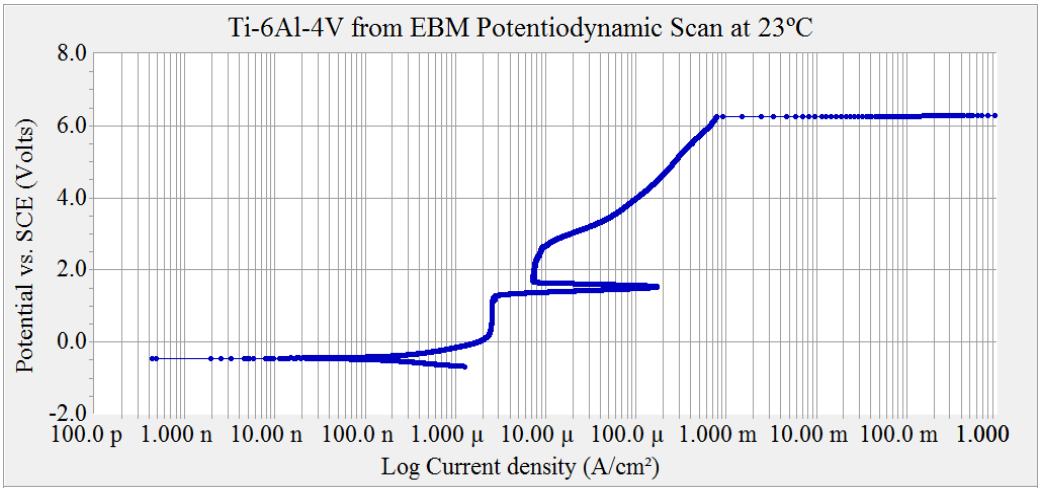

Figure 40: Polarization curve for Ti-6Al-4V from EBM machine at 23ºC in 3.5% mass NaCl solution.

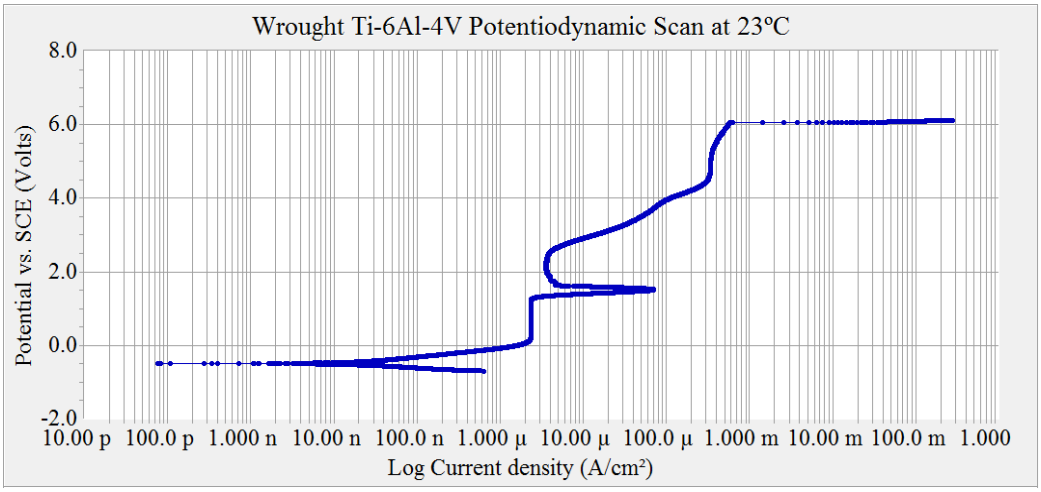

Figure 41: Polarization curve for wrought Ti-6Al-4V at 23ºC in 3.5% mass NaCl solution.

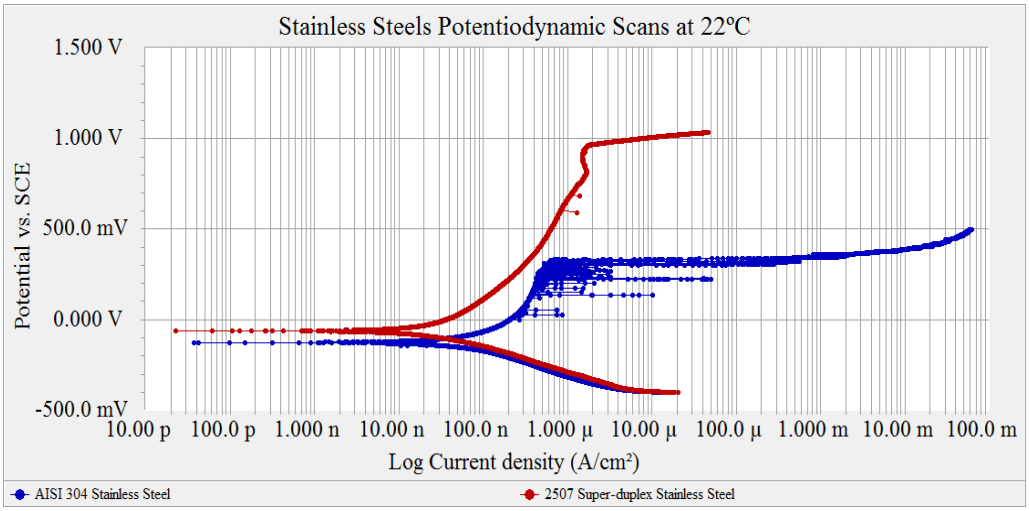

Figure 42: Polarization curves for type 304 stainless steel and type 2507 super-duplex stainless steel at 22ºC in 3.5% mass NaCl solution (Khalfaoui, 2013).

Figure 42 shows polarization curves for two types of stainless steels: AISI 304 stainless steel and 2507 super-duplex stainless steel (Khalfaoui, 2013). In comparison to the Ti-6Al-4V curves in Figures 40 and 41, both stainless steels have a narrower range of passivation region under lower values of potentials which is the reason for their lower corrosion resistance. Metastable pits happened before the continuous pitting of 304 stainless steel; these pits appeared as current fluctuations close to its pitting potential of 0.36 V vs. SCE. 2507 super-duplex stainless steel has better corrosion resistance as it has higher pitting potential of 1.0 V vs. SCE.

It was clear that Ti-6Al-4V maintained its passivity regardless of the manufacturing method. Both EBM and wrought titanium alloy maintained a good range of passivity, and had a high pitting potential.

- ***Pitting potential determination for Ti-6Al-4V parts manufactured by EBM machine and by conventional wrought method in NaCl solution at different temperatures.***

Pitting potential (E_{pit}) was obtained from the potentiodynamic curve which is the potential at which the anodic current increases and continues to increase at all potentials (Jones, 1996). E_{pit} was located where the current density increase abruptly. Potentiodynamic scans at different temperatures for Ti-6Al-4V from the

EBM machine are presented in Figure 43 and for wrought alloy in Figure 44. As seen in the charts in Figures 43 and 44, a rapid increase in the current occurs at high potential indicating stable pitting. All charts show similar behavior of the alloy manufactured in both techniques; a passivation region appeared in a potential range of 0.3-1.3 V vs. SCE of the anodic curve, and then the current density increased with the potential increase in the transpassive state until stable pits formed. Fluctuations in the recorded current measurements were noticed at temperatures higher than 50ºC. In addition, oxygen bubbles for wrought alloy were not observed after 50ºC since E_{pit} in those curves had a lower value than water stability potential, 1.5 V vs. SCE.

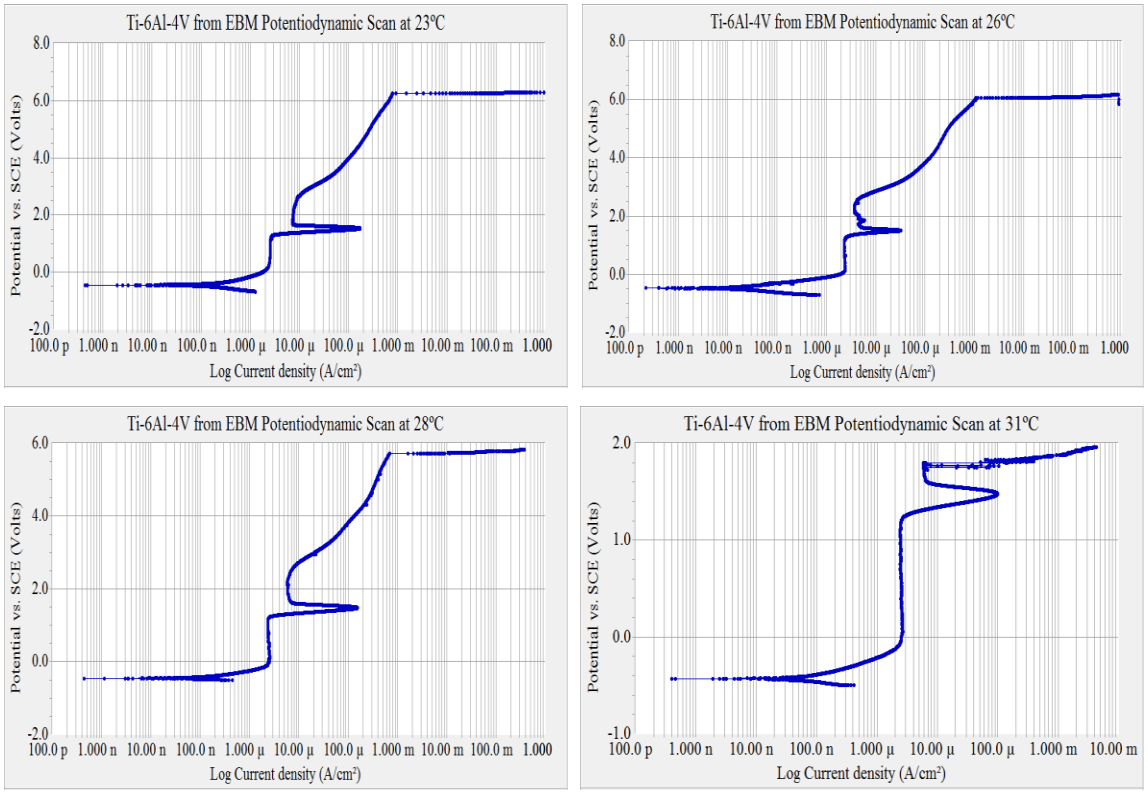

Figure 43: Potentiodynamic scan of Ti-6Al-4V manufactured in EBM machine conducted in 3.5% mass NaCl solution at different temperatures.

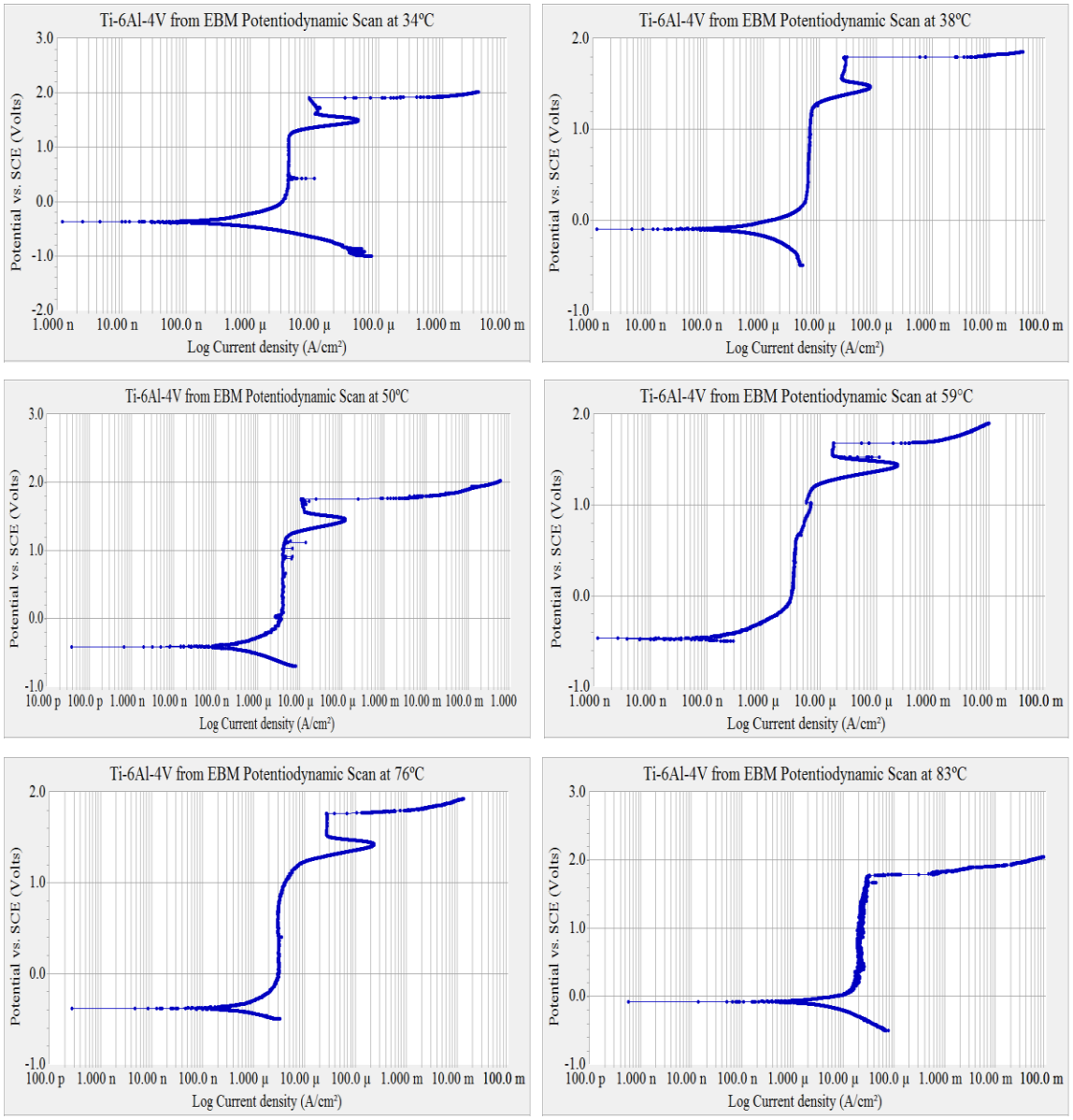

Figure 44: Continued.

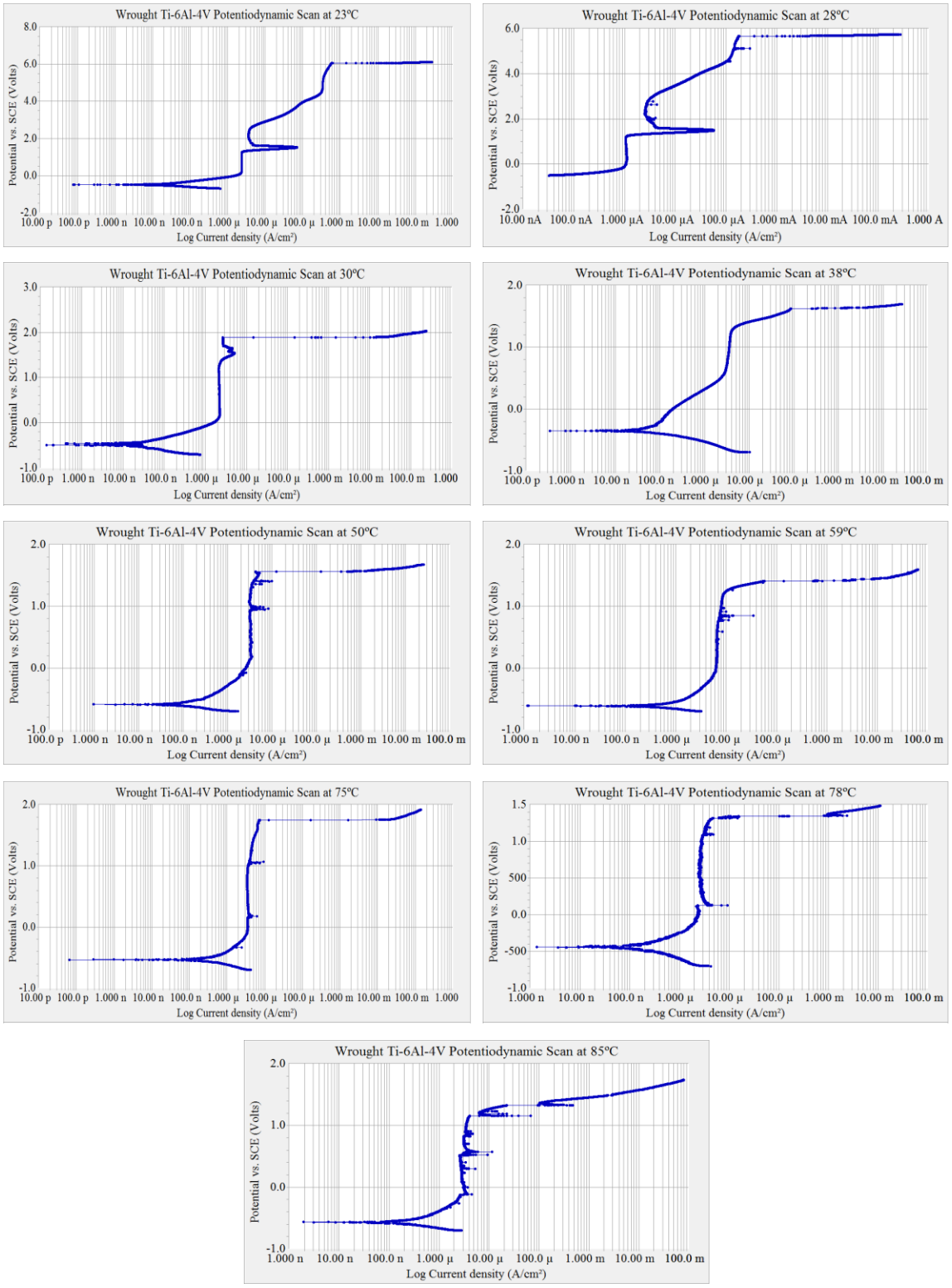

Figure 45: Potentiodynamic scan of wrought Ti-6Al-4V conducted in 3.5% mass NaCl solution at different temperatures.

Tables 13 and 14 list the pitting potential at different temperatures for the Ti-6Al-4V manufactured in the EBM machine and for the wrought alloy, respectively. When comparing both tables, it was noticed that values of E_{pit} at a certain temperature are almost the same for both alloys, which indicates that corrosion resistance of both materials in NaCl solution is the same even at higher temperatures. A rapid decrease in potential occurred around 30°C for both alloys. At temperatures higher than 30°C, it was observed that E_{pit} for EBM samples stays almost constant at a value of 1.77 V vs. SCE with a lowest E_{pit} of 1.69 V vs. SCE at 59ºC. E_{pit} for wrought alloy decreases with increasing temperature, and the lowest E_{pit} was 1.32 V vs. SCE at 85ºC. This shows that the EBM alloy has higher pitting corrosion resistance than the wrought alloy at higher temperatures. However, since the lowest E_{pit} is relatively high in comparison to E_{pit} for most stainless steels in the same environment, both titanium alloys are still considered of high and similar corrosion resistance. E_{pit} for stainless steels at 22ºC, shown in Figure 42, was 0.36 and 1.0 V vs. SCE for 304 and 2057 super-duplex stainless steels, respectively (Khalfaoui, 2013).

Table 13: Pitting potential of Ti-6Al-4V manufactured in EBM machine at different temperatures. Potentiodynamic tests conducted in 3.5% mass NaCl solution.

EBM Ti-6Al-4V	
Temperature (℃)	**Pitting Potential vs. SCE (Volts)**
23	6.25
26	6.07
28	5.71
31	1.77
34	1.91
38	1.78
50	1.76
59	1.69
76	1.78
83	1.77

Table 14: Pitting potential of wrought Ti-6Al-4V alloy at different temperatures. Potentiodynamic tests conducted in 3.5% mass NaCl solution.

Wrought Ti-6Al-4V	
Temperature (℃)	**Pitting Potential vs. SCE (Volts)**
23	6.06
28	5.69
30	1.88
38	1.64
50	1.57
59	1.41
75	1.75
78	1.35
85	1.32

Pitting potential values can be represented in the potential-temperature chart as shown in Figures 45 and 46 and they show the effect of changing temperature on the pitting potential of EBM Ti-6Al-4V and of wrought Ti-6Al-4V, respectively. A rapid fall in potential was obvious around 30ºC in both charts. This indicates that the CPT of this alloy is close to this temperature when performing a potentiostatic test at a constant potential around E_{pit} (Arnvig & Bisgard, 1996). This rapid decrease also indicates that the potential at which pitting is expected to occur is critical at around 30ºC. A small change in temperature around 30ºC will cause the pitting potential to drop from around 5.7 to 1.8 V vs. SCE, which is important to consider for applications performed under these conditions.

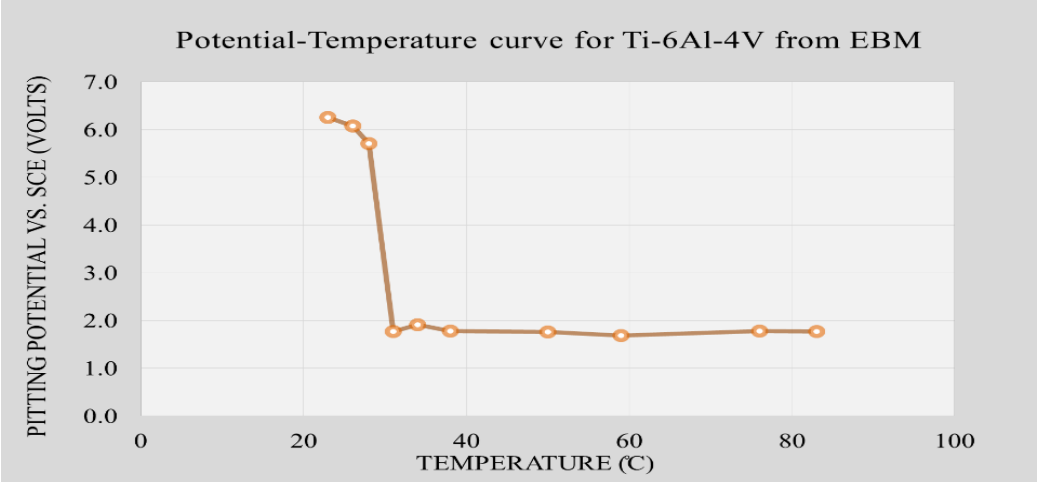

Figure 46: Effect of temeprature on the pitting potential of Ti-6Al-4V samples fabricated in an EBM machine in 3.5% mass NaCl solution.

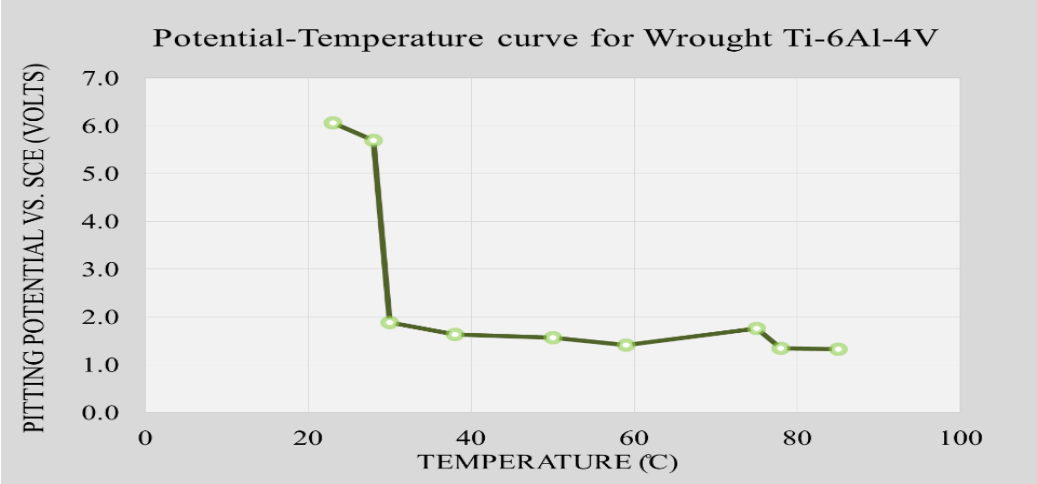

Figure 47: Effect of temperature on the pitting potential of wrought Ti-6Al-4V alloy in 3.5% mass NaCl solution.

5.1.2 Potentiostatic Testing

The following outcomes were obtained with the potentiostatic tests:

- ***Critical pitting temperature of Ti-6Al-4V manufactured by EBM machine and by conventional wrought method at 800 mV vs. SCE in NaCl solution.***

Potentiostatic tests were conducted in 3.5% mass NaCl solution. According to the ASTM standard G 150-99, the constant potential applied during the test was 800 mV vs. SCE. The materials tested were: EBM-manufactured Ti-6Al-4V, wrought Ti-6Al-4V and 316L stainless steel. Their potentiostatic tests are shown in Figures 47, 48 and 49, respectively. Wrought titanium and 316L stainless steel samples were polished to 600-grit emery paper, while the EBM sample was tested as-received to study the effect of surface roughness on CPT. Titanium alloys showed the same response during the potentiostatic test as the highest current density recorded was 30 $\mu A/cm^2$ at 100ºC when the test solution was boiling. The samples were examined after the test and no corrosion was detected under these test conditions. The samples surface was shiny without any change in their exterior appearance. On the other hand, the 316L stainless steel had a CPT of 14ºC under the same test conditions. The current density in stainless steel increased to a value higher than 500 $\mu A/cm^2$ at temperatures below 15ºC and pits were observed on the material's surface after testing.

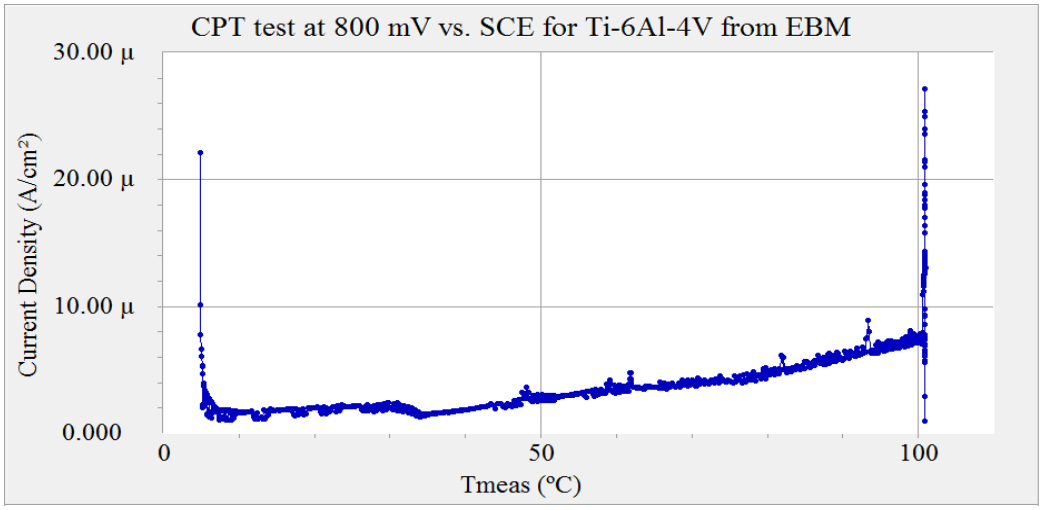

Figure 48: Potentiostatic test of EBM-manufactured Ti-6Al-4V alloy conducted at constant potential of 800 mV vs. SCE in 3.5% mass NaCl solution.

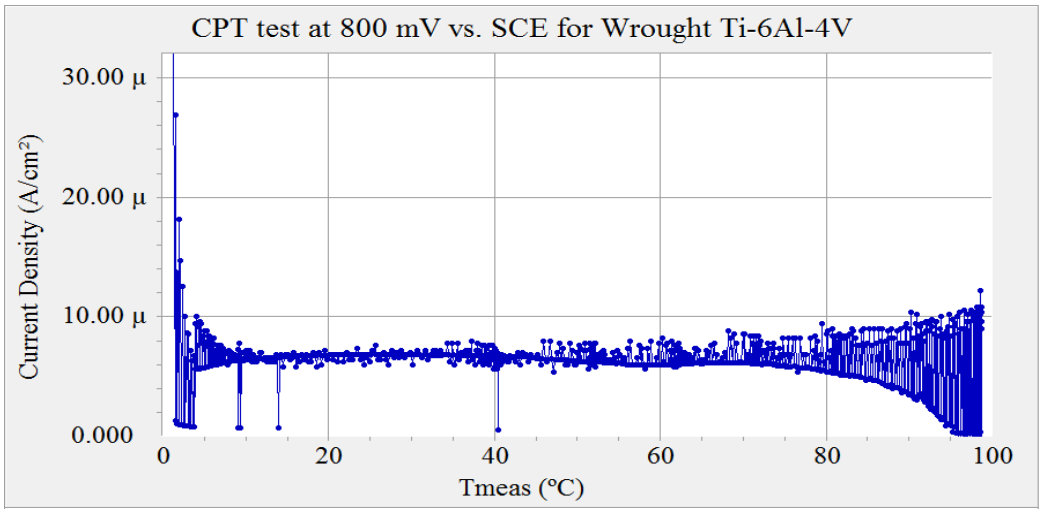

Figure 49: Potentiostatic test of wrought Ti-6Al-4V alloy conducted at constant potential of 800 mV vs. SCE in 3.5% mass NaCl solution.

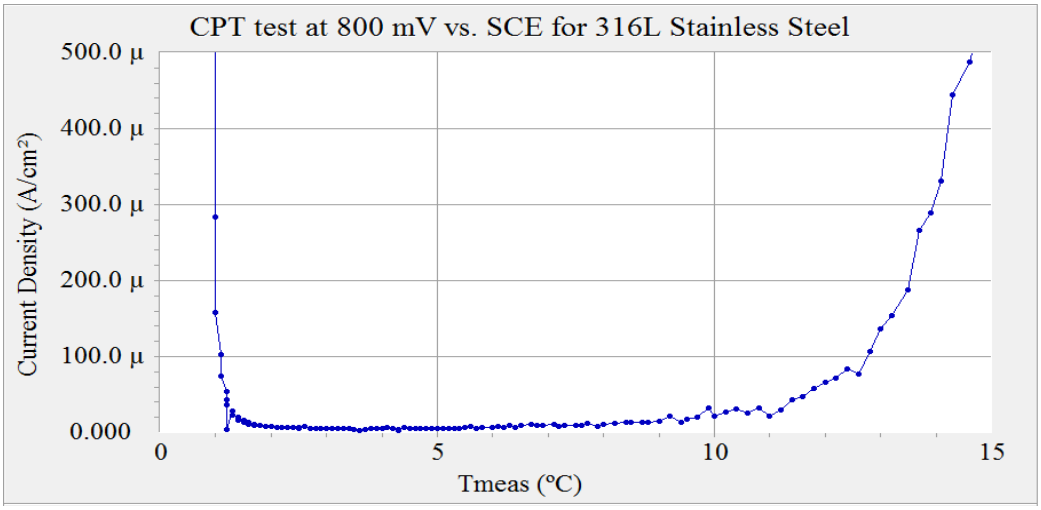

Figure 50: Potentiostatic test of 316L stainless steel conducted at potential of 800 mV vs. SCE in 3.5% mass NaCl solution.

- ***Critical pitting temperature of Ti-6Al-4V manufactured by EBM machine in NaCl solutions of different pH values***.

Since the EBM samples showed to have excellent corrosion resistance in the previous CPT test, other conditions were investigated to detect if these samples can withstand more aggressive conditions. Another set of CPT tests was conducted under the same potential but in different environments. Figures 50, 51 and 52 show potentiostatic tests performed on EBM Ti-6Al-4V in 3.5% mass NaCl solution with different pH values of 5.7, 2.0, and 10.0, respectively. The ASTM standard G 150-99 verifies CPT as the temperature at which the current density exceeds 100 µA/cm^2 for 60 seconds (ASTMG150-99, 2010). Since the current density did not increase more than 30 µA/cm^2 at 100ºC, then the sample did not pit in all conditions of changing the pH of this solution. Observations of tested samples showed no sign of any form of corrosion on the samples' surfaces.

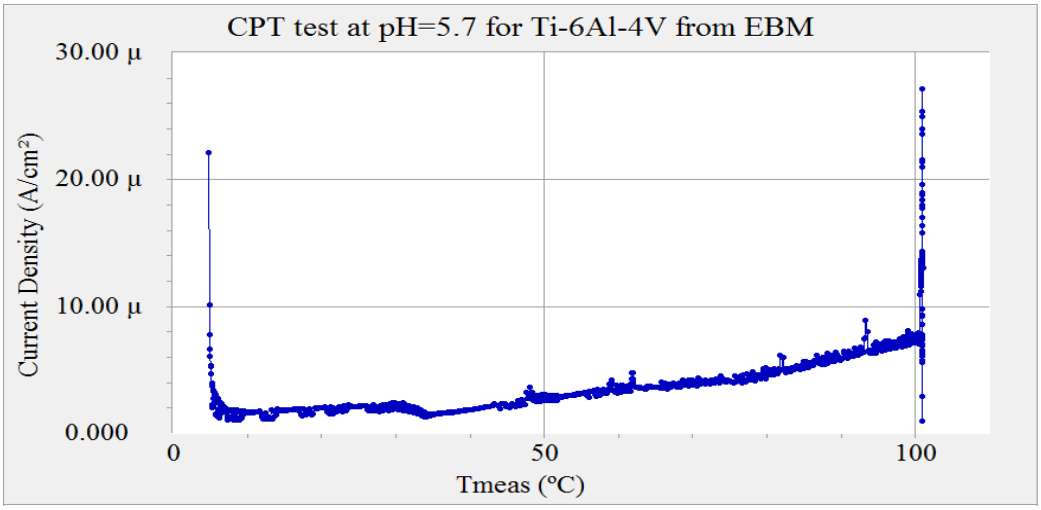

Figure 51: Potentiostatic test of EBM-manufactured Ti-6Al-4V conducted at a potential of 800 mV vs. SCE in 3.5% mass NaCl solution at pH=5.7.

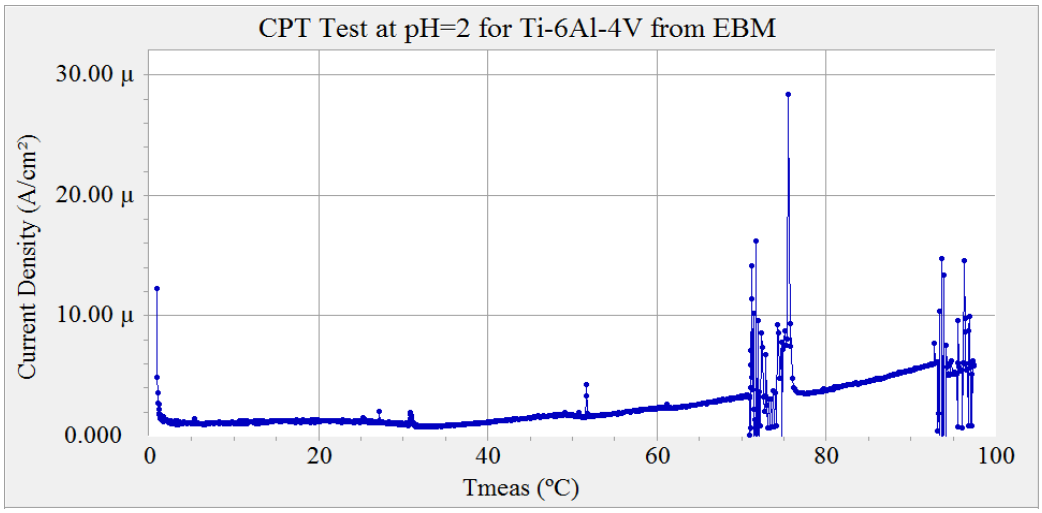

Figure 52: Potentiostatic test of EBM-manufactured Ti-6Al-4V conducted at a potential of 800 mV vs. SCE in 3.5% mass NaCl solution at pH=2.0.

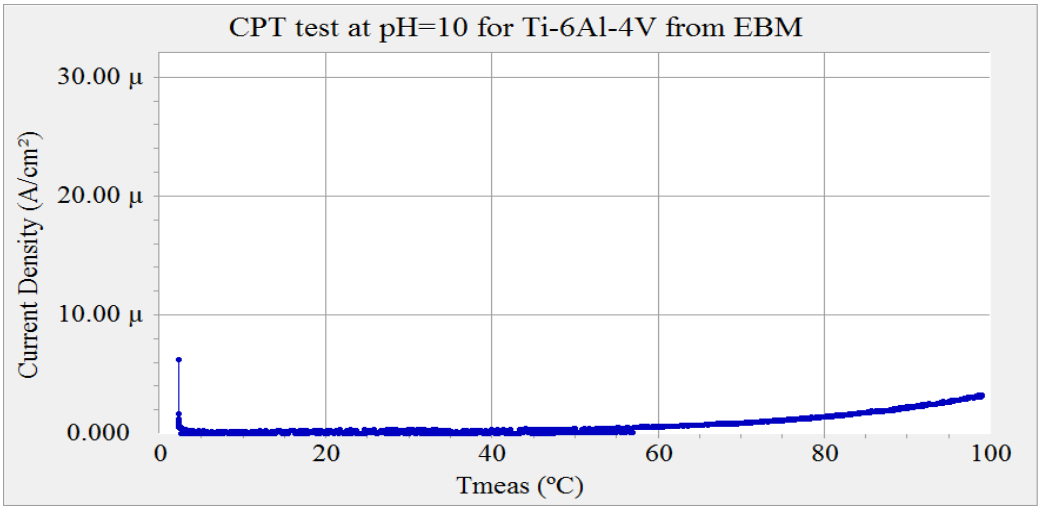

Figure 53: Potentiostatic test of EBM-manufactured Ti-6Al-4V conducted at a potential of 800 mV vs. SCE in 3.5% mass NaCl solution at pH=10.0.

Despite the variations in surface roughness and porosity of Ti-6Al-4V manufactured in the EBM machine, this material passed another property; it proved to resist pitting corrosion in NaCl solutions under test potential of 800 mV vs. SCE, regardless of the pH of the solution.

5.2 Results of Part Two: Statistical Design of Experiment for Process Parameters of Electron Beam Melting Machine

5.2.1 Effect of EBM Beam Current, Beam Speed and Offset Focus on Surface Roughness

The surface roughness of the EBM samples was measured using a 3D optical profilometer that created 5.51 mm square surface profiles of the samples. Figure 53 shows optical images for samples one through eight of Table 12 that displays the surface topography along with a roughness profile for each sample. Only one replicate of each sample is presented in this chapter, and images of all replicates are presented in Appendix A. The values of the surface roughness measured are listed in Table 15.

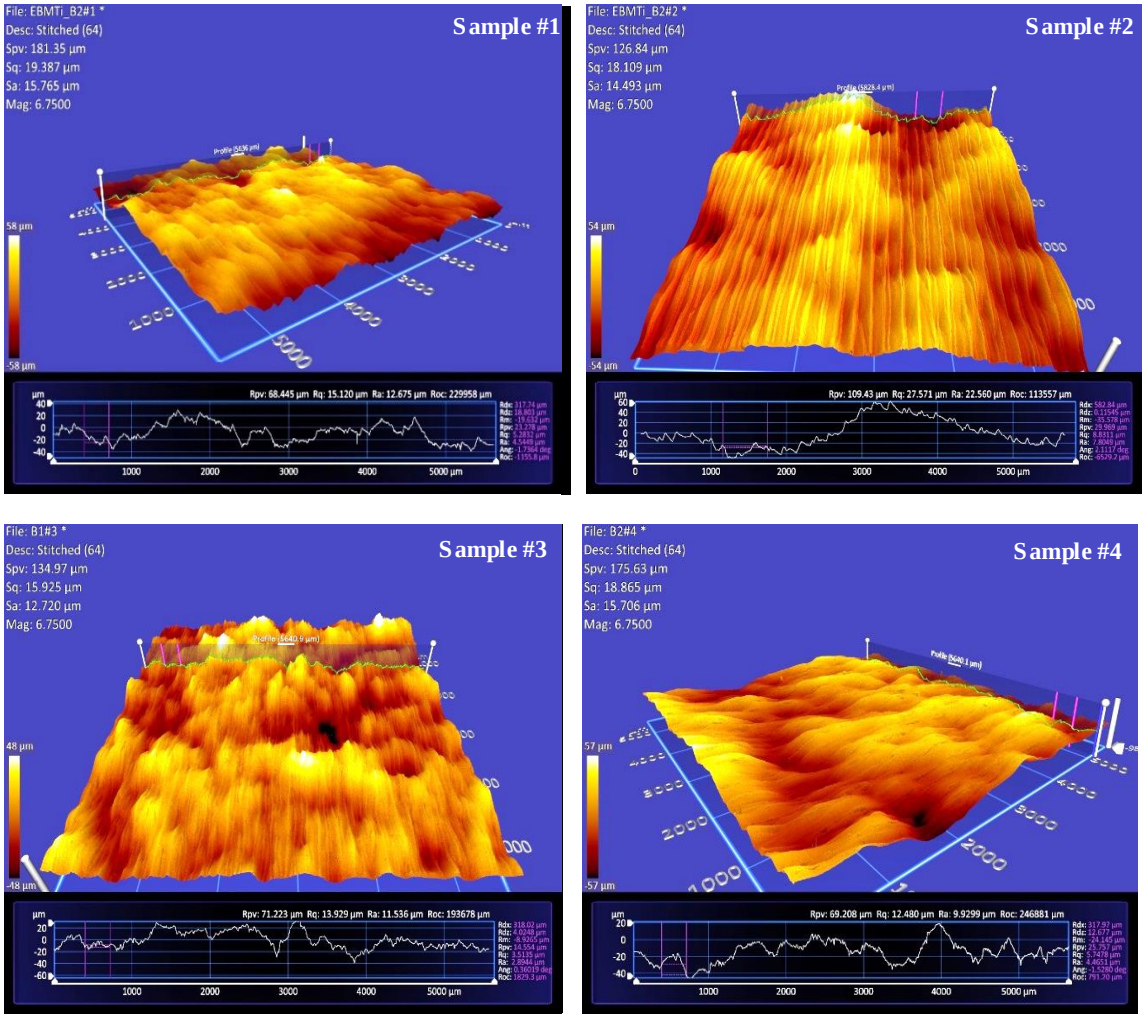

Figure 54: 3D optical images for Ti-6Al-4V samples manufactured in EBM machine under different process parameters.

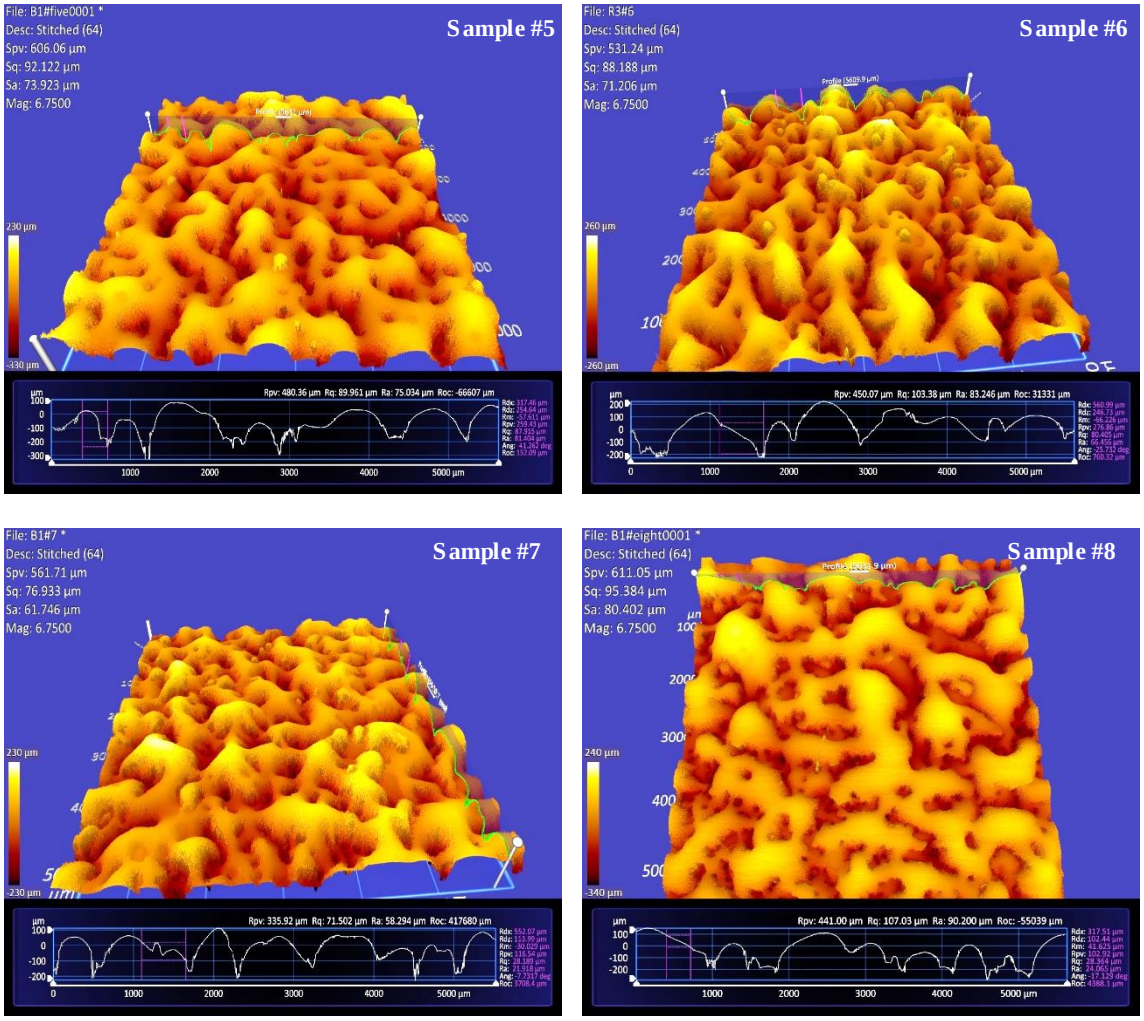

Figure 53: Continued.

From the optical images shown in Figure 53, it was observed that all samples displayed significant surface roughness. A major difference was observed between the first four samples and the last four. The first set of four samples was built with zero offset focus while the last four involved a 25 mA offset focus. The samples of zero offset focus had roughness with systematic valley and mountain-like shapes that were in the direction of the electron scans. On the other hand, samples manufactured with a 25 mA offset focus had much deeper roughness and holes that caused these samples to be porous as well. Offset focus is the amount (in mA) by which the beam is defocused from the calibrated position. When the beam focus was in

the same calibrated position –zero offset, parts produced were of a smoother surface than when the beam was deviated from the calibrated position. The wider the gap between the beam and the calibrated position, the rougher the surface. In addition, more inclusions were observed on the surface of the last four samples. This relatively high offset focus prevented complete melting of some powder particles, which made unmelted powder appear in their original spherical shape as inclusions on top of the sample surface.

Table 15: Surface roughness of Ti-6Al-4V samples manufactured in an EBM machine under different process parameters.

Sample #	Beam current (mA)	Beam speed (mm/s)	Offset focus (mA)	RMS Surface roughness (µm)			
				Replicate 1	Replicate 2	Replicate 3	Average
1	5	3000	0	15.046	19.387	18.785	17.7393
2	10	3000	0	24.027	18.109	24.713	22.2830
3	5	6000	0	15.925	17.946	12.224	15.3650
4	10	6000	0	17.153	18.865	15.77	17.2627
5	5	3000	25	92.122	99.777	89.395	93.7647
6	10	3000	25	92.616	109.080	88.188	96.6280
7	5	6000	25	76.933	88.001	76.936	80.6233
8	10	6000	25	95.384	91.123	95.872	94.1263

The values of surface roughness listed in Table 15 are in agreement with what was mentioned above. The first four samples had much lower surface roughness than the last four samples. The averages of surface roughness of the first set of samples (1-4) varied between 15.4 and 22.3 µm, while for the rest of the samples (5-8), the surface roughness averages were in the range of 80.6 - 96.6 µm. This result indicates that offset focus has a major impact on the surface roughness of produced parts. As for the other two parameters within one set of constant offset focus, increasing the speed at a constant current resulted in a decrease in surface roughness, while increasing the current at constant speed caused an increase in surface roughness. It was noticed that variations in each set of the same offset focus are not considerable in comparison to the variations that occurred between each set of a different offset focus. This points out that a change in offset focus is more significant than changes due to the beam current and beam speed.

However, a consistent trend was noticed in each set due to changes in both beam current and beam speed and is related to linear energy. Linear energy is the amount of energy transferred by electrons per unit length. It is the ratio between beam power and beam speed. Linear energy increases with increasing beam current and decreasing beam speed. Samples ones through four are of the same beam current and beam speed as in samples five through 8, correspondingly. The values of linear energy for samples one through eight in order are as follows: 100, 200, 50, 100, 100, 200, 50 and 100 J/m. Samples 2 and 6 had the highest linear energy, samples 3 and 7 had the lowest, while samples 1, 4, 5 and 8 had the same linear energy. The surface roughness increased with an increase in the linear energy. This is because high linear energy leads to a higher concentration of deposited energy, which will cause deep penetrations and generates a surface of higher roughness. Higher linear energy obtained with higher beam current and lower beam speed, this occurs because increasing beam current is associated with increased deposited energy and decreased beam speed will increase the exposed time of deposited energy over a certain distance.

Data in Table 15 was statistically analyzed using Minitab software to relate the surface roughness to significant manufacturing parameters through a model equation. Based on an analysis of variance approach (ANOVA) and with a 95% level of confidence, it was decided whether the parameter is of a significant effect to be included in the model equation or not. The Minitab program showed that 3-way interactions (effect of three parameters together) and 2-way interactions (effect of two parameters together) were of negligible influence; therefore, they were omitted from the model equation. Each process parameter has its own influence on surface roughness and no significant effect was concluded from the parameters combinations. The coded equation model obtained was as follows:

$$Surface\ roughness = 54.725 + (2.850 * current) - (2.879 * Speed) + (36.561 * offset\ focus) \quad (16)$$

where the beam current, scanning speed and offset focus are represented in the codded values of (-1, +1) and the surface roughness obtained is in μm.

Offset focus has the highest impact on surface roughness and beam speed has the lowest. Current and offset focus have a positive influence, while speed has a negative influence; surface roughness increases with increasing offset focus and beam current, while it decreases with increasing beam speed.

Measured values of surface roughness were compared to calculated values from the model equation (16). The average of residual percent of all samples was -0.5% and the average of absolute value of residual percent was 9.0%. These are acceptable values for residuals, which implies that this model is a close representation for measured roughness. Analysis table for calculating the percent and absolute residuals of surface roughness data is presented in Appendix B.

5.2.2 Effect of EBM Beam Current, Beam Speed and Offset Focus on CPT

In part one of this study, CPT for EBM titanium was measured in 3.5% mass NaCl solution under 800 mV vs. SCE. At these experimental conditions, the sample did not pit and CPT was not detected. Other CPT tests were conducted in the same NaCl solution of different pH value, but no sign of pitting was observed under this potential as well. When potential-temperature relation for EBM titanium was established (see Figures 45 and 46 in section 5.1.1), a rapid drop in the potential was noticed around 30ºC and this indicates that the CPT is around this temperature when a potentiostatic test is conducted under a constant potential of E_{pi} (Arnvig & Bisgard, 1996) $_t$. Since E_{pit} is to be applied in the potentiostatic test, it has to be above the pitting potential region but below the transpassive potential as was shown in Figure 18, the constant potential used for potentiostatic tests of EBM Ti-6Al-4V should be in the range of 1.77-5.69 V vs. SCE. Several pretests were performed and a value of 2.4 V vs. SCE was found to be the best value to use.

Potentiostatic tests conducted on samples one through eight are presented in Figure 54. The CPT test was conducted at 2.4 V vs. SCE in 3.5% mass NaCl solution. The CPT was determined as the temperature when a major increase in current density happens, which indicates that pitting corrosion occurs simultaneously. Tests for all replicates are presented in Appendix C, and only one replicate of each sample

is shown in Figure 54 in this chapter. The values of CPT measured are listed in Table 16. R1#2 stands for replicate 1 of sample #2.

In general, CPT values for all samples were comparable; the average CPT ranged from 28.8 to 32.1ºC, except for samples 3 and 7. Unlike the surface roughness, changing the offset focus from zero to 25 mA did not cause a great impact on the CPT values. All averages of the CPT values were one or two degrees above or below 30ºC excluding samples 3 and 7 which had the lowest linear energies; lowest linear energy is associated with lowest beam current and highest beam. In addition, samples 3 and 7 had the highest CPT values which indicates that these samples have the highest corrosion resistance of all, as these two samples were able to sustain more increase in temperature than the others.

Surface irregularities allow formation of stagnant regions that initiate pits within surface folds; a smoother surface is expected to have better corrosion resistance and so a higher CPT should be obtained. However, surface roughness did not seem to have significant influence on the CPT. Highest CPT was obtained for samples of surface roughness around 15 μm and 80 μm, and comparable CPT values was obtained for all other samples that had average surface roughness range of 17-96 μm. As the effect of surface roughness did not follow a consistent trend on CPT values, then surface roughness up to 96 μm did not affect the CPT of these EBM titanium samples.

On the other hand, the effect of linear energy on CPT values followed a consistent trend. The highest CPT obtained was in replicate 3 of sample #3 (R3#3) with the lowest linear energy, while the lowest CPT was recorded with replicate 3 of sample #2 (R3#2) that had the highest linear energy. Almost the same values of CPT were obtained for samples 1 and 4 and for samples 5 and 8, which have the same linear energies. However, differences were noticed in the CPT values between replicates of some samples, depending on surface conditions for that sample.

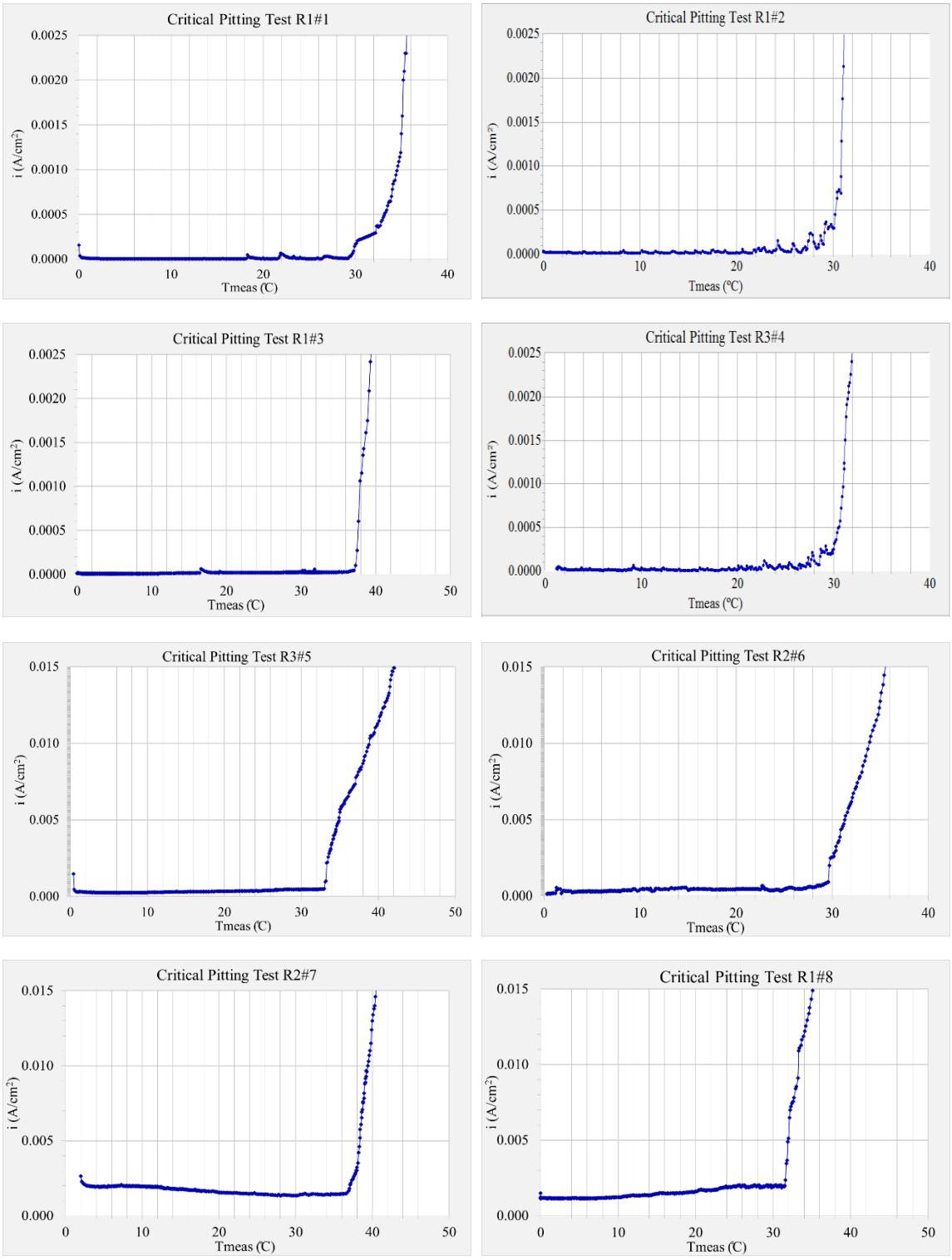

Figure 55: Potentiostatic tests for EBM Ti-6Al-4V samples conducted in 3.5% mass NaCl solution at a potential of 2.40 V vs. SCE.

In general, the CPT ranges did not vary widely, indicating that EBM titanium alloy retained its corrosion resistance regardless of values of the processing parameters of the EBM machine. In addition, the change of surface roughness from 15 µm to 80 µm did not have a significant effect on CPT values obtained.

Using Minitab software, a model equation was established and CPT was related to significant processing parameters as shown in equation (17):

$$CPT = 32.12 - (1.760 * current) + (1.750 * Speed) - (1.098 * current * speed) \quad (17)$$

where the factors in the equation, current and speed, are represented in the codded values of (-1, +1) and the CPT obtained is in ºC.

As previously mentioned in the above data analysis, offset focus did not significantly affect the CPT as it was omitted from the model equation. However, beam current, beam speed and their interaction factor were of a significant effect on CPT. Beam current and beam speed had a greater effect than their interaction factor. Both current and the interaction factor of current and speed decreased the CPT, while the speed increased the CPT.

Table 16: Critical Pitting Temperature (CPT) of Ti-6Al-4V samples manufactured in an EBM machine under different process parameters.

Sample #	Beam current (mA)	Beam speed (mm/s)	Offset focus (mA)	CPT (˚C)			
				Replicate 1	Replicate 2	Replicate 3	Average
1	5	3000	0	29.30	32.80	27.21	29.77
2	10	3000	0	30.85	30.71	24.90	28.82
3	5	6000	0	37.30	36.20	39.79	37.76
4	10	6000	0	31.80	29.80	30.09	30.56
5	5	3000	25	31.60	31.80	32.90	32.10
6	10	3000	25	30.30	29.70	31.80	30.60
7	5	6000	25	34.20	36.70	36.20	35.70
8	10	6000	25	31.60	30.80	32.00	31.47

The CPT calculated with the model equation (17) was compared to measured values in Table 16. The average of residual percent of all samples was -0.4% and the average of absolute value of residual percent was 4.4%. This means that the suggested model for CPT comes in agreement with measured values. Analysis table for calculating the percent and absolute residuals of critical pitting temperature (CPT) data is presented in Appendix B.

The samples were inspected after CPT test with an optical microscope to detect pitting. Images are shown in Figure 55 for samples 1 through 8. Pits appeared at discrete areas on the sample surface with an oxide layer covering the surface of the pit. For the first four samples of zero offset focus, the spread of pitting corrosion followed the track of the ripples that exists on the surface according to the electron beam scanning direction. While for the other set of high offset focus, the corrosion covered the deep holes with a layer of oxide and was spread along more than one hole as well.

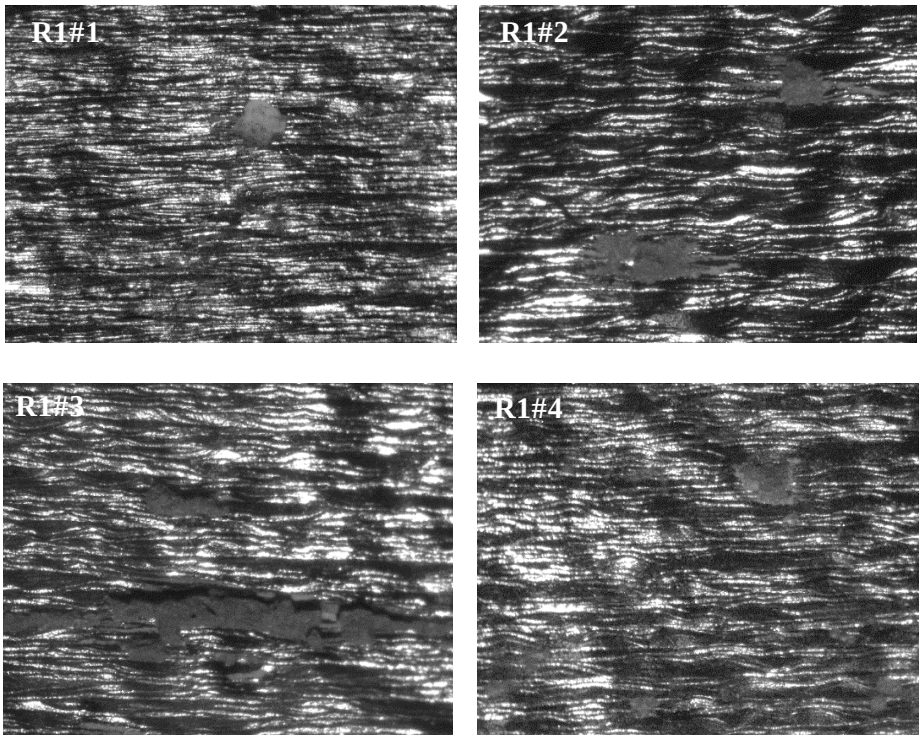

Figure 56: Optical images for EBM Ti-6Al-4V samples after CPT test.

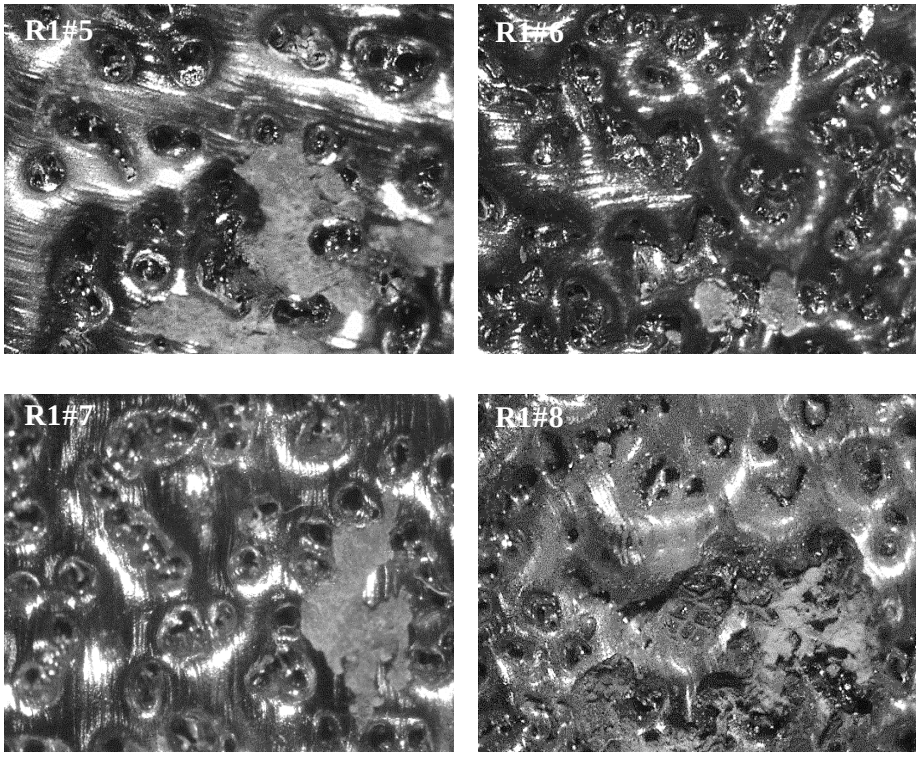

Figure 55: Continued.

5.2.3 Effect of EBM Beam Current, Beam Speed and Offset Focus on Density and Porosity

Measured values of density are listed in Table 17 along with the calculated porosity. These two properties were affected by the change in offset focus more than any change in beam current and beam speed. The density of the first set of four samples with zero offset focus was higher than that of the second set with 25 mA offset focus. Higher offset focus formed deep curvatures and cavities within the sample, which decreased the density of the material. However, no specific trend was detected in each set of the four samples, indicating that alterations in beam current and beam speed will not influence the density. The same pattern in porosity outcomes was noted. The second set of 25 mA offset focus has a higher porosity than the first set. The range of porosity was 0.21-0.52% and 9.13-10.11% for the first and second set, respectively, and variations in beam current and beam speed did not cause any major differences in porosity values within each set of the same offset focus.

Table 17: Density and porosity of Ti-6Al-4V samples manufactured in EBM machine under different process parameters.

Sample #	Beam current (mA)	Beam speed (mm/s)	Offset focus (mA)	Sample Average density (g/cm^3)				Porosity			
				Replicate 1	Replicate 2	Replicate 3	Average	Replicate 1	Replicate 2	Replicate 3	Average
1	5	3000	0	4.4376	4.3998	4.3892	4.4089	0.40	0.46	0.70	0.52
2	10	3000	0	4.4073	4.4146	4.4105	4.4108	0.29	0.12	0.21	0.21
3	5	6000	0	4.4122	4.4305	4.4314	4.4247	0.18	0.24	0.26	0.22
4	10	6000	0	4.4011	4.4271	4.4325	4.4203	0.43	0.16	0.28	0.29
5	5	3000	25	4.0175	4.0055	4.0133	4.0121	9.11	9.38	9.20	9.23
6	10	3000	25	4.0021	4.0232	4.0239	4.0164	9.46	8.98	8.96	9.13
7	5	6000	25	4.0236	3.9641	4.0186	4.0021	8.97	10.31	9.08	9.45
8	10	6000	25	3.8805	4.0213	4.0172	3.9730	12.21	9.02	9.11	10.11

The model equations obtained for density and porosity are shown in equations (18) and (19), respectively with a Minitab program. Offset focus was the only significant parameter to affect these properties. As noticed from the below equations, increasing offset focus will decrease density and increase porosity.

$$Density = 4.209 - (0.208 * offset\ focus) \quad (18)$$

$$Porosity = 4.896 + (4.586 * offset\ focus) \quad (19)$$

where the offset focus is represented in the codded values of (-1, +1), the density obtained is in g/cm^3 and the porosity obtained is a percentage value.

Analysis to confirm the validity of these equations was performed and the average of residual percent of all samples was 0.0% and -12.7% for density and porosity, respectively. In addition, the average of absolute value of residual percent was 0.5% and 26.7% for density and porosity, respectively. Analysis tables for calculating the percent and absolute residuals of density and porosity data are presented in Appendix B.

For the four properties studied above, the probabilities (P) of each build parameter to have a significant effect on the property studied are listed in Table 18. With 95% confidence level, a factor (build

parameter) is considered to be significant when it has a probability greater than 95%. Number of standard deviations from the center (T) of each build parameter are also shown in the same table, where higher deviations from the center indicates higher influence of that build parameter on the property. Finally, coded coefficients relate the build parameters to the property. They are coded with values assigned for the build parameter as -1 and +1 for the low and for the high value of that build parameter, respectively.

Table 18: Probability (P), percentage of significance, number of standard deviations from the center (T) and coded coefficient for the effect of each build parameter on the properties studied.

Property	Surface roughness				CPT			
Build parameter	P	Significance % (1-p)	T	Coded coefficent	P	Significance % (1-p)	T	Coded coefficent
Constant	0.000	99.9+%	48.65	54.725	0.000	99.9+%	81.52	32.123
Beam current	0.020	98.0%	2.53	2.850	0.000	99.9+%	-4.47	-1.760
Beam speed	0.010	99.0%	-2.56	-2.879	0.000	99.9+%	4.44	1.750
Offset focus	0.000	99.9+%	32.50	36.561	-	-	-	-
Beam current* Scan speed	-	-	-	-	0.011	98.9%	-2.79	-1.098
Property	Density				Porosity			
Build parameter	P	Significance % (1-p)	T	Coded coefficent	P	Significance % (1-p)	T	Coded coefficent
Constant	0.000	99.9+%	659.79	4.209	0.000	99.9+%	35.69	4.896
Beam current	-	-	-	-	-	-	-	-
Beam speed	-	-	-	-	-	-	-	-
Offset focus	0.000	99.9+%	-32.55	-0.208	0.000	99.9+%	33.43	4.586
Beam current* Scan speed	-	-	-	-	-	-	-	-

CHAPTER VI

CONCLUSIONS

The present research evaluated a Ti-6Al-4V alloy fabricated in an Electron Beam Melting machine (EBM) and compared it with a wrought Ti-6Al-4V alloy. Potentiodynamic testing in 3.5% mass NaCl solution at room temperature (23ºC) showed similar corrosion behavior of the alloy manufactured in both techniques. A protective oxide layer developed on the alloy's surface in a potential range of 0.3-1.3 V vs. SCE, which contributed to the alloy unique corrosion resistance. Both Ti-6Al-4V alloys passivate with a passivation current density of 2.45 $\mu A/cm^2$. A transpassive state of the metal starts at a potential of 1.5 V vs. SCE. This potential is outside the thermodynamic stability region of water where water begins to decompose and oxygen bubbles evolve. Bubbles presence on sample's surface cause an increase in current density which appears as a bump in the polarization curve. The transpassive state continues and current density increases as a metastable breakdown of the film takes place, until a stable pitting occurs at a pitting potential of 6.25 and 6.06 V vs. SCE for EBM and wrought titanium alloy, respectively. This is a relatively high pitting potential in comparison to most stainless steels. In general, Ti-6Al-4V maintained its resistance regardless of how it was manufactured. Both the EBM and wrought alloy maintained a good range of passivity and had a relatively high pitting potential.

Pitting potential was also detected with potentiodynamic tests at different temperatures to evaluate corrosion resistance of the Ti-6Al-4V alloy manufactured by both methods. Again, both alloys showed similar results even at higher temperatures as it was noticed from the potential-temperature curves established for EBM and wrought titanium alloy. A major drop in the pitting potential happened around 30ºC and the pitting potential decreased from nearly 5.7 V to 1.8 V vs. SCE. This indicates that the critical pitting temperature (CPT) of both alloys is close to this temperature when conducting a potentiostatic test at a constant potential around the pitting potential E_{pit}. This rapid fall in potential also indicates that the pitting

potential of Ti-6Al-4V around 30ºC is critical, as minor changes in temperature might cause the pitting to occur at considerable lower potentials.

Critical pitting temperature (CPT) was used as another indicator for comparing corrosion resistance of the EBM alloy with the wrought alloy. In 3.5% mass NaCl solution at a standard potential of 800 mV vs. SCE, a potentiostatic test for both titanium alloys did not result in any pitting corrosion, as the current density did not exceed 30 $\mu A/cm^2$ when the temperature reached 100ºC. While CPT test conducted at the same conditions for 316L stainless steel resulted in a CPT at 14ºC. The same potentiostatic test was conducted for the Ti-6Al-4V alloy produced with the EBM machine but in NaCl solutions of different pH values of 5.7, 2.0 and 10.0. Despite the variations in surface roughness and porosity of the EBM titanium, results showed that the EBM titanium was capable to withstand more aggressive conditions in NaCl solutions of different pH values, as no sign of pitting was detected in these tests as well.

Parts produced in the EBM machine have different properties depending on the processing parameters specified for that machine. In a statistically designed experiment, beam current, beam speed and offset focus were examined for their effect on surface roughness, CPT, density and porosity of the Ti-6Al-4V samples manufactured in an EBM system. Surface roughness measurements showed curvatures on the samples' surface which appeared due to the fabrication technique. Offset focus had the largest impact on surface roughness over beam current and beam speed. Surface roughness increases with increasing offset focus. Samples of zero offset focus had roughness of systematic valley and mountain-like shapes that were in the direction of the electron scan, while samples manufactured with 25 mA offset focus had higher roughness and holes that caused these samples to be porous as well. Average surface roughness were around 17 μm and 93 μm for samples of zero and 25 mA offset focus, respectively. Beam current and beam speed had a lower effect on surface roughness, but this effect is almost consistent and relates to the linear energy that increased with increasing beam current and with decreasing beam speed. Surface roughness was found to increase with increasing linear energy and offset focus.

Conducting a potentiostatic test in 3.5% mass NaCl solution at a constant potential of 2.40 V vs. SCE resulted in CPT averages in the range of 28.82 - 37.76ºC. The highest CPT was associated with the lowest linear energy and the lowest CPT was recorded for the samples of the highest linear energy. Beam current, beam speed and their combination had a significant effect on the CPT value, more than the offset focus. Overall, CPT ranges did not vary widely, indicating that the EBM titanium alloy had the same corrosion resistance regardless of the values of the processing parameters of the EBM machine. In addition, the change of surface roughness from 15 μm to 80 μm did not have a significant effect on CPT values obtained for EBM Ti-6Al-4V parts.

The density and porosity of EBM parts were greatly affected by offset focus. Changing offset focus from zero to 25 mA resulted in an almost 10% decrease in density and an increase in porosity of nearly 18 times more for the samples of higher offset focus. Minor and inconsistent changes occurred in density and porosity measurements due to changes in beam current and beam speed, while offset focus had the most influence recorded.

In conclusion, the Ti-6Al-4V alloy manufactured in an EBM machine had the same corrosion behavior as a wrought alloy as both alloys showed to have the same pitting potential in 3.5% mass NaCl solution, even at higher temperatures tested. The EBM alloy did not pit under the standard conditions of the potentiostatic test and maintained its corrosion resistance in NaCl solutions of different pH values. In addition, changing processing parameters did not have a high impact on the alloy's corrosion behavior. Parts produced from the EBM system can be controlled in order to achieve a specific range of surface roughness and porosity in order to match the application it is used in. However, uniform and precise roughness and porosity are not achievable through this machine as many factors plays a role in the properties of the resulted object.

REFERNCES

Abdulmageed, M. H. & Ibrahim, S. I., 2010. Corrosion Behavior of Ti-6Al-4V Alloy in Different Media. *Al-Khawarizmi Engineering Journal*, 6(3), pp. 77-84.

Abou Shahba, R. M. G. W. A. E.-S. A. E., 2011. Corrosion and Inhibitation of Ti-6Al-4V Alloy in NaCl Solution. *International Journal of Electrochemical Science,* pp. 5499-5509.

Ackelid, U., 2006. *The Aluminum Alloy 6061 Produced with the arcam EBM Process: A Feasibility Study,* Molndal, Sweden: Arcam AB.

Agarwala, M. K. & Jamalabad, V. R., 1996. Structural Quality of Parts Procesed by Fused Deposition. *Rapid Prototyping Journal*, 2(4), pp. 4-19.

Arcam, 2013. *Arcam A2: Products: Arcam.* [Online]
Available at: http://www.arcam.com/technology/products/arcam-a2/
[Accessed July 2013].

Arnvig, P.-E. & Bisgard, A. D., 1996. *Determining the Potential Independent Critical Pitting Temperature (CPT) by a Potentiostatic Method Using the Avest Cell.* Denver, Colorado, NACE International.

ASTMG150-99, 2010. ASTM G150-99: Standard Test Method for Electrochemical Critical Pitting Temperature Testing of Stainless Steels. *ASTM International.*

ASTMG5-94, 2004. ASTMG5-94 (Reapproved 2004): Standard Reference Test Method for Making Potentiostatic and Potentiodynamic Anodic Polarization Measurements. *ASTM International ,* pp. 45-56.

Azom, 2002. *Materials applications: Titanium: Azom.* [Online]
Available at: URL: http://www.azom.com/article.aspx?ArticleID=1297
[Accessed April 2013].

Bass, B. S., 2007. *Validating the Arcam EBM Process as an Alternative Fabrication Method for Titanium-6Al-4V Alloys.* Raleigh(North Carolina): North Carolina State University.

Boyer, R., Collings, E. & G., W., 1994. Physical Metallurgy of Titanium Alloys. In: *Materials properties Handbook.* s.l.:ASM International.

Branzoi, V. et al., 2005. Polarization Behavior of Pure Titanium in Different Media of Chloride. *Revue Roumaine de Chimie*, 50(11-12), pp. 1013-1018.

Callister, W. & Rethwisch, D., 2007. *Fundamentals of Materials Science and Engineering.* s.l.:Wiely & Sons (Asia).

Campbell, F. C., 2008. *Elements of Metallurgy and Engineering Alloys.* s.l.:ASM International.

Campbell, I., Bourell, D. & Gibson, I., 2012. Additive manufacturing: rapid prototyping comes of ages. *Rapid Prototyping Journal,* 18(4), pp. 255-258.

Chua, C. K., Leong, K. F. & Lim, C. S., 2003. *Rapid Prototyping: Principles and Applications*. Singapore: World Scientific.

Donachie, J. M. J., 2000. *Titanium: A Technical Guide (2nd Edition)*. s.l.:ASM International .

Ebrahimi, N. et al., 2012. A Comperative Study of Critical Pitting Temperature (CPT) of Stainless Steels by Electrochemical Impedance Spectroscopy (EIS), Potentiodynamic and Potentiostatic Techniques. *Corrosion Science*, Volume 59, pp. 96-102.

Engineer, T., 2011. *Rapid prototyping technology keeps race team on track*. [Online]
Available at: http://www.theengineer.co.uk/channels/design-engineering/in-depth/rapid-prototyping-technology-keeps-race-team-on-track/1008545.article

Frankel, G., 2003. Pittin Corrosion, Corrosion: Fundamentals, Testings, and Protection. In: *ASM Handbook* . s.l.:ASM Insternational, pp. 236-241.

Gaytan, S. et al., 2009. Microstructure and mechanical properties of electron beam-rapid manufactured Ti-6Al-4V biomedical prototypes compared to wrought Ti-6Al-4V. *Materials Characterization*, Issue 60, pp. 96-105.

Gilbert, C., Pauline, S. & Radovan, K., 2011. *Digital Engineering of Bio-Adaptable Dental Implants*. [Online]
Available at: http://www.intechopen.com/books/implant-dentistry-a-rapidly-evolving-practice/digital-engineering-of-bioadaptable-dental-implants
[Accessed July 2013].

Gurrappa, I., 2003. Characterization of Titanium Alloy Ti-6Al-4V for Chemical, Marine and Industrial Applications. *Materials Characterization*, Issue 51, pp. 131-139.

Hopkinson, N., Hague, R. & Dickens, P., 2005. *Rapid Manufacturing an Industrial Revolution for the Digital Age*. s.l.:John Wiley and Sons, Ltd.

Jones, D. A., 1996. *Principles and Prevention of Corrosion*. Upper Saddle River, NJ: Prentice Hall.

Khalfaoui, W., 2013. United Arab Emirates, s.n.

Koike, M. et al., 2011. Evaluation of Titanium Alloy Fabricated Using Electron Beam Melting System for Dental Applications. *Journal of Materials Processing Technology*, Issue 211, pp. 1400-1208.

Leyens, C. P. M., 2003. *Titanium and Titanium Alloys: Fundamentals and Applications*. Germany: Wiley-VCH.

Liou, J., Nagel, K. & W., F., 2012. *Hybrid Manufacturing System Design and Development*. Chicago, Illinois, USA, ASME.

Mahale, T. R., 2009. *Electron Beam Melting of Advanced Materials and Structures, mass customization, mass personalization*. North Carolina: Library of North Carolina State University.

Martin, E., Azzi, M., Salishchev, G. & Szpunar, J., 2010. Influence of Microstructure and Texture on the Corrosion and Tribocorrosion Behavior of Ti-6Al-4V. *Tribology International*, Issue 43, pp. 918-924.

Moayed, M., Laycock, N. & Newman, R., 2003. Dependence of the Critical Pitting Temperature on Surface Roughness. *Corrosion Science*, Issue 45, pp. 1203-1216.

Murr, L., Greer, P., Mari, K. & Owen, K., 2011. Evaluation of Titanium Alloys Fabricated Using Rapid Prototyping Technologies - Electron Beam Melting and Laser Beam Melting. *Materials*, Issue 4, pp. 1776-1792.

Neville, Anne; Xu, Jie, 2011. An Assesment of the instability of Ti and its Alloys in Acidic Environment at Elevated Temperature. *Journal of Light Metals*, Issue 1, pp. 119-126.

Newell, A. P., 2009. *Microstructure Studies of Ti-6Al-4V Near-Net Shape Structural Components as Prepared by the Arcam Electron Beam Melting Process.* Raleigh(North Carolina): North Carolina State University.

Noort, R. V., 1987. Review Titanium: The Implant Material of Today. *Journal of Materials Science,* 22(11), pp. 3801-3811.

Pandey, P. M., Reddy, N. V. & Dhande, S. G., 2003. Slicing Procedure in Layered Manufacturing. *Rapid Prototyping Journal*, 9(5), pp. 274-288.

Qvarfort, 1989. Critical Pitting Temperature Measurements of Stainless Steels with an Improved Electrochemical Method. *Corrosion Science*, 29(8), pp. 987-993.

Rafi., K. H., Karthik, N. V., Starr, T. L. & Stucker, B. E., 2012. *Mechanical Property Evalutaion of Ti-6Al-4V Parts Made Using Electron Beam Melting.* s.l., s.n., pp. 526-535.

RedEye Australia, 2014. *Industry: Aerospace case studies.* [Online]
Available at: http://redeyeaustralasia.com/files/Wyle.pdf
[Accessed June 2014].

RedEye, 2013. *Knowledge center: Case studies: ICON A5 aircraft.* [Online]
Available at: https://www.redeyeondemand.com/CS_Icon.aspx
[Accessed January 2014].

RedEye, 2014. *Industry: Rapid Manufacturing Aerospace Components.* [Online]
Available at: http://www.redeyeondemand.com/Industry_Aerospace.aspx
[Accessed July 2014].

Robin, A., Sandim, H. & Rosa, J., 1999. Corrosion Behavior of the Ti-6Al-4V Alloy in Boiling Nitric Acid Solutions. *Corrosion Science*, Issue 41, pp. 1333-1346.

Safdar, A., 2010. *Licentiate Dissertation: Microstructure and Surface Roughness of EBM Produced Ti-6Al-4V.* Malmo: Malmo University, Division of Material Science.

Schmidt, Robert G. Launsby; Kiemele, Mark J., 1997. *Understanding Industrial Designed Experiments.* Colorado Springs: Air Academy Press.

Schutz, R. W., 2005a. Titanium. In: *Corrosion Tests and Standards.* s.l.:ASM International, pp. 597-612.

Schutz, R. W., 2005b. Corrosion of Titanium and Titanium Alloys. In: *ASM Handbook*. s.l.:ASM International, pp. 252-299.

Starly, B., Parthasarathy, J., Raman, S. & Christensen, A., 2009. Mechanical Evalutaion of Porous Titanium (Ti6Al4V) Sturctures with Electron Beam Melting. *Journal of the Mechanical Behavior of Biomedical Materials*, Issue 3, pp. 249-259.

Startasys, 2014. *PolyJet: Bio-compatible*. [Online]
Available at: http://www.stratasys.com/materials/polyjet/bio-compatible
[Accessed June 2014].

Thomas Jefferson National Accelerator Facility, O. o. S. E., 2011. *The Element Titanium*. [Online]
Available at: http://education.jlab.org/itselemental/ele022.html
[Accessed 2013].

Welk, B. A., 2010. *Microstructural and Preperty Relationship in Beta-Titanium Alloy Ti-5553*. s.l.:Ohio State University.

Yu, S. & Company, 3., 2003. Corrosion Resistance of Titanium Alloys. In: *ASM Handbook: Corrosion: Fundamentals, Testing and Protection*. s.l.:ASM International, pp. 703-711.

Zygo, 2011. *Optical Profiler Basics*. [Online]
Available at: http://www.zygo.com/?/met/profilers/opticalprofilersabout.htm
[Accessed June 2014].

APPENDIX A

PROFILOMETER IMAGES FOR PART TWO RESUTLS

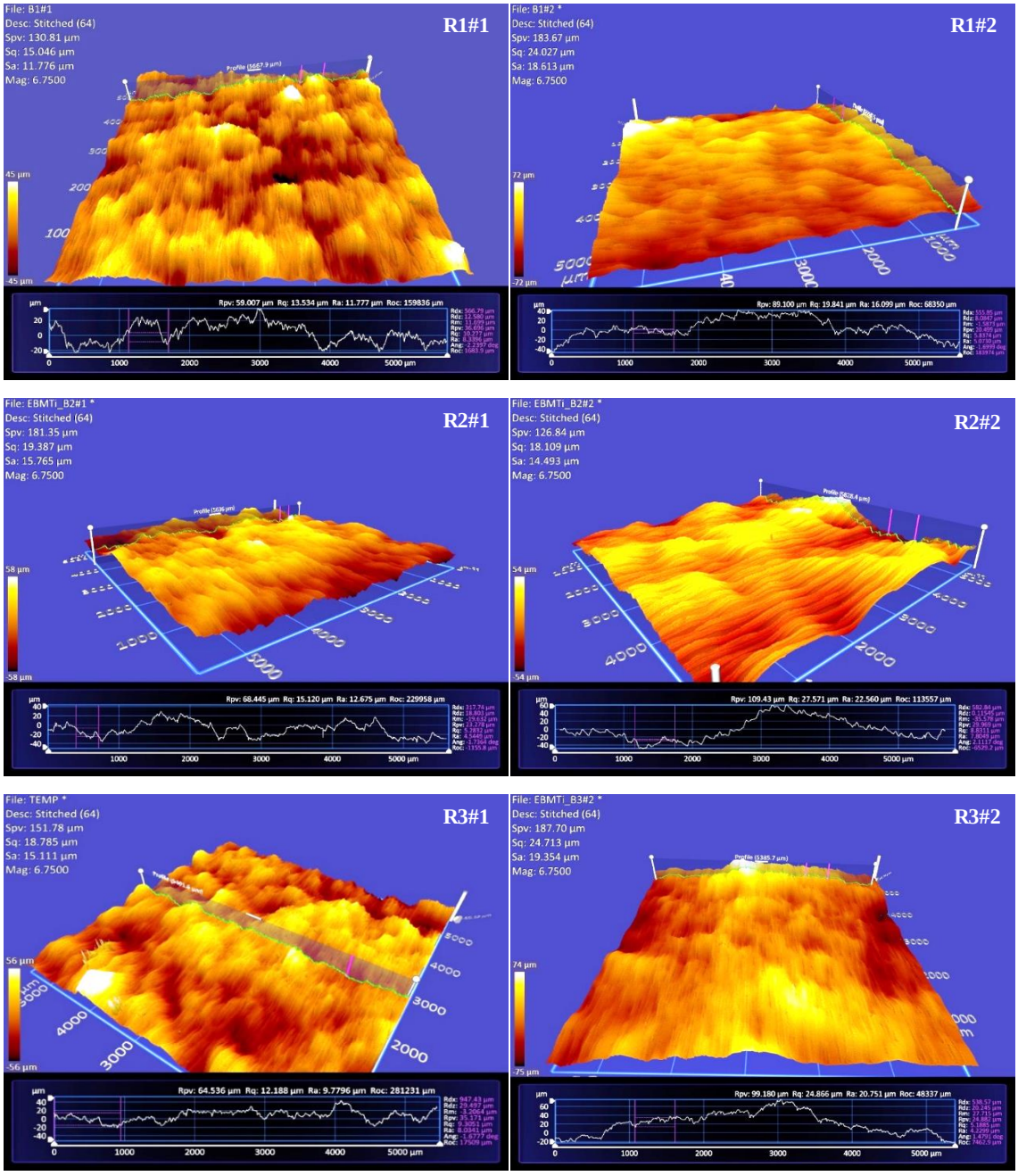

Figure A-1: 3D optical images for Ti-6Al-4V samples manufactured in EBM machine under different process parameters. Figures shown are for the three replicates of samples 1 and 2 as labeled. R1#2 indicates replicate 1 of sample #2.

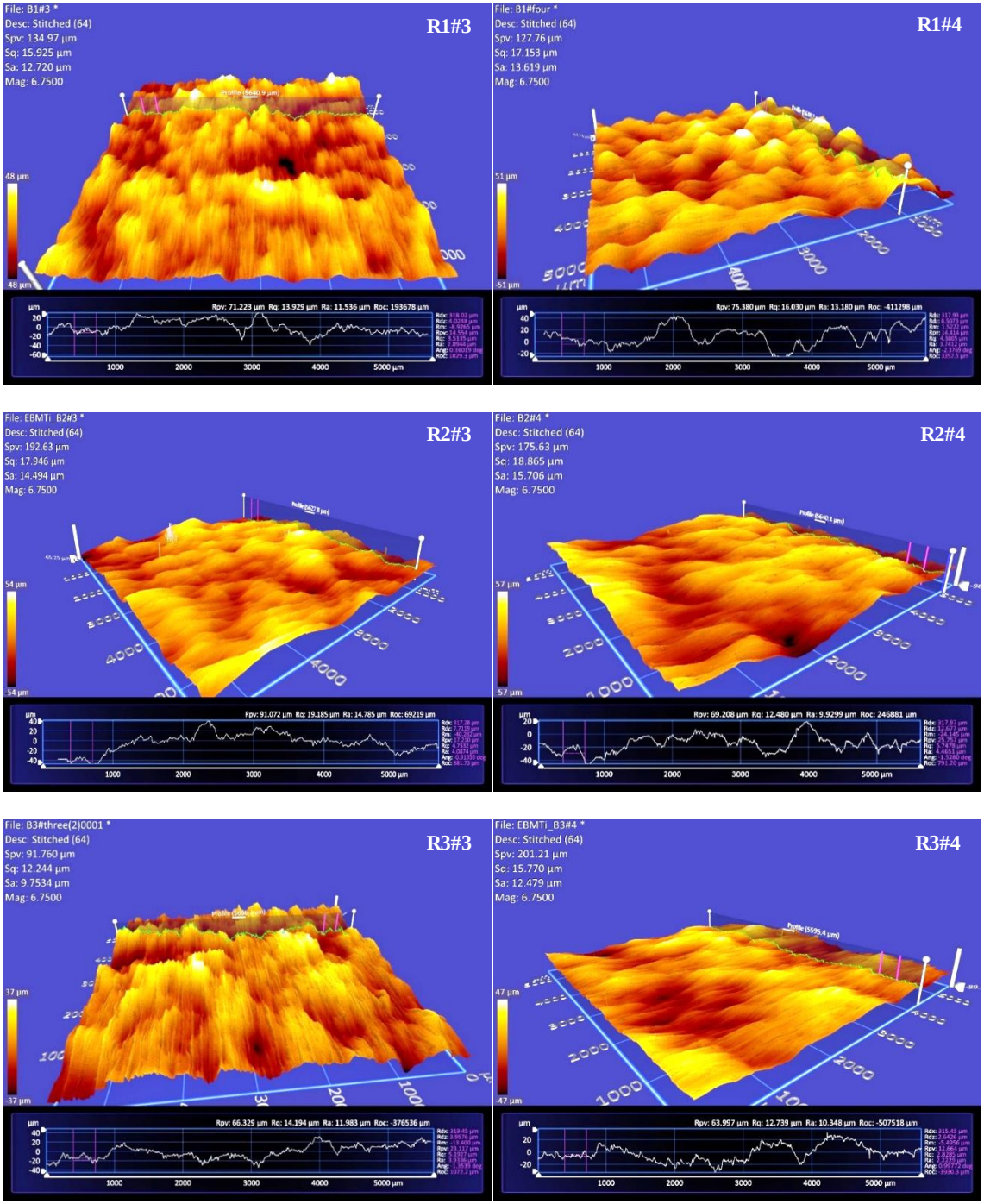

Figure A-2: 3D optical images for Ti-6Al-4V samples manufactured in EBM machine under different process parameters. Figures shown are for the three replicates of samples 3 and 4 as labeled. R1#3 indicates replicate 1 of sample #3.

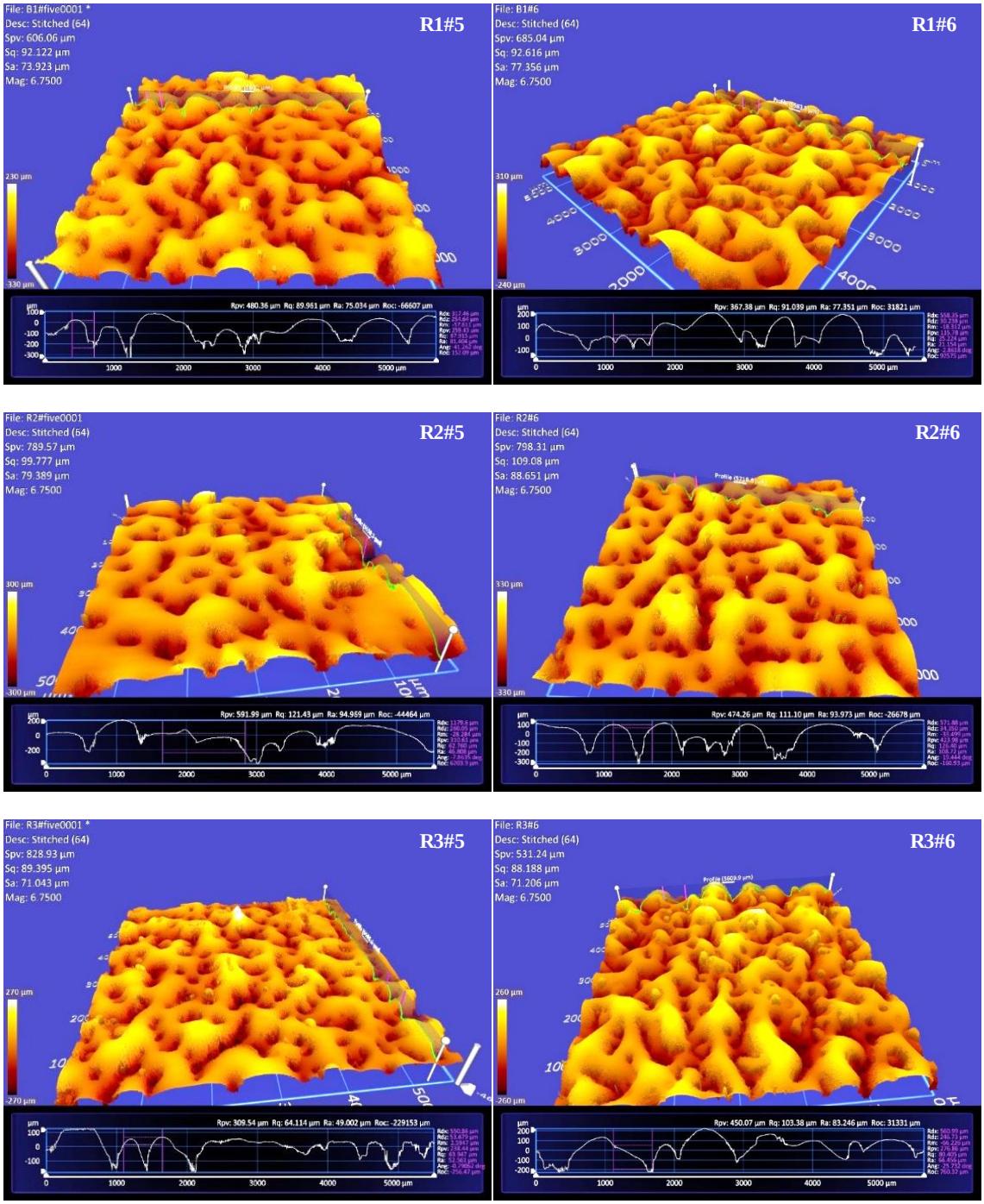

Figure A-3: 3D optical images for Ti-6Al-4V samples manufactured in EBM machine under different process parameters. Figures shown are for the three replicates of samples 5 and 6 as labeled. R1#6 indicates replicate 1 of sample #6.

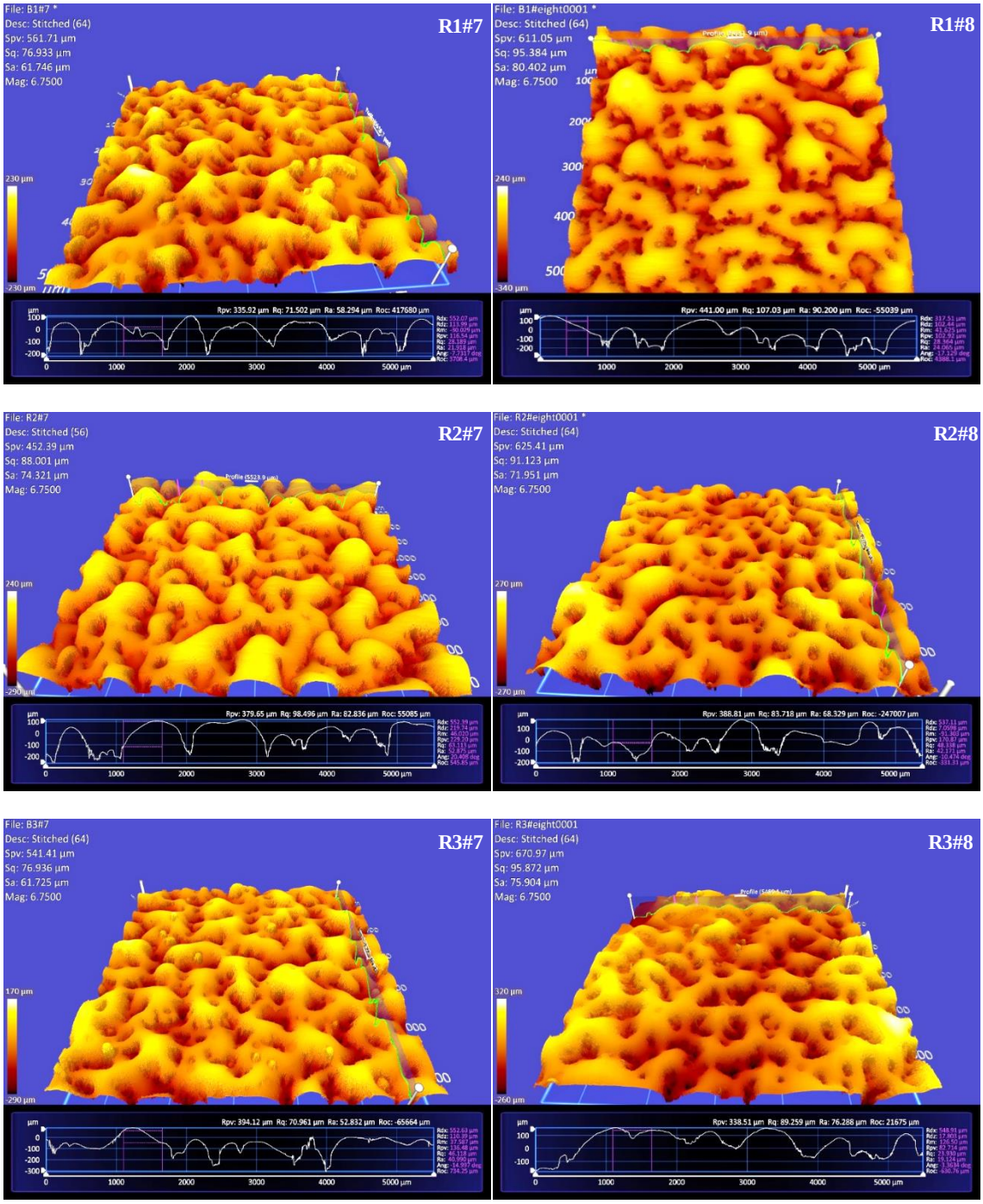

Figure A-4: 3D optical images for Ti-6Al-4V samples manufactured in EBM machine under different process parameters. Figures shown are for the three replicates of samples 7 and 8 as labeled. R1#8 indicates replicate 1 of sample #8.

APPENDIX B

EXAMINATIONS ON MEASURED PROPERTIES OF PART TWO

Surface Roughness		
Building parameter		Encoded Coefficient
Constant	-	18.2504
Current	A	1.14005
Speed	B	-0.00191925
Offset	C	2.92486
Current * speed	AB	0
Currnet * offset	AC	0
Speed* offset	BC	0
Current * speed * offset	ABC	0

Table B-1: Decoded coefficients relating surface roughness of EBM Ti-6Al-4V to EBM building parameters.

Building parameter			Property		Residual		
A	B	C	Surface roughness				
Current	Speed	Offset	Meas	Pred	Value	Percent	Abs(%)
5	3000	0	15.046	18.193	-3.1	-20.9%	20.9%
10	3000	0	24.027	23.893	0.1	0.6%	0.6%
5	6000	0	15.925	12.435	3.5	21.9%	21.9%
10	6000	0	17.153	18.135	-1.0	-5.7%	5.7%
5	3000	25	92.122	91.314	0.8	0.9%	0.9%
10	3000	25	92.616	97.015	-4.4	-4.7%	4.7%
5	6000	25	76.933	85.557	-8.6	-11.2%	11.2%
10	6000	25	95.384	91.257	4.1	4.3%	4.3%
5	3000	0	19.387	18.193	1.2	6.2%	6.2%
10	3000	0	18.109	23.893	-5.8	-31.9%	31.9%
5	6000	0	17.946	12.435	5.5	30.7%	30.7%
10	6000	0	18.865	18.135	0.7	3.9%	3.9%
5	3000	25	99.777	91.314	8.5	8.5%	8.5%
10	3000	25	109.080	97.015	12.1	11.1%	11.1%
5	6000	25	88.001	85.557	2.4	2.8%	2.8%
10	6000	25	91.123	91.257	-0.1	-0.1%	0.1%
5	3000	0	18.785	18.193	0.6	3.2%	3.2%
10	3000	0	24.713	23.893	0.8	3.3%	3.3%
5	6000	0	12.224	12.435	-0.2	-1.7%	1.7%
10	6000	0	15.77	18.135	-2.4	-15.0%	15.0%
5	3000	25	89.395	91.314	-1.9	-2.1%	2.1%
10	3000	25	88.188	97.015	-8.8	-10.0%	10.0%
5	6000	25	76.936	85.557	-8.6	-11.2%	11.2%
10	6000	25	95.872	91.257	4.6	4.8%	4.8%
					Residual	-0.5%	9.0%

Table B-2: Percent and absolute residuals for measured and predicted surface roughness of Ti-6Al-4V from EBM.

Critical Pitting Temperature (CPT)		
Building parameter		Encoded Coefficient
Constant	-	22.2717
Current	A	0.613333
Speed	B	0.00336278
Offset	C	0
Current * speed	AB	-0.000292778
Currnet * offset	AC	0
Speed* offset	BC	0
Current * speed * offset	ABC	0

Table B-3: Decoded coefficients relating critical pitting temperature of EBM Ti-6Al-4V to EBM building parameters.

Building parameter			Property		Residual		
A	B	C	CPT				
Current	Speed	Offset	Meas	Pred	Value	Percent	Abs(%)
5	3000	0	29.30	31.04	-1.7	-5.9%	5.9%
10	3000	0	30.85	29.71	1.1	3.7%	3.7%
5	6000	0	37.30	36.73	0.6	1.5%	1.5%
10	6000	0	31.80	31.02	0.8	2.5%	2.5%
5	3000	25	31.60	31.04	0.6	1.8%	1.8%
10	3000	25	30.30	29.71	0.6	1.9%	1.9%
5	6000	25	34.20	36.73	-2.5	-7.4%	7.4%
10	6000	25	31.60	31.02	0.6	1.9%	1.9%
5	3000	0	32.80	31.04	1.8	5.4%	5.4%
10	3000	0	30.71	29.71	1.0	3.3%	3.3%
5	6000	0	36.20	36.73	-0.5	-1.5%	1.5%
10	6000	0	29.80	31.02	-1.2	-4.1%	4.1%
5	3000	25	31.80	31.04	0.8	2.4%	2.4%
10	3000	25	29.70	29.71	0.0	0.0%	0.0%
5	6000	25	36.70	36.73	0.0	-0.1%	0.1%
10	6000	25	30.80	31.02	-0.2	-0.7%	0.7%
5	3000	0	27.21	31.04	-3.8	-14.1%	14.1%
10	3000	0	24.90	29.71	-4.8	-19.3%	19.3%
5	6000	0	39.79	36.73	3.1	7.7%	7.7%
10	6000	0	30.09	31.02	-0.9	-3.1%	3.1%
5	3000	25	32.90	31.04	1.9	5.7%	5.7%
10	3000	25	31.80	29.71	2.1	6.6%	6.6%
5	6000	25	36.20	36.73	-0.5	-1.5%	1.5%
10	6000	25	32.00	31.02	1.0	3.1%	3.1%
					Residual	-0.4%	4.4%

Table B-4: Percent and absolute residuals for measured and predicted CPT of Ti-6Al-4V from EBM.

Density		
Building parameter		Encoded Coefficient
Constant	-	4.41616
Current	A	0
Speed	B	0
Offset	C	-0.0166105
Current * speed	AB	0
Currnet * offset	AC	0
Speed* offset	BC	0
Current * speed * offset	ABC	0

Table B-5: Decoded coefficients relating density of EBM Ti-6Al-4V to EBM building parameters.

Building parameter			Property		Residual		
A	B	C	Density				
Current	Speed	Offset	Meas	Pred	Value	Percent	Abs(%)
5	3000	0	4.4376	4.4162	0.0215	0.5%	0.5%
10	3000	0	4.4073	4.4162	-0.0089	-0.2%	0.2%
5	6000	0	4.4122	4.4162	-0.0040	-0.1%	0.1%
10	6000	0	4.4011	4.4162	-0.0150	-0.3%	0.3%
5	3000	25	4.0175	4.0009	0.0166	0.4%	0.4%
10	3000	25	4.0021	4.0009	0.0012	0.0%	0.0%
5	6000	25	4.0236	4.0009	0.0227	0.6%	0.6%
10	6000	25	3.8805	4.0009	-0.1204	-3.1%	3.1%
5	3000	0	4.3998	4.4162	-0.0163	-0.4%	0.4%
10	3000	0	4.4146	4.4162	-0.0016	0.0%	0.0%
5	6000	0	4.4305	4.4162	0.0144	0.3%	0.3%
10	6000	0	4.4271	4.4162	0.0110	0.2%	0.2%
5	3000	25	4.0055	4.0009	0.0046	0.1%	0.1%
10	3000	25	4.0232	4.0009	0.0223	0.6%	0.6%
5	6000	25	3.9641	4.0009	-0.0368	-0.9%	0.9%
10	6000	25	4.0213	4.0009	0.0204	0.5%	0.5%
5	3000	0	4.3892	4.4162	-0.0270	-0.6%	0.6%
10	3000	0	4.4105	4.4162	-0.0056	-0.1%	0.1%
5	6000	0	4.4314	4.4162	0.0152	0.3%	0.3%
10	6000	0	4.4325	4.4162	0.0164	0.4%	0.4%
5	3000	25	4.0133	4.0009	0.0124	0.3%	0.3%
10	3000	25	4.0239	4.0009	0.0230	0.6%	0.6%
5	6000	25	4.0186	4.0009	0.0177	0.4%	0.4%
10	6000	25	4.0172	4.0009	0.0163	0.4%	0.4%
					Residual	0.0%	0.5%

Table B-6: Percent and absolute residuals for measured and predicted density of Ti-6Al-4V from EBM.

Porosity		
Building parameter		Encoded Coefficient
Constant	-	0.309976
Current	A	0
Speed	B	0
Offset	C	0.36688
Current * speed	AB	0
Currnet * offset	AC	0
Speed* offset	BC	0
Current * speed * offset	ABC	0

Table B-7: Decoded coefficients relating porosity of EBM Ti-6Al-4V to EBM building parameters.

Building parameter			Property		Residual		
A	B	C	Porosity				
Current	Speed	Offset	Meas	Pred	Value	Percent	Abs(%)
5	3000	0	0.3988	0.3100	0.089	22.3%	22.3%
10	3000	0	0.2875	0.3100	-0.022	-7.8%	7.8%
5	6000	0	0.1774	0.3100	-0.133	-74.7%	74.7%
10	6000	0	0.4266	0.3100	0.117	27.3%	27.3%
5	3000	25	9.1067	9.4820	-0.375	-4.1%	4.1%
10	3000	25	9.4555	9.4820	-0.026	-0.3%	0.3%
5	6000	25	8.9675	9.4820	-0.514	-5.7%	5.7%
10	6000	25	12.2066	9.4820	2.725	22.3%	22.3%
5	3000	0	0.4565	0.3100	0.147	32.1%	32.1%
10	3000	0	0.1223	0.3100	-0.188	-153.5%	153.5%
5	6000	0	0.2381	0.3100	-0.072	-30.2%	30.2%
10	6000	0	0.1611	0.3100	-0.149	-92.4%	92.4%
5	3000	25	9.3776	9.4820	-0.104	-1.1%	1.1%
10	3000	25	8.9784	9.4820	-0.504	-5.6%	5.6%
5	6000	25	10.3149	9.4820	0.833	8.1%	8.1%
10	6000	25	9.0204	9.4820	-0.462	-5.1%	5.1%
5	3000	0	0.6967	0.3100	0.387	55.5%	55.5%
10	3000	0	0.2140	0.3100	-0.096	-44.8%	44.8%
5	6000	0	0.2574	0.3100	-0.053	-20.4%	20.4%
10	6000	0	0.2831	0.3100	-0.027	-9.5%	9.5%
5	3000	25	9.2005	9.4820	-0.281	-3.1%	3.1%
10	3000	25	8.9608	9.4820	-0.521	-5.8%	5.8%
5	6000	25	9.0819	9.4820	-0.400	-4.4%	4.4%
10	6000	25	9.1130	9.4820	-0.369	-4.0%	4.0%
					Residual	-12.7%	26.7%

Table B-8: Percent and absolute residuals for measured and predicted porosity of Ti-6Al-4V from EBM.

APPENDIX C

POTENTIOSTATIC TESTS FOR MEASURING CPT OF PART TWO

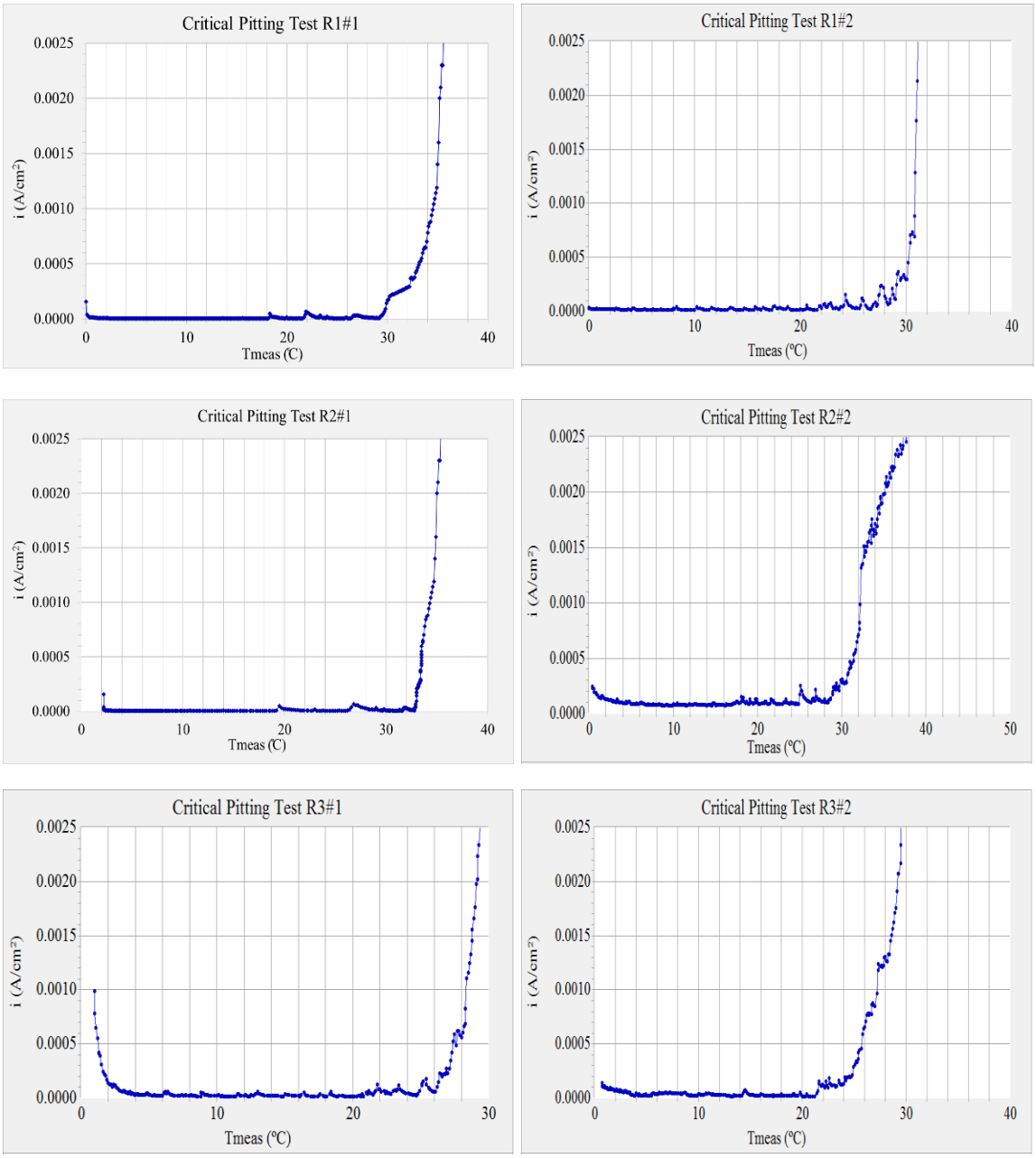

Figure C-1: Critical pitting temperature test for Ti-6Al-4V samples manufactured in EBM machine under different process parameters. Figures shown are for the three replicates of samples 1 and 2 as labeled. R1#2 indicates replicate 1 of sample #2.

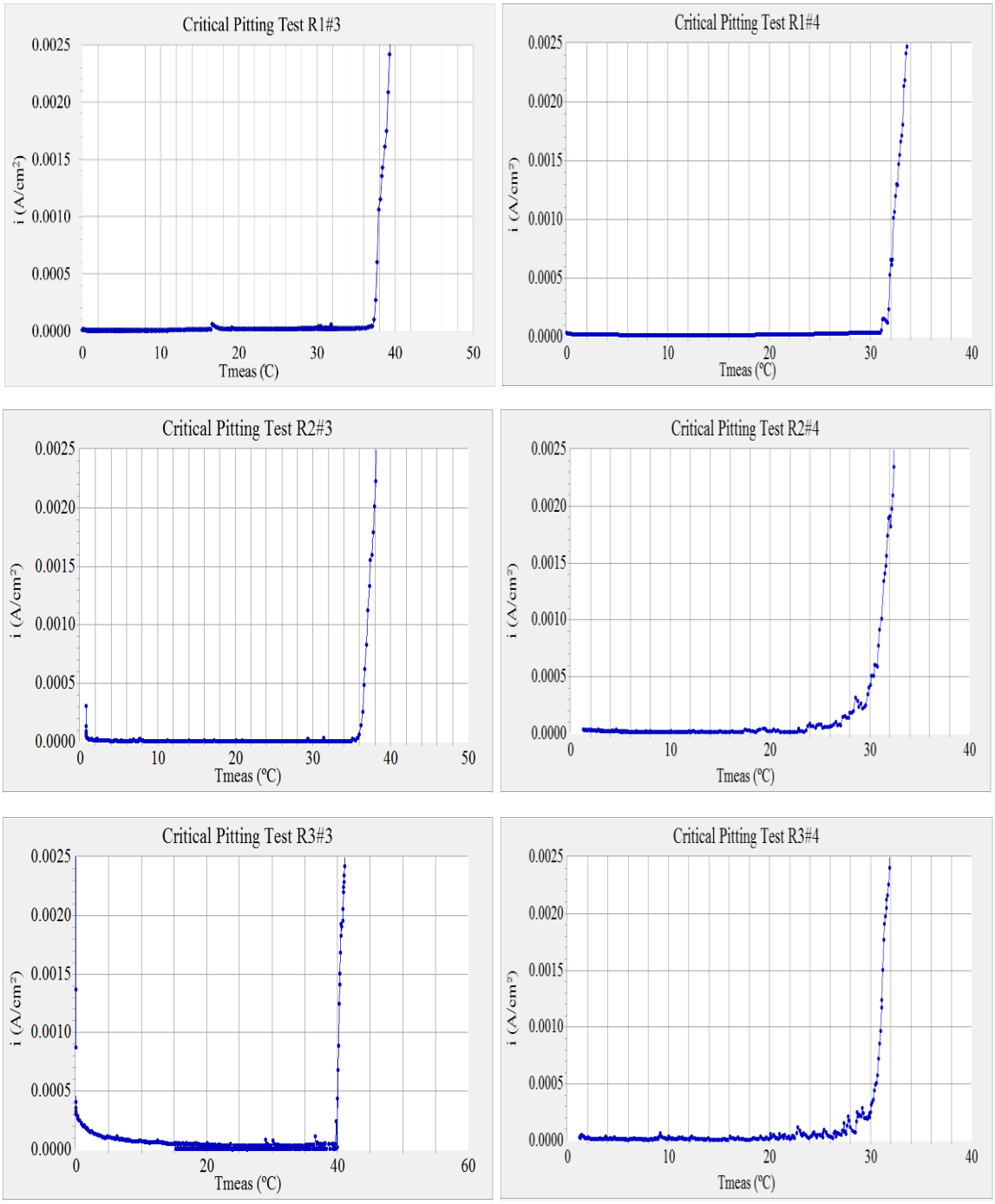

Figure C-2: Critical pitting temperature test for Ti-6Al-4V samples manufactured in EBM machine under different process parameters. Figures shown are for the three replicates of samples 3 and 4 as labeled. R1#4 indicates replicate 1 of sample #4.

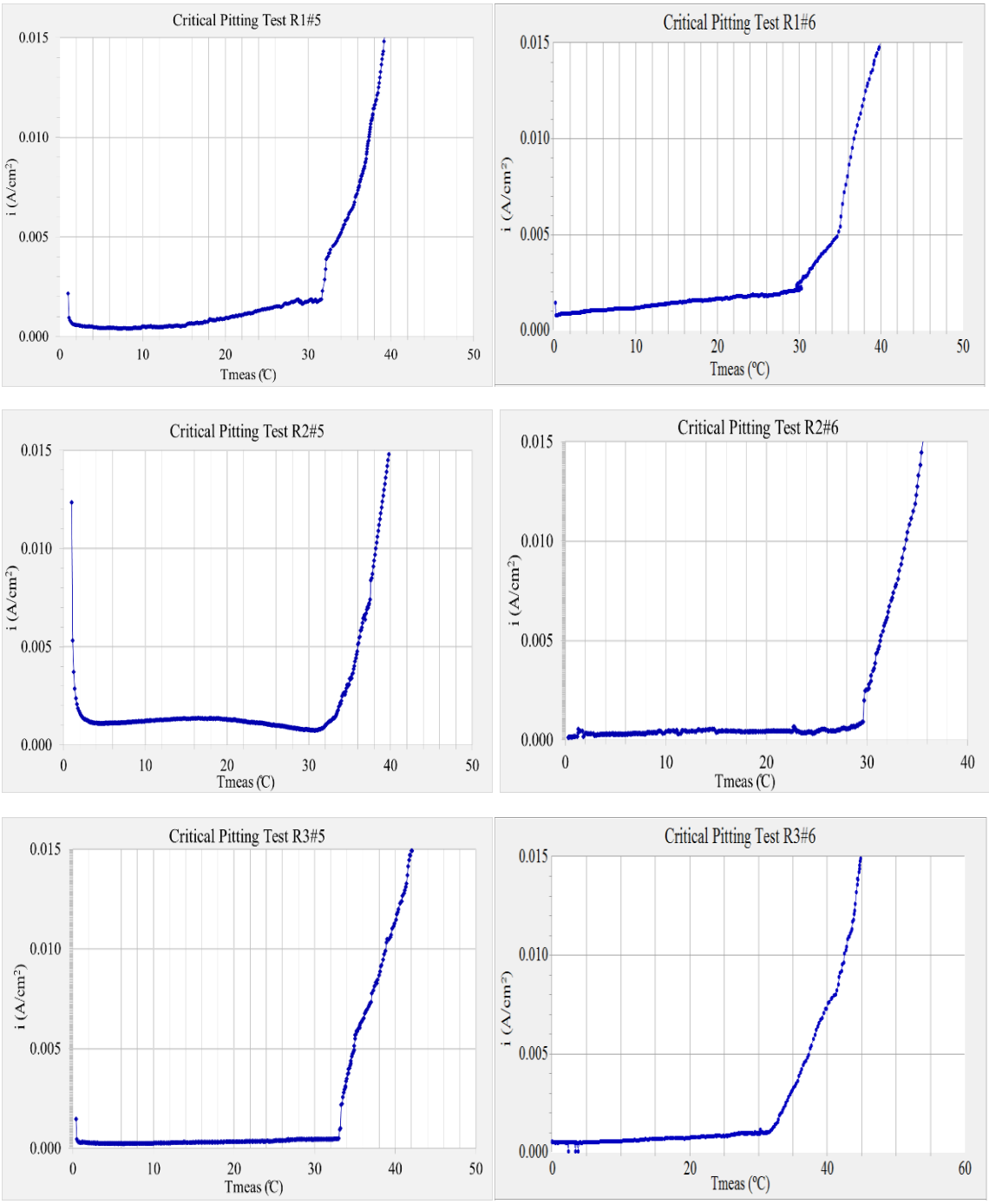

Figure C-3: Critical pitting temperature test for Ti-6Al-4V samples manufactured in EBM machine under different process parameters. Figures shown are for the three replicates of samples 5 and 6 as labeled. R1#6 indicates replicate 1 of sample #6.

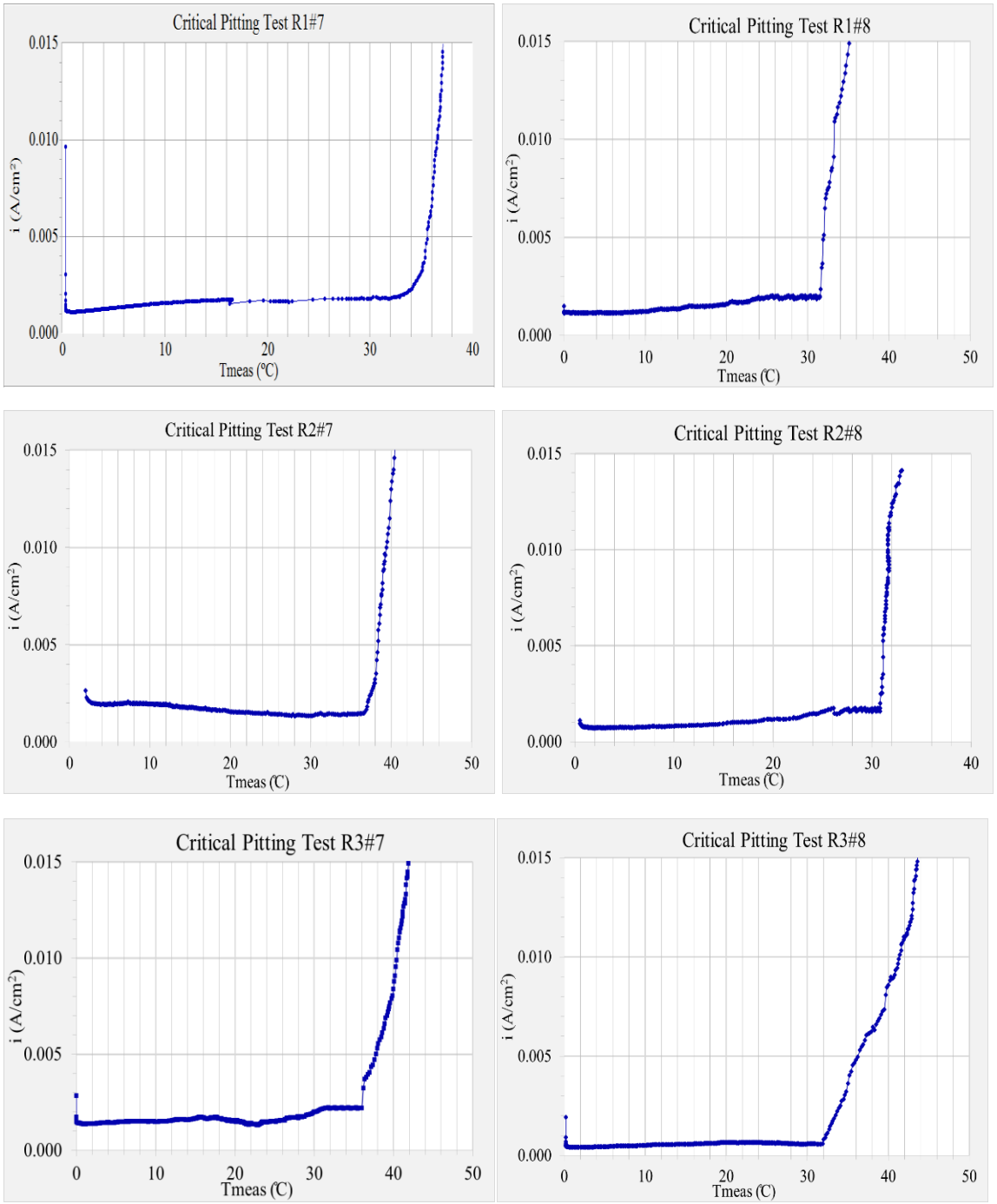

Figure C-4: Critical pitting temperature test for Ti-6Al-4V samples manufactured in EBM machine under different process parameters. Figures shown are for the three replicates of samples 7 and 8 as labeled. R1#8 indicates replicate 1 of sample #8.